SOLID-STATE-LASER-DRIVEN VAPORIZATION AND IONIZATION OF TIN

FOR EXTREME ULTRAVIOLET LIGHT SOURCES

Ph.D. thesis, Vrije Universiteit Amsterdam, 2025
Solid-state-laser-driven vaporization and ionization of tin
Dion Engels

Cover: An artistic interpretation of the UV shadowgraphy diagnostic.
A piece of tin is illuminated by a solid-state laser (red) and imaged by two UV wavelengths (the two purple colors), which show a different image due to their distinct wavelengths.
Back: The spectrum from Chapter 1, with gradually darkening purple behind it indicating different UV wavelengths.

DOI: 10.5463/thesis.1420
ISBN: 978-94-92323-82-8

Printing: Ridderprint
An electronic version of this dissertation is available at: research.vu.nl

VRIJE UNIVERSITEIT

Solid-state-laser-driven vaporization and ionization of tin

for extreme ultraviolet light sources

ACADEMISCH PROEFSCHRIFT

ter verkrijging van de graad van Doctor of Philosophy
aan de Vrije Universiteit Amsterdam,
op gezag van de rector magnificus
prof.dr. J.J.G. Geurts,
volgens besluit van de decaan
van de Faculteit der Bètawetenschappen
in het openbaar te verdedigen
op woensdag 26 november 2025 om 15.45 uur
in de universiteit

door

Dion Junior Engels

geboren te Venray

promotor:	prof.dr. O.O. Versolato
copromotoren:	dr. J. Sheil prof.dr. W.M.G. Ubachs
promotiecommissie:	prof.dr. K.S.E. Eikema prof.dr. R.A.H. Engeln prof.dr.ir. H.L. Offerhaus dr. A.S. Stodolna dr. H.J. Teunissen

The work described in this thesis was conducted at the Advanced Research Center for Nanolithography (ARCNL), a public-private partnership between the University of Amsterdam (UvA), the Vrije Universiteit Amsterdam (VU), Rijksuniversiteit Groningen (UG), the Dutch Research Council (NWO), and the semiconductor equipment manufacturer ASML. This thesis was also partially financed by the project 'Plasma driven by a variable-wavelength laser for next-generation EUV sources for nanolithography' (with project number 19458) of the Open Technology Programme, which is financed by NWO, and 'Toeslag voor Topconsortia voor Kennis en Innovatie (TKI)' from the Dutch Ministry of Economic Affairs and Climate Policy.

Contents

Introduction

The world's dependence on droplets of tin

In the most advanced EUV nanolithography machines, 50 000 tin droplets are blown up per second, continuously throughout each hour of every day. This adds up to 4.3 billion exploding tin droplets* per day, each droplet explosion emitting a small amount of light. This light is crucial, as it is extreme ultraviolet (EUV) light, which is used to 'print' modern computer chips in the rest of the machine. The computer chips produced in this way have become essential for many modern devices, such as computers, kitchen appliances, televisions, or cars, and thus also support modern services such as Netflix and ChatGPT. Due to these widespread applications, some of the most valuable companies in the world are in the business of computer chips.[1–3]

These extremely valuable and well-known companies, such as Microsoft and Apple, create end products utilizing computer chips. Other notable examples include tech companies like Google, Meta, or OpenAI. However, companies such as BMW, NXP, Bosch, and Texas instruments are also significant consumers of computer chips. All of these companies are at the bottom of the semiconductor industry pyramid, creating products with computer chips. The chip manufacturing process is delegated to a select group of companies called 'foundries' because of its complexity and cost. The largest foundry is TSMC,[4] which produces the chips of Apple and alone controls 60 % of the market†.[8]

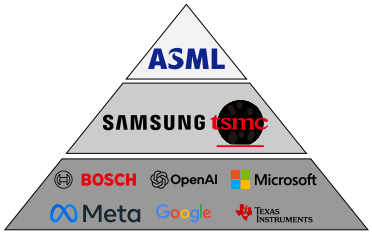

FIGURE 1: A pyramid of (a particular sector of) the chip industry. While many companies use and design chips, fewer can make them (the 'foundries'), and even fewer can make the machines (the 'tools') required. Thus, when focusing on one such tool, the nanolithography tool, ASML alone occupies the top spot of the pyramid.

Although there are only a few foundries with the ability to produce cutting-edge chips, even fewer

*For more than a 100 kg of tin per year.

†Making it key to Taiwan's autonomy,[5,6] and also using 8 % of all electricity produced in Taiwan, which is expected to rise above 20 % in 2030.[7]

can make the machines, 'tools,' needed to do the job. The key tool to make a chip is the nanolithography machine, which is one of the most expensive. In addition, it has the greatest impact on the efficiency and speed of the chip being produced. And only one company can supply the newest generation lithography tool, the one that utilizes tin droplets, and thus occupies the top spot of the pyramid: ASML*.

A short history of the most complex machines in the world

Modern lithography machines are extremely complex[9] room-sized machines costing more than 200 million euros.[10] Here, we focus on a single module of the lithography machine: the source. In the source, EUV light is generated and sent into the rest of the machine to be used to create computer chips.

The previous generation of lithography machines utilized light with a wavelength of λ=193 nm, with the light generated from a KrF laser. However, to achieve the nanometer-sized features required for modern chips, even shorter wavelengths are necessary. This is because of the fundamental limit of optics described by the Abbe limit:

$$\mathrm{CD} = k_1 \frac{\lambda}{\mathrm{NA}}. \tag{1}$$

The critical dimension (CD) is determined by two main factors: λ, the wavelength of the light and the numerical aperture (NA) of the system, which is defined as $\mathrm{NA} \approx D/2f$ for optical systems in air or vacuum (where D is the size and f the focal length of the lens). The numerical aperture can be imagined as a sphere surrounding the focal point; the more of this sphere the lens occupies, the higher the NA. Furthermore, the factor k_1, which varies based on process optimizations, typically ranges from 0.25–0.4. Thus, transitioning to a shorter wavelength becomes necessary to achieve a smaller critical dimension, given the limitations on increasing the NA. This reduction in the critical dimension allows for an increased number of transistors on a chip, resulting in enhanced chip performance and efficiency.

Research on extreme ultraviolet (EUV) lithography, the newest generation of lithography machines, started more than 30 years ago in the late 1980s.[11–14] One of the first challenges was to decide which exact wavelength shorter than 193 nm to use. A wavelength of 13.5 nm was chosen primarily because of the availability of mirrors at this specific extremely short wavelength. Lenses are not suitable because EUV wavelengths are absorbed by almost all materials†. Thus, multilayer mirrors consisting of

*For this specific part of the industry. There are many other companies that are key for other components, such as extremely pure silicon wafers, metrology tools, or other steps in the manufacturing process such as etching.

†Including air; there is a vacuum inside the machines.

tens of layers alternating between molybdenum and silicon are required to transport the 13.5 nm EUV light.[15]
The fundamental principle involves a small amount of light being reflected by each even molybdenum layer (the reflector) and transmitted through the odd layers of silicon (the spacer). Then, by matching the spacing between the reflecting layers with the wavelength of the light*, constructive interference occurs, resulting in reflection. This phenomenon is known as the Bragg effect and is illustrated in Fig. 2.

Multilayer mirrors composed of molybdenum and silicon can reflect over 70 % of the light within a 1 % range around 13.5 nm (i.e., 13.3–13.7 nm),[16] offering some of the best reflectivity performance. Other material combinations can lead to peak reflectivity at different wavelengths, but no other material combination comes close to the 71.2 % peak reflectivity reported for molybdenum and silicon.[17] Given that approximately ∼10 mirrors are required in the lithography machine, even a minor increase in transmission is crucial. For example, improving the reflectivity from 65 % to 70 % more than doubles the light output after the 10th mirror. Thus, that is the justification for 13.5 nm: it is the wavelength of the best multilayer mirrors, those consisting of molybdenum and silicon.

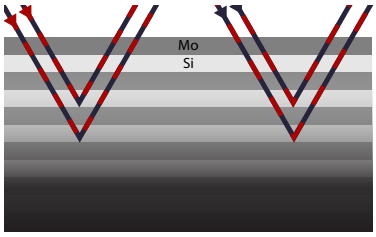

FIGURE 2: A schematic of the Bragg effect. A ray of light with a wavelength (illustrated by the dashed line) comes in and reflects on the molybdenum layer. For the left case, the wavelength is correct, and the light waves are in phase after the reflection. The wavelength on the right does not match the thickness of the materials, is out-of-phase and will not be reflected as well.

The next challenge lies in creating an EUV source that can produce a large amount of light (100–180 W was a typical desire during the early development[15,18]) that falls within 1 % of 13.5 nm, referred to as 'in-band' EUV. The use of a conventional laser, as previously used for 193 nm, is not feasible due to the absence of suitable technology. The only available 'laser' technology capable of producing 13.5 nm light is the free-electron laser (FEL). FELs function by emitting light through the acceleration and deceleration of electrons and are capable of emitting at 13.5 nm. However, there are significant technology challenges that make it difficult to use FELs for EUV production, such as the fact that one FEL would power several lithography machines, increasing the risk of downtime, and the fact that the light is coherent.[19,20] Similarly, a synchrotron light source,[21] or other more compact X-ray sources,[22] are also considered difficult to implement technologically. An alternative approach involves high-harmonic generation (HHG). This process

*Resulting in layers of a few nm thick.[15]

involves the removal of electrons from their atoms by an intense ultra-short laser passing through a gas cell, with the electrons returning as the electric field of the light reverses. This results in the creation of odd 'higher harmonics,' such as 1/3x, 1/5x, etc., of the original laser wavelength, potentially yielding 13.5 nm. However, the conversion efficiencies (CE) of laser light into in-band EUV light are typically <0.01 %, and given that industrial lasers are typically limited to 100 kW, it is not possible to exceed a few watt of EUV using HHG.[23]

The solution is to generate a plasma. In natural settings, plasma occurs under conditions of high temperature, such as those found in the Sun, or as a result of high applied voltages, as observed in welding and lightning.[24] In a plasma, electrons detach from their host atoms, which become ions with electron deficiencies. Plasmas typically emit light when an electron transitions between energy states or when electrons and ions recombine. In laboratory settings, typical ways to create a plasma are by illuminating a target with a pulsed laser, resulting in a laser-produced plasma (LPP), or by creating a discharge, a discharge-produced plasma (DPP). Since industrially available pulsed lasers can achieve power levels exceeding 20 kW,[25] a conversion efficiency of only 0.5 % would already give 100 W of in-band EUV*. Additionally, liquid microdroplet-based laser-produced plasma generate less debris than discharge-produced plasmas, giving them an advantage in long-term operation.[15,18,26] Thus, a laser-produced plasma is the ideal choice for an EUV source. But that leaves the question: Which element should be used as the ion in the plasma to maximize EUV emission?

Tin is the perfect choice for this case, as Sn^{10+} to Sn^{14+} are strong emitters around 13.5 nm.[15,18,27] The excitation-deexcitation of multiply excited electrons in these ions has been shown to be the origin of this emission.[28] This characteristic makes tin ideal for producing 13.5 nm light, provided that the plasma can be heated sufficiently to ensure that Sn^{10+} to Sn^{14+} ions are dominant. Schupp *et al.* demonstrated that tin can emit nearly 20 % of its total light output in the 13.5 nm in-band region, which is an exceptionally high value.[29] Consequently, conversion efficiencies of laser light into EUV of 5 % can be achieved, providing a pathway to >100 W EUV sources.[30]

A modern EUV source

In more than two decades of development, ASML has successfully engineered the commercial extreme ultraviolet (EUV) source, which is currently capable of producing an output over 500 W to be used for printing in the rest of the machine.[32,33] A modern EUV source has several essential components that deserve to be introduced, which

*Typical lasers in this Thesis have pulse lengths of ~10 ns, and an intensity of at least 10^7 W/cm^2, more than a million times the intensity of a stove top.

are schematically shown in Fig. 3.
First, the 'collector mirror,' which gathers the EUV light emitted from the plasma and sends it into the machine through the 'intermediate focus' (IF). The collector mirror occupies nearly half of the sphere surrounding the tin plasmas, specifically the side of the plasma that is heated by the laser, as the majority of EUV is emitted in that direction. Therefore, only EUV emitted towards the laser-facing 2π (i.e., half of the sphere) is considered for plasma-driven EUV sources. This consideration was already included in the 5 % conversion efficiency mentioned previously.
Second, the collector mirror is perpetually at risk of being hit by charged tin ions leaving the tin plasma. The 'buffer gas' serves to prevent tin from hitting the collector

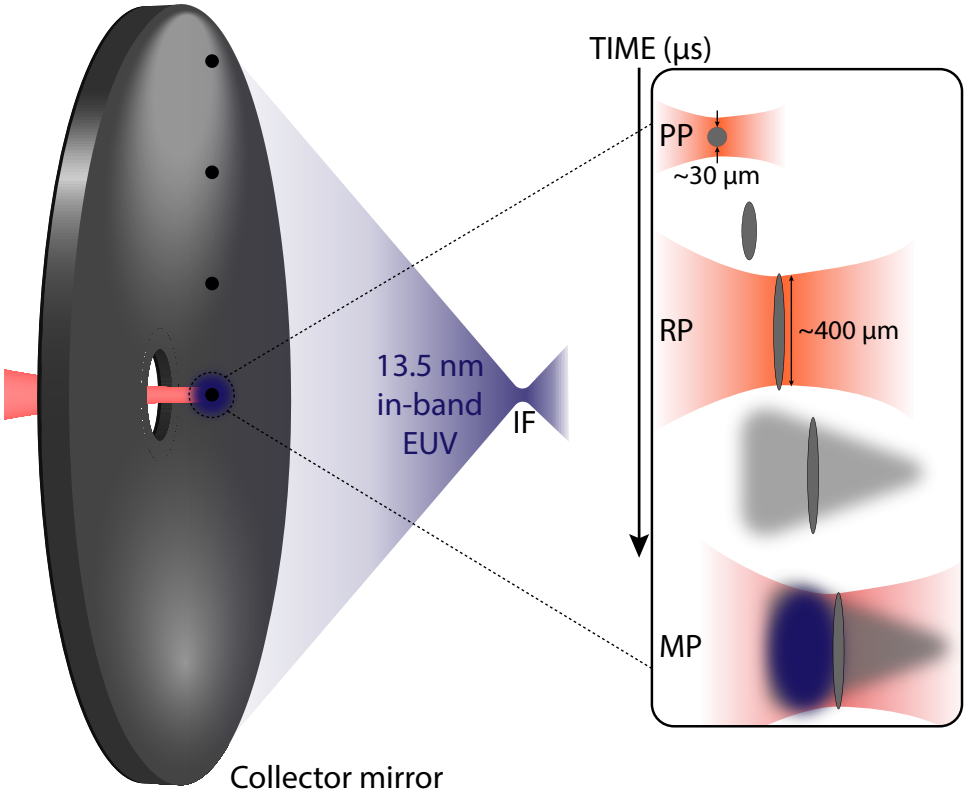

FIGURE 3: A schematic of a modern EUV source with its multiple laser pulses. Each tin droplet, moving downward in a stream, is deformed and expanded radially by the pre-pulse (PP), vaporized by the rarefication pulse (RP), and then blown up using the main pulse (MP) to generate EUV light in a process taking a few µs. The collector mirror is on the left and collects the 13.5 nm in-band EUV light into the machine via the intermediate focus (IF). Displacement of the illustrated tin is purely for visual clarity. Inspired by Ref. [31].

mirror, as this would lead to rapid degradation of the mirror performance. Third, the 'droplet generator' produces a stream of tin microdroplets, each with a diameter of tens of µm*.[26,34,35] 50 000 droplets per second are shot into the machine, each transformed into a plasma by a high-power laser to generate a burst of EUV light.[35]

Finally, a modern EUV source has three laser systems. The first laser to interact with the droplet is the 'pre-pulse' (PP), starting the 'target shaping' process, where a 'target' is made out of the droplet.[36,37] The pre-pulse generates a small plasma on the tin, inducing hydrodynamic expansion and deformation into a 'sheet,' a process that takes a few microseconds. The sheet typically exceeds 200 µm in diameter and ranges between 0.05–2 µm in thickness.[38] The modified aspect ratio of the tin sheet matches the optimal length scale of a CO_2-driven plasma, at a size of several 100 µm, better than that of the initial droplet.[35] However, a drawback of the pre-pulse is that it consumes approximately 10 % of the tin and more tin is lost over time through small fragments as the sheet expands.[39]
Subsequently, the thin sheet is transformed into a vapor by the 'rarefication pulse,' which arrives a few microseconds after the pre-pulse.[33] This transformation from sheet to vapor decreases the density of the target while increasing the length scale along the laser propagation axis.[35,40] Both of these effects improve the absorption of the final laser pulse when compared to the tin sheet, which acts as an effective mirror while the vapor offers long path lengths for absorption. Finally, the 'main pulse' creates the EUV-emitting plasma. In modern systems, this is a pulsed CO_2 laser with a wavelength of 10.6 µm operating at 50 kHz.[26,41] The advantages of CO_2 are its maturity as a system capable of outputting the desired >20 kW of laser power,[33,35] and its long 10.6 µm wavelength supporting high CE values.[42]

Research questions and thesis outline

The development of EUV sources has not stopped now that 500 W output has been achieved. There are still many open questions, both physics-related and more applied to the current machine, that could allow for optimization of each step in the process and thus increase EUV output. For example, the pre-pulse, which has been in use for years now, is still an active field of research, where in-depth fluid dynamic questions such as "What sets the curvature of the tin sheet?"[43] and "What kind of instabilities play an important role in the pre-pulse process?" are being studied. Similarly, the rarefication pulse opens up many different ways of preparing the target that will be hit by the main pulse. "What kind of composition should the vaporized tin have? Should liquid microdroplets be present in the vapor or not? Should the vapor be

*Less than half of the width of a human hair.

relatively cold or hotter, and maybe even ionized? What shape should the vapor have to optimize the absorption of the main pulse? What parameters should the used solid-state laser have to achieve these parameters?" The parameter space is practically endless.

Steps to optimize the pre-pulse or rarefication pulse could be integrated into a modern EUV source with relative ease. However, one can also wonder about larger changes. Why should this combination of three laser pulses be the limit? Could an additional pulse give even better performance? What if one of the lasers is switched out for an alternative? The biggest contender in this field is to use a main pulse generated by a solid-state laser, with a wavelength of 2 µm, to replace the current 10.6 µm CO_2 main pulse. Solid-state lasers are already being used for the pre-pulse and rarefication pulse,[33,41] as solid-state lasers offer high efficiency of electrical power to laser power in a compact package. However, so far, solid-state lasers have not been able to challenge the 10.6 µm CO_2 laser in the role as main pulse, due to a mismatch of technological limits for solid-state lasers and optimal plasma conditions for EUV generation. This is changing for 2-µm-driven sources, which offer several benefits, such as good EUV generation performance and potential scaling pathways to higher EUV powers, combined with the higher laser efficiencies typical of solid-state lasers. It is an active field of research to quantify their feasibility for industrial applications, both related to the plasma physics of such a source, but also to create the laser technology required.

Of course, all this is too much for a single PhD thesis. For this Thesis, we focus on novel applications of solid-state laser-driven processes related to EUV sources, taking inspiration from the rarefication pulse and solid-state laser-generated main pulses. What happens when a laser pulse, from a solid-state laser, interacts with tin?

Depending on the intensity of the laser pulse, we can split the study of the interaction of laser pulses generated by solid-state lasers with tin into two areas. The first area is the vaporization of liquid tin using a low-intensity ($1–1000 \times 10^6$ W/cm^2) 1 µm solid-state laser, inspired by the rarefication pulse relevant for the target shaping process in industrial nanolithography machines. Here, we aspire to answer questions such as "What is the composition of the vapor created by a solid-state laser vaporizing a tin sheet?", "What physical process governs the vaporization?", and "Which parameters impact the resulting vapor?" The second area of study is EUV-producing plasmas driven by a high-intensity ($>1 \times 10^{10}$ W/cm^2) 2 µm laser, an alternative to the current industry standard 10.6 µm CO_2 main pulse. In this field, important open questions are "What is the behavior of the ion emission for 2 µm compared to the widely studied 1 µm or 10.6 µm?", "What is emitted by a 2-µm-driven EUV-emitting plasma in addition to the EUV photons?", "How can 2-µm-driven EUV sources reach industrial

levels of EUV emission?", and "What is the best 'target,' such as a sheet or vapor, for 2-µm-driven EUV sources?" Along those lines, we define two overarching research questions:

What sets the composition of a tin vapor created by a laser pulse from a tens of nm-thick liquid tin sheet and which parameters impact this composition?
What physics would allow the scaling of 2-µm-driven EUV-emitting plasma sources from laboratory to industrial application?

These research questions leave a broad range of topics to investigate and each chapter of this Thesis will focus on a specific part. Chapters 1–3 will be related to vaporization using a solid-state laser, while Chapter 4 will focus on 2-µm-driven EUV sources.

Chapter 1 introduces a novel diagnostic to investigate the composition of tin vapors. Specifically, we vaporize thin sheets with a 6 ns 10^8 W/cm^2 laser pulse and then study the resulting vapor cloud 100 ns later. We study the vapor by making images of it in transmission and measuring the extinction (absorption + scattering) of light as it passes through the vapor. We can make a spectrum of the extinction of light in the vapor by using hundreds of backlighting wavelengths, which range between 235–400 nm in the UV. We use this extinction spectrum, which we can make per pixel in our image and thus spatially resolved with a resolution of 10 µm, to reveal that the vapor consists of small nanoparticles (radius <30 nm) and free atoms with a temperature around 3000 K. Moreover, we find that the vapor is spatially homogeneous; the composition is the same for every position in the vapor.

Chapter 2 sets out to understand how the vaporization process actually works. To do so, we use a much longer 100 ns vaporization pulse, allowing us to take pictures during the vaporization. We observe the sheet gradually thinning from these pictures taken during the vaporization pulse. This points to Hertz-Knudsen vaporization being the vaporization mechanism, compared to some alternative mechanisms common in fast vaporization. We develop a model based on Hertz-Knudsen vaporization, reproducing our experimental data well. By combining two methods to observe the sheet shrinking, we can conclude that sheets with a thickness ranging 30–300 nm all vaporize via Hertz-Knudsen for laser intensities between 0.2–4 $\times$ 10^7 W/cm^2. Thus, we understand the mechanism of vaporization for tin sheets: the same mechanism as a puddle of water outside, just a billion times faster.

Chapter 3 takes vaporization to the extreme by increasing the laser intensity a hundredfold in an effort to change the composition of the vapor. Specifically, we study how the resulting vapor depends on the laser intensity ranging 1–130 $\times$ 10^7 W/cm^2, encompassing the intensity of both Chapters 1 & 2, but also extending it significantly higher. We do this to study the dependence of the vapor on inputs such as the original

sheet target or the laser parameters. Which 'knob' should have to be turned to change the vapor significantly? We find that the laser intensity is a key parameter as long as it is increased to above the threshold to form plasma during the vaporization. Once this laser intensity is achieved, the vapor changes from a uniform 3000 K mix of nanoparticles and atoms to a hot 8000 K free atom-only vapor. The density of the atoms increases as the nanoparticles disappear, making laser intensity a key pathway to creating dense atom-only vapors.

Finally, **Chapter 4**, takes the intensity to EUV-emitting regimes. By increasing the laser intensity, the temperature of the plasma will increase, and thus will the average charge state $\bar{z}$ of the ions in the plasma.[44] As the laser intensity reaches the $\sim 10^{11}$ W/cm^2, the plasma temperature will increase to the ∼30 eV required to have a large presence of the 13.5 nm in-band EUV emitting ions of Sn^{10+} to Sn^{14+}. We supply this required laser intensity using a 2 µm laser, an alternative to the current industry standard 10.6 µm. Previously (see List of Publications), we already showed that 2-µm-driven plasmas can obtain promising conversion efficiency (CE) values. That is why this work, the culmination of a decade of work on EUV-emitting plasmas at ARCNL, tries to complete the case for 2 µm technology being a promising candidate for future EUV sources. It does so by focusing on quantifying the power partitioning, studying the balance of input energy (the laser) and energy sinks, such as emitted light, ions, neutrals, and laser reflection or transmission. We show that we can reconstruct the complete power partitioning, reconstructing 101(14) % of the input energy. Around 70 % of the energy goes into the emission of photons, of which a dominant fraction is emitted in the 5–70 nm wavelength range. Plasma ions contribute ∼30 % of the energy, and this fraction slightly decreases as a function of the laser intensity, whereas photon emissions increase in step. These results offer a benchmark of the plasma power partitioning for future research into and industrial applications of EUV lithography sources.

These results are summarized and reflected upon in **Conclusion & Outlook**. In the outlook, we expand on the results shown in the main chapters for both applications of solid-state lasers: the vaporization of tin and 2-µm-driven EUV sources. For tin vapor, we show the potential of a dye-laser-backlight UV shadowgraphy setup, replacing the broadband OPO laser used in this Thesis. The narrow-band dye laser allows for density and linewidth extraction from the extinction spectra, and detailed probing of the tin atomic resonances. For 2-µm-driven EUV sources, we look toward a concept without a pre-pulse, where the 2 µm main pulse hits the droplet directly. This concept has been studied using radiation-hydrodynamic simulations[45] and offers a potentially novel pathway to high EUV source powers. The first step in the experimental study of this concept is demonstrated and paves the way for future work to further validate the concept.

Experimental setup

ARCNL is the proud owner of two small-scale EUV sources, the Daleks*. The vacuum chambers are identical and therefore are called *Dalek-I* and *Dalek-II*. The main task of the Dalek setups is to create a vacuum environment ($\sim 10^{-6}$ mbar) for the tin droplet stream that is easily accessible by lasers and many (optical) diagnostics. That is why the Dalek chamber features 52 vacuum ports located only 18 cm away from the center of the chamber, creating many options to access the center of the chamber with a high NA. Figure 4 shows cross-sectional drawings of the entire Dalek setup (vacuum chamber and selected components around it) from the side view, the front view, and the top view.

Both Dalek setups are identical at their core, even though both have gone through many iterations over the years. The difference between the Dalek setups is their application and thus exact laser systems and diagnostics. Dalek-I is the setup currently focused on 2 µm EUV sources and is thus used for Chapter 4 and some other publications related to 2 µm (see List of Publications). Dalek-II is the setup for vaporization experiments and is used for Chapters 1–3.

In this section, we focus on the main principles of the experimental setup, usually skipped over in individual publications, such as the droplet generation and triggering systems, while each chapter will describe the key setup components for that exact study. The report of this section will be based on the status of the Dalek systems in the spring of 2025, to include all the improvements done over the years. For older and in some aspects more detailed descriptions of Dalek systems, one can read the theses of Kurilovich[46] and Meijer.[31]

A stream of tin

The droplet generator sits on top of the Dalek vacuum chamber. The entire droplet generator system is called the 'source'†. The source consists of two main components: a tin tank and a nozzle assembly (indicated as (1) in Fig. 4), and is connected to the Dalek via a flange, which also allows for feedthroughs to send electrical signals to the nozzle and to measure temperatures. This flange sits on motorized movable bellows, which allow the source to tilt with respect to the Dalek, ensuring that the droplet stream passes through the center of the chamber. The tin tank holds the liquid tin (roughly 1.3 kg) and has its own heating element. In preparation for the experiment, the tank is filled with solid 99.999 % pure tin blocks and pumped to vacuum ($\sim 10^{-6}$ mbar) through a line at the top to stop further oxidization of the tin.

*Named for the fictional race of robots seen in Doctor Who.

†Not to be confused with the EUV source, this is the droplet source. The source of the source.

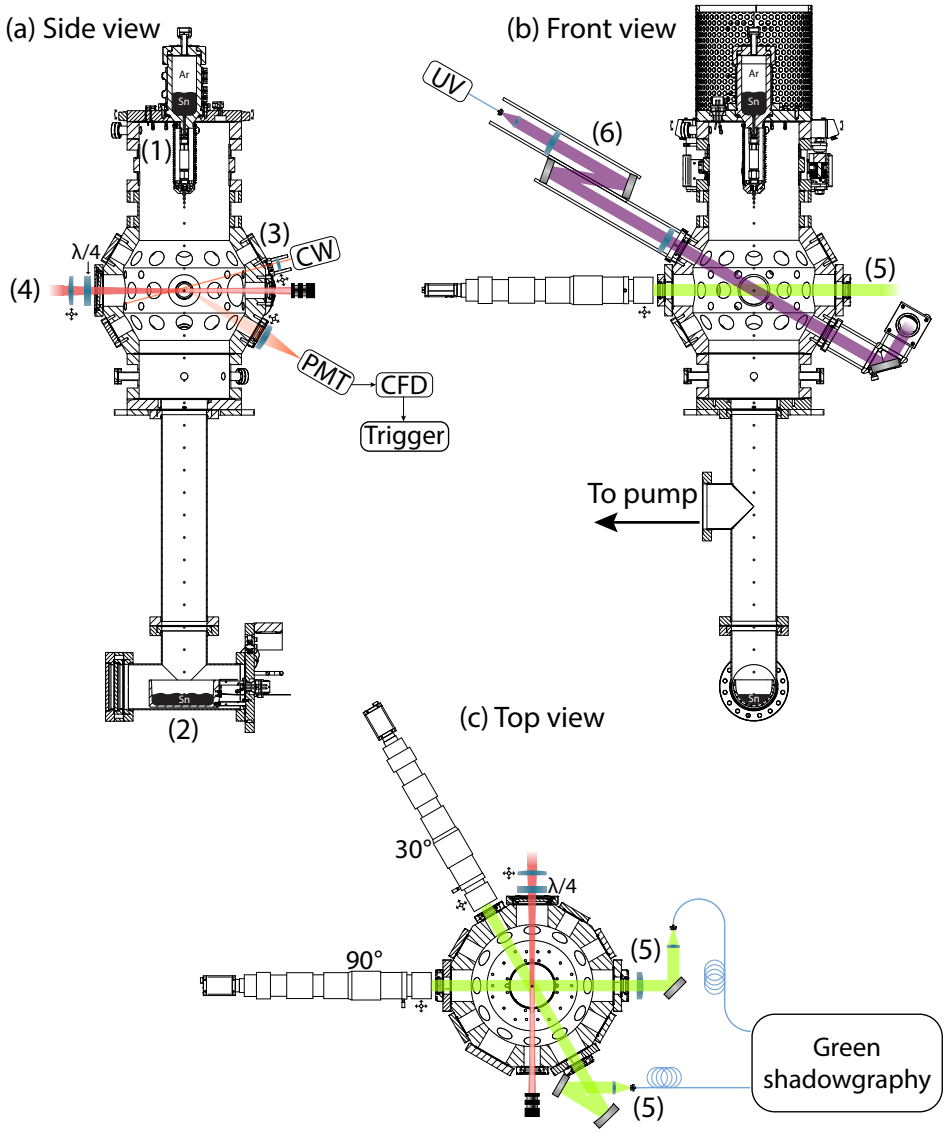

FIGURE 4: Illustration of a Dalek setup from three views. Numbered icons indicate (1) the nozzle, (2) the catcher, (3) triggering system, (4) the pre-pulse, (5) green shadowgraphy, and (6) UV shadowgraphy. Inspired by Ref. [31].

The tin in the tank is brought to 270 °C, well above the melting point of the tin at 232 °C. The nozzle is brought up to the same temperature by the separate nozzle heater, which consists of two stages, allowing the tip of the nozzle to be molten only when everything else is ready, in an effort to reduce the chance of clogging.

Once the tin is liquid, the tank is pressurized with argon gas and the tin at the tip is molten by setting the heater to 270 °C. Typical argon pressures are 10–25 bar, depending on the nozzle orifice size and the desired droplet size. A cage system is present around the pressurized tin for safety in case of failure, shown in Fig. 4(b). Once pressure is applied and the tin at the tip is liquid, a stream of tin will immediately begin to flow out of the nozzle, entering the vacuum chamber with a velocity of ∼15 m/s. The stream is centered using the bellows and leaves the main Dalek chamber at the bottom*. This is where the Dalek chamber is connected to its vacuum pump, but also the 'catcher,' (indicated as (2) in Fig. 4) which is the intended collection place of all unused tin droplets†. The catcher is also heated to 270 °C to prevent the formation of stalagmites.

Droplet generation

The tin stream inherently breaks up as it travels through the vacuum chamber due to the Rayleigh-Plateau instability. Raleigh-Plateau breakup occurs in thin streams, such as our droplet stream or a shower. Depending on the velocity and the radius of the stream, different frequencies, which can be imagined as the distance between a bulge and a squeeze in the stream, grow faster, leading to chaotic breakup into droplets with a wide range of sizes. In the experiment, breakup is driven by a piezoelectric element integrated into the nozzle, which effectively squeezes the stream at a certain frequency and ensures the formation of droplets at this frequency and thus at a constant droplet size.

The size of the tin droplets depends on three main parameters. The first is the size of the orifice of the nozzle. The nozzle is picked before the experimental campaign to best match the desired droplet size. The orifice size and the flow velocity determine the rate of tin usage. Since the tin tank is limited to 1.3 kg, this also sets the length of the experimental campaign. In short, it is encouraged to use a small nozzle at lower pressures if possible, as it increases the measurement time‡. The main parameter to change the droplet size is the frequency applied to the piezo, as it can easily be changed during operation. The diameter of the droplets relates the frequency with

*At this point, by eye, the stream of tin looks like a line of silk.

†The lasers operate at 10 Hz, while the droplet breakup is in the kHz-range. Thus, most tin goes into the catcher.

‡And thus reduces stress on the experimentalist.

the relation $d \propto f^{-1/3}$ since the mass in the stream must be conserved. Thus, the full relation between the aforementioned parameters and the droplet size is (empirically)

$$d = A \times f^{-1/3}, \text{with } A \propto p^{0.25} \varnothing_{\text{NOZ}}^{0.71}, \tag{2}$$

where p is the argon backing pressure and $\varnothing_{\text{NOZ}}$ the nozzle orifice size. The parameter A is always experimentally determined by scanning the piezo frequency and recording the droplet size. Typical frequency values are 5–50 kHz. Higher values are possible, but they often give droplets that are too closely spaced to ensure that only one droplet is hit by the laser, while lower frequencies often do not give a stable breakup into equal droplets. Depending on the size of the chosen nozzle orifice and the argon backing pressure (here typically 10–25 bar), this can give droplet diameters ranging 20–50 µm with a typical uncertainty of ±0.5 µm. Combining the limited range of pressures (only 2.5x change possible) with the $1/4$ power law in Eq. (2) shows why changing the pressure cannot give large changes in droplet size, even though it can be easily changed experimentally. Additionally, changing the pressure will change the stream velocity, which impacts several factors such as the tin consumption, the spacing between the successive droplets, and also the triggering, which will be discussed next.

Triggering

With a stable stream in place*, the next step is to hit the droplet with a laser. The timing and repeatability of the laser-droplet interaction, also called the *laser-to-droplet* alignment, are critical for the experiment. For example, for a pre-pulse case that makes a sheet, laser-to-droplet alignment should be good enough to result in less than 1° tilt for the sheet. But since the droplets move at ∼15 m/s and are typically 20–50 µm in diameter, they move one diameter every ∼2 µs. Thus, for a high repeatability of the experiment, the laser needs to hit the droplet within 100 ns of the perfect moment, every time. Guaranteeing this high level of accuracy is solved by having the droplets pass through a horizontal line of continuous laser light, which scatters light that can be detected and used to trigger the laser(s). In more detail, the light is generated by an Integrated Optics 0633L-13A-NI-PT-NF diode laser, which emits 60 mW of 636 nm (red) light. This part is indicated as (3) and is shown schematically as 'CW' (continuous wave) in Fig. 4. The horizontal line focus, with typical full-width-at-half-maximum (FWHM) of 400 µm × 20 µm, is achieved using cylindrical lenses and allows for some movement of the stream left-right without losing signal strength. The scattered light is picked up by a Hamamatsu H10492-013

*The eye cannot resolve the stream but the microscopes will now show a steady breakup into identical droplets.

photo-multiplier tube (PMT, also shown in Fig. 4), which sits behind a band-pass filter to ensure it only picks up the diode light*.

The signal-to-noise ratio of this scattered signal is the key to <100 ns repeatability of the trigger†. Thus, the power of the continuous light should be high, the horizontal FWHM not too large (but also not too small to prevent constant adjustment being required as the stream moves slightly over time), and the vertical FWHM as small as possible. The first two increase the intensity of the light at the droplet, while reducing the vertical FWHM has a double effect. 1) It increases the intensity of light at the droplet, but 2) it also increases the 'steepness' of the scattered signal because the droplet will spend less time in the horizontal light sheet. Both are wanted to obtain the highest dV/dt, increase in signal over time from the PMT as possible. The higher this value, the less effect noise will have on the exact trigger moment, reducing the variability of the trigger moment t.

Four further details are important for the triggering system. First, this horizontal laser sheet is placed 3–6 mm above the center of the chamber. These few millimeters will give a 200–400 µs of travel time to the center of the chamber, where the droplet will interact with the pulsed laser, and thus enough time for the laser's pump-pulse cycle. Second, the triggering system is also used to down-sample the kHz scattering signal to 10 Hz, the frequency of the laser systems. Third, a 'backup box' is present in the triggering system. This box produces a 9.5 Hz triggering signal, but only when the 10 Hz signal is not present. This is required to ensure that the lasers keep running at a steady frequency in case of problems with the droplet stream, which is required to prevent thermal issues in the lasers.

Finally, a 'constant fraction discriminator' (CFD) signal processing device is used to improve triggering performance, in two main ways: by giving a droplet-size-invariant trigger and reducing the variation of the trigger moment. Figure 5 shows a schematic overview of the triggering system and explains the working principle of the CFD. The raw signal of the droplet passing through the sheet of light is a Gaussian temporally, with the width and height (which is tuned to be relatively constant using an adjustable attenuator) varying for different droplet sizes. Thus, a simple fixed threshold would result in different trigger timings. In the experiment, this would mean that the laser pulse would be misaligned after changing the droplet size. The CFD is used to find a droplet-size-invariant trigger moment. It does this by taking the original signal and subtracting a delayed and horizontally flipped version of itself from it. The zero

*Except for the plasma that follows, which emits all colors and therefore typically over-saturates the PMT, by a lot. Fortunately, this plasma follows the trigger and thus does not matter, since the PMT will have recovered by the next trigger, 100 ms later.

†At the time of writing, our record stands at 0.6 µm standard deviation in the position of the droplet after triggering, which is roughly 40 ns variation in the trigger timing at a droplet velocity of 15 m/s.

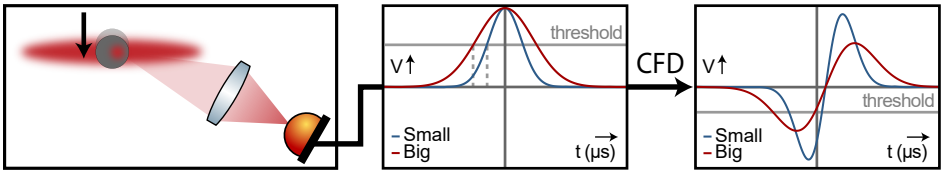

FIGURE 5: An illustration of the triggering system. A droplet passes through a horizontal line focus, and the scattered light is picked up by a lens and a photo-multiplier tube. The resulting signal, temporally, looks like a Gaussian, with a width and intensity depending on the droplet size. Thus, a constant threshold would result in shifting triggering points in time (dashed gray line). A constant fraction discriminator is used to obtain a size-invariant triggering point at the first zero crossing after a pre-trigger.

crossing of this new signal will not depend on the original width. Thus, the CFD device triggers on the first zero crossing after a pre-trigger (which prevents triggers on noise) to give a size-invariant trigger timing. Additionally, if one optimizes the delay of the horizontally flipped signal (which should be approximately the full-with-at-half-maximum of the original Gaussian), the slope of this signal will be maximized, resulting in even higher dV/dt and thus improved triggering performance.

Lasers and green shadowgraphy

The first laser to hit the droplet, in every chapter of this Thesis, is the 'pre-pulse' (PP, indicated as (4) in Fig. 4). The pre-pulse is focused down to a Gaussian spot with a single lens, with a typical FWHM between 80–105 µm depending on the application. This final lens is placed on an xyz-translation stage to allow for fine-tuning of the pre-pulse alignment. The z-axis needs to be tuned to ensure that the focus is on the position of the droplet. This is done by maximizing the laser-impact-induced propulsion velocity, which means maximizing energy-on-droplet, as thus minimizing the spot size.[47] The beam has a circular polarization for symmetric energy deposition, as ensured with a quarter waveplate, and its energy can be controlled with a waveplate-polarizer combination (not shown in Fig. 4). For Chapters 1–3, performed on Dalek-II, the pre-pulse is obtained from a Surelite III, outputting 10 ns Gaussian pulses. The Surelite III is stabilized using a MRC Compact Laser Beam Stabilization system to improve pointing stability and reduce long-term drifts of the laser beam focus position. For Chapter 4, performed on Dalek-I, the pre-pulse is a Spectra-Physics Quanta-Ray Pro-250, which also outputs 10 ns Gaussian pulses and has a built-in stabilization system. Both lasers are seeded, ensuring that the temporal profile is smooth, which is required to ensure that incompressible flow dominates over compressible flow,[48] resulting in sheet formation without excessive hole formation.

We image the experiment using stroboscopic shadowgraphic imaging systems, simply called 'shadowgraphy.' There are two types, green shadowgraphy and UV shadowgraphy. UV shadowgraphy (indicated as (6) in Fig. 4) was developed for Chapter 1 and used in Chapter 3 & 4. Since it is described in detail in Chapter 1, we will focus on the green shadowgraphy here. The green shadowgraphy starts with a Litron Nano S pulsed Nd:YAG laser outputting up to 50 mJ at 532 nm. This direct light is not usable for imaging as a result of its strong coherence. Thus, it is used to pump a Rhodamine 6G dye cell, which emits 5 ns pulses at 560 nm (with a bandwidth of 12 nm FWHM) through fluorescence. This light is brought to the experiment through up to three large multimode optical fibers (as the dye and Litron Nano S are located on another table). At this point, spatial coherence has reduced significantly, improving the quality of the image.[49] This light is sent through the chamber using a simple combination of lenses and mirrors, passing through the tin (indicated as (5) in Fig. 4). Thus, the shadow of the tin is imaged using the combination of a long-distance microscope (K2 Distamax) and a CCD camera (AVT Prosilica GT 2450). This system has a spatial resolution of 5 µm. Multiple fibers and cameras can be used to simultaneously image the tin at 30° and 90° angles with respect to the pre-pulse direction. We can set the exact timing of the shadowgraphy with ns precision using Stanford Research Systems DG645 boxes by changing the delay between the pre-pulse (or any other laser) and the shadowgraphy. Typically, 20–50 frames are taken at a certain time delay, to allow for filtering or averaging of the data in post-processing.

The final laser to hit the droplet is either the vaporization pulse (VP, Chapters 1–3) or the main pulse (MP, Chapter 4), excluding the shadowgraphy since that does not change the state of the tin. In brief, Chapter 1 uses a Litron Nano T, focused to a 'line' to vaporize a slice of the tin sheet. Chapter 2 uses an in-house-built laser[50] imaged to a spatial 'flat top' to vaporize the sheet homogeneously. Chapter 3 uses a Continuum Agilite 569-12, spatially focused to a Gaussian, much larger than the sheet with a FWHM of ∼1.5 mm. This spatial profile is also effectively flat at the sheet with only 5 % drop off in intensity radially. All these lasers are Nd:YAG-based 1 µm lasers, just like the pre-pulse lasers. Finally, Chapter 4 uses another in-house-built laser[51] emitting at 2 µm as the main pulse. Details of these lasers are described in their respective chapters.

Chapter 1

High-Resolution Spectroscopic Imaging of Atoms and Nanoparticles in Thin Film Vaporization

Dion Engels, Randy Meijer, Karl Schubert, Wim van der Zande, Wim Ubachs, and Oscar Versolato.
Applied Physics Letters **123**(25), 254102 (2023).

We introduce a spectroscopic absorption imaging method in the UV regime (225–400 nm) to study tin vapor created by irradiating a thin film with a low intensity 10^8 W/cm^2 nanosecond laser pulse, a case inspired by current developments around 'advanced target shaping' in industrial laser-produced plasma sources for extreme ultraviolet light. The 4-ns-time-resolved, 10-µm-spatial-resolution images contain a 10-cm^{-1}-resolution spectrum of the vapor in each pixel 100 ns after the vaporization. The images allow us to reveal a homogeneous temperature profile throughout the vapor of around 3000 K. We obtain a density map of the atoms (with a peak density of 5×10^{18} cm^{-3}) and nanoparticles (10^{12} cm^{-3} for the best fitting 20 nm radius case) which both are shown to be present in the vapor. For each free atom, approximately three appear to be clustered in nanoparticles, and this composition is invariant over space and density. The density and temperature maps of the free atoms are combined to estimate the electron density (peaking at 10^{13} cm^{-3}) in the vapor.

Optical diagnostics of plasma and vapor play a key role in the development of modern technologies. Notable examples include recent breakthroughs in tokamak fusion plasma, where multiplexed imaging provides necessary detail, e.g., of the scrape-off layer,[52–55] and EUV lithography, where active and passive spectroscopy methods led to key new insights.[18,28,56] The diagnostics employed so far have focused either on spectroscopic resolution, to identify contributing electronic states in atoms and ions, or on imaging resolution, to, e.g., pinpoint the precise location of high-temperature plasma areas.[57,58] This focus typically comes with trade-offs between imaging and spectroscopic resolution, or with the necessity to employ tedious spatial raster scans to combine sufficient resolution on both fronts.[59–62] The use of liquid tin as laser-plasma targets in EUV lithography [63,64] and plasma divertor shielding in fusion [65–67] motivates the development of direct optical diagnostics that combine high spatial and temporal resolution with high-resolution spectroscopy of tin vapor that may comprise atoms as well as nanoparticles.

In this work, we introduce a method of UV spectroscopic absorption imaging that combines ~10 µm spatial, 4 ns temporal, and a 10/cm spectroscopic resolution that enables identifying the composition of tin vapor. We develop and apply the method to the field of tin target shaping, relevant to the production of EUV light using laser-produced plasma (LPP).[64] Specifically, we use a 10^8 W/cm^2 nanosecond-duration laser pulse to experimentally create a vapor from a thin film, which is imaged using the method, and to determine the vapor's state of matter. Target shaping, i.e. creating thin tin sheets from droplets, is used for the LPPs to increase EUV generation efficiency.[35] Even larger efficiency gains, in converting more laser light into useful EUV photons, could be obtained with improved, 'advanced' target shaping.[34] Inspired by this concept, we here investigate targets pre-shaped by a further laser pulse to create a tin vapor [38] that may improve the interaction with the main pulse and increase the conversion efficiency (analogous to the pre-plasma suggested in Refs. [68, 69]).

In the experiment (see Fig. 1.1), a train of tin microdroplets (T = 270 °C in the current experiments) is generated using a droplet generator mounted on top of a vacuum chamber (10^{-7} mbar). The droplet stream passes through a sheet of light a few millimeters above the vacuum chamber center. Scattered light at a kHz-rate is picked up by a photo-multiplier tube and downsampled to 5 Hz to trigger the experiment. For more details of the experimental setup, see previous work.[38,70]

A microdroplet (diameter set to ~30 µm) is first hit by the pre-pulse [PP, 10 ns, λ = 1064 nm, cf. Ref. [71], and see Fig. 1.1(a)]. Spatially, the PP is focused to a Gaussian spot size of approximately 100×100 µm (FWHM, full-width at half-maximum). The droplet is propelled by the PP and expands into a thin sheet.[70,72]

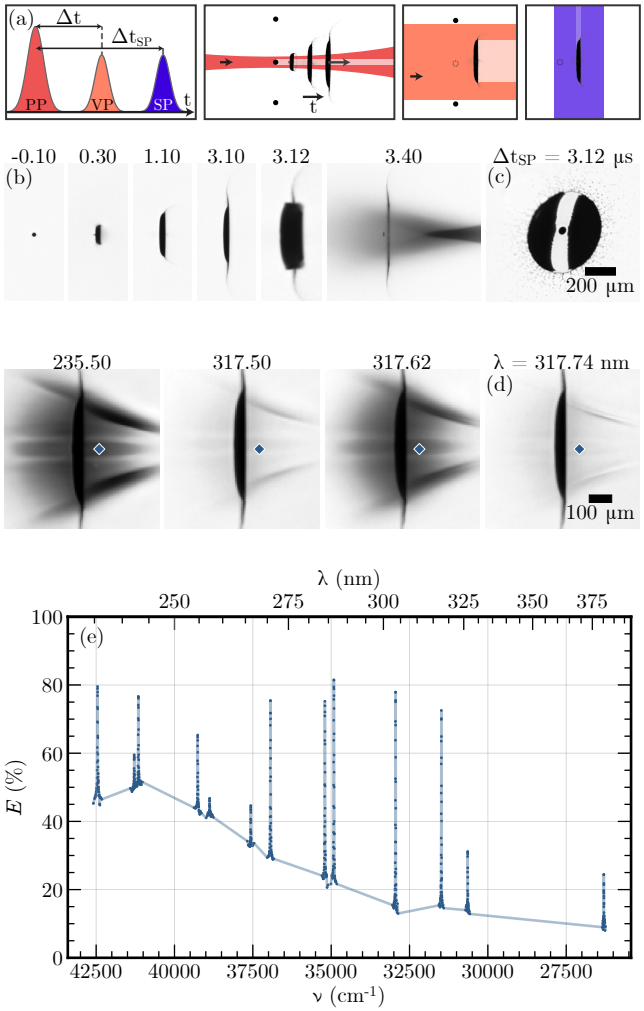

FIGURE 1.1: (a) Time-ordering of the three laser pulses used in the experiment. First, the tin microdroplet is hit by a pre-pulse (PP), propelling the droplet and expanding it into a thin film. At a set time (Δt), this thin film is irradiated with the vaporization pulse (VP), creating the tin vapor. The tin vapor is imaged using the shadowgraphy pulse (SP). (b) Processed side-view shadowgrams created with 284.08 nm-backlighting at different times after the PP. The VP hits 3.1 µs after the PP. (c) Front view of the thin film (at 30°, showing the *line* focus of the VP, to control absorption path length. (d) Side-view shadowgrams at various SP wavelengths, 100 ns after the VP. (e) Extinction (E) spectrum for the location indicated by the blue dot in panel (d).

At a set time after the PP, here 3.1 µs, the sheet is irradiated with a 0.5 mJ ns-length vaporization pulse (VP, $\lambda = 1064$ nm). At this time, the sheet has a thickness of 50–20 nm (decreasing radially outward).[38] The VP is focused to a *line* focus using a cylindrical lens and has an FWHM of 1100×70 µm, to define a common interaction length of the side-view shadowgraphy. The energy of the VP is carefully tuned to ensure vaporization occurs without significant ionization of the tin as evidenced by the absence of any signal on Faraday cup ion detectors.

Finally, the vapor is imaged using two synchronous shadowgraphy pulses (SP). A front-view image (at 30°) is taken using 560 nm light to check proper droplet-to-laser alignment.[38] The light for the side-view image at 90° comes from a Continuum Horizon OPO laser here generating wavelengths between 225–400 nm, with a pulse length of 4 ns, a spectral bandwidth of 5–10 cm^{-1}, and a spatial resolution of between 5 µm and 10 µm depending on the wavelength. Fig. 1.1(b) shows the evolution of the tin target from microdroplet to vapor using side-view UV shadowgraphy, while (c) shows the front view from the green shadowgraphy after the VP has hit.

For each UV shadowgraphy wavelength, we average over 50 frames (in our stroboscopic method, each frame corresponds to a different droplet), after correcting for minor tilt and alignment changes. This reduces the visibility of coherence 'speckle' and increases the signal-to-noise ratio. The images obtained at different wavelengths are scaled to a global magnification value (magnification changes with wavelength due to the chromatic, single-lens-imaging setup). All CCD pixels are binned into 4 by 4 bins (in the following referred to as a pixel) to reduce the impact of any remaining misalignment, resulting in an effective spatial resolution of 10 µm. Fig. 1.1(d) highlights the range of wavelengths allowed by the OPO laser and the changing contrast of the vapor. These and all subsequent images are taken with 100 ns between the VP and the shadowgraphy.

Fig. 1.1(e) shows the extinction spectrum for the location indicated by the blue marker in panel (d). A broadband contribution is present, decreasing toward longer wavelengths. This we attribute to the presence of nanoparticles as we will describe below.[73–75]

Furthermore, strong Sn-I atomic resonances are visible, proving the presence of free atoms in the vapor (see Supplementary Material Note 1 for an overview of resonances[76]).[77–79] The electronic levels probed can be seen in the Grotrian diagram in Fig. 1.2(a). These atomic resonances enable the extraction of the temperature of the vapor using a Boltzmann plot.[56,80] To do so, the broadband contribution is removed to obtain the atomic contribution to the extinction spectrum, E_{atom} [see Fig. 1.2(b)]. Next, we calculate the area under the logarithm of E_{atom} for each atomic resonance and use this as the metric for the line strength S. This line strength can be related to

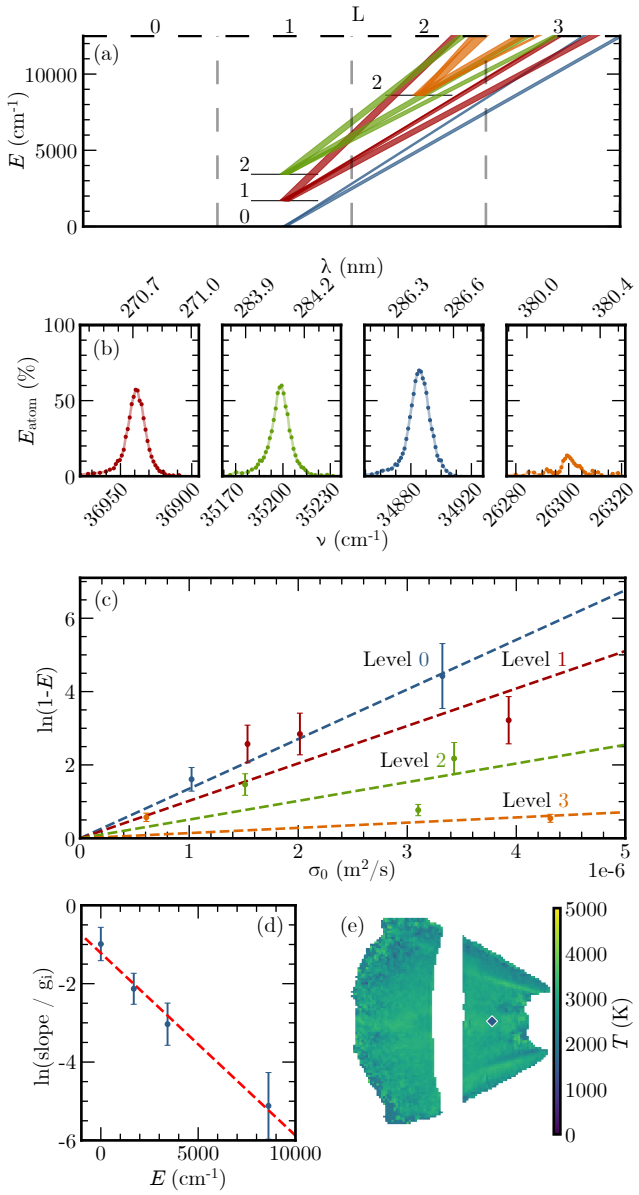

FIGURE 1.2: (a) Grotrian diagram. Only the ground level of neutral tin $5s^25p^2$ is shown for clarity. The four energy levels probed in the experiment are also shown. The different colored lines are resonances from these levels to higher levels (not shown). The numbers next to the levels indicate the total angular momentum quantum number J. (b) Extinction around several atomic resonances when the broadband term is subtracted (E_{atom}). The plot colors relate to the ground levels of the resonances in panel (a). (c) σ_0 versus $\ln(1-E)$ integrated over the resonance. See the main text for information. (d) Boltzmann plot with fit of the four levels based on the slopes in panel (c) for the pixel indicated in panel (e). (e) Resulting temperature map for the entire vapor.

the Boltzmann population fraction $b(T)$

$$S \equiv \int -\ln(1 - E(\nu))d\nu = n_0 L \chi(\nu) b(T) \sigma_0. \tag{1.1}$$

Here, σ_0 is the base resonance cross section (see Supplementary Material Table S1[76]), n_0 is the total atom density, L the common path length through the vapor [$\sim$100 µm, obtained from images like Fig 1.1(c)], and taking $\chi(\nu)$ as a common broadening factor. Plotting S versus σ_0 gives a straight line, of which the slope is set by the Boltzmann population fraction [see Fig. 1.2(c)].

We assume that no other higher-lying levels than those shown in the Grotrian diagram are occupied (the next level lies at 17 162 cm^{-1}). This allows us to calculate the occupation of the levels based on the fit slopes, with the common factors n_0, L, and $\chi(\nu)$ dividing out and, thus, our treatment is independent of their specific numerical values. These occupations are then fit with a Boltzmann distribution, resulting in a temperature, see Fig. 1.2(d).

Having demonstrated the process above for a single pixel, we next apply it to the full image to create a temperature map. The result, presented in Fig. 1.2(e), reveals a relatively uniform temperature around 3000 K. Small deviations from a homogeneous temperature can be seen in high-extinction areas [cf. Fig. 1.1(d)]. These deviations may point to temperature increases in colliding vapor flows, or potentially to differences in $\chi(\nu)$ between resonances becoming more apparent at high densities. In general, both (i) the non-trivial spectral shape of the OPO laser and (ii) the uncertainty in the assumption of constant density broadening contribute to a conservative overall systematic uncertainty of approximately 20 % on the data points in Fig. 1.2(c). This uncertainty propagates through the fit [cf. Fig. 1.2(d)] to result in an uncertainty in the order of 100 K in temperature T [Fig. 1.2(e)]. With this in mind, we note that the temperature can be considered to be relatively uniform and close to the boiling temperature of tin of 2875 K.

Having obtained the overall temperature map, we next extract the local density, which together with the temperature and the composition defines the state of matter of the target material. Fig. 1.3 shows extinction spectra for selected locations, indicated by the dots in Fig. 1.3(a-c). As shown in Fig. 1.3(d), the individual spectra are very similar, with the only clear difference being the total extinction. This similarity can be further investigated by introducing the relative density (a) and relative cross section (σ_{rel}). To do so, Beer-Lambert's law [81,82] is inverted to an equation for the cross section: $\sigma(\nu) = -\ln(1 - E(\nu))/nL$. Again, n is the density of the material and σ its extinction (absorption + scattering) cross section, and L is the (common) path length through the material.

A relative density a can be defined for any two pixels in an image by comparing the $\ln(1 - E(\nu))$ between the two locations, following Schupp *et al.*[83] The advantage of relative densities is that we do not require any underlying model for the cross section. Fig. 1.3(e) shows $\ln(1 - E(\nu))$ to highlight the non-linearity of Beer-Lambert; the atomic resonances become more pronounced when taking the logarithm since these have very high extinction values.

We fit the broadband extinction spectrum of each pixel to the spectrum of a single reference pixel (defined as $a = 1$), obtaining a single (wavelength independent, unitless) value a: an overall multiplicative factor that minimizes the difference between the logarithms of the individual spectra of panel (e) and the reference spectrum. Fig. 1.3(f) shows the result of the fit procedure for the selected positions expressed as a relative cross section, σ_{rel}, defined as $\sigma_{\mathrm{rel}}(\nu) = -\ln(1 - E(\nu))/a$. We set $\sigma_{\mathrm{rel}}(\nu) = 1$ for the reference pixel at the longest wavelength (381 nm).

Fig. 1.3(g) shows the same results with the atomic resonances filtered out for improved visibility. Besides the selected locations, the mean σ_{rel} with uncertainty bounds are also plotted to highlight the collapse of *every pixel* in the vapor to the same curve. With this, we reveal the striking fact that the spectra are spatially invariant and, thus, that the underlying nanoparticle size distribution that causes the broadband extinction curve is the same everywhere in the vapor.

We next plot the values obtained for a in Fig. 1.3(b), showing a strong correlation with the original shadowgraph in panel (a). An atomic equivalent to the method above can be defined by comparing the area under the logarithm of E_{atom} [following Fig. 1.2(c)] between different pixels to again obtain a single a as an overall multiplicative factor. The results are presented in Fig. 1.3(c). Remarkably, the two means for obtaining the relative densities a produce extremely similar spatial profiles, comparing panels (b) and (c). This indicates that the nanoparticles and free atoms move together and that the densities, ranging over an order of magnitude, have no influence on the composition of the vapor itself – the composition appears to be *frozen in*.

The total number of atoms in the vapor can be estimated, taking as input the known cross section of the resonances and the constant path length (100 µm). Further, we take a linear scaling of the broadening $\chi(\nu)$ with density.[84] Using this, an absolute density map can be obtained (which is indistinguishable from Fig. 1.3(c) and therefore not shown) and peaks at 5×10^{18} cm^{-3}. Summing over the full map (i.e., integrating over the entire measured volume) results in a total number of 1×10^{13} atoms in the vapor. This number represents approximately 40 % of the total number of vaporized atoms when compared to the prediction from the sheet thickness model of Liu *et al.*[38]

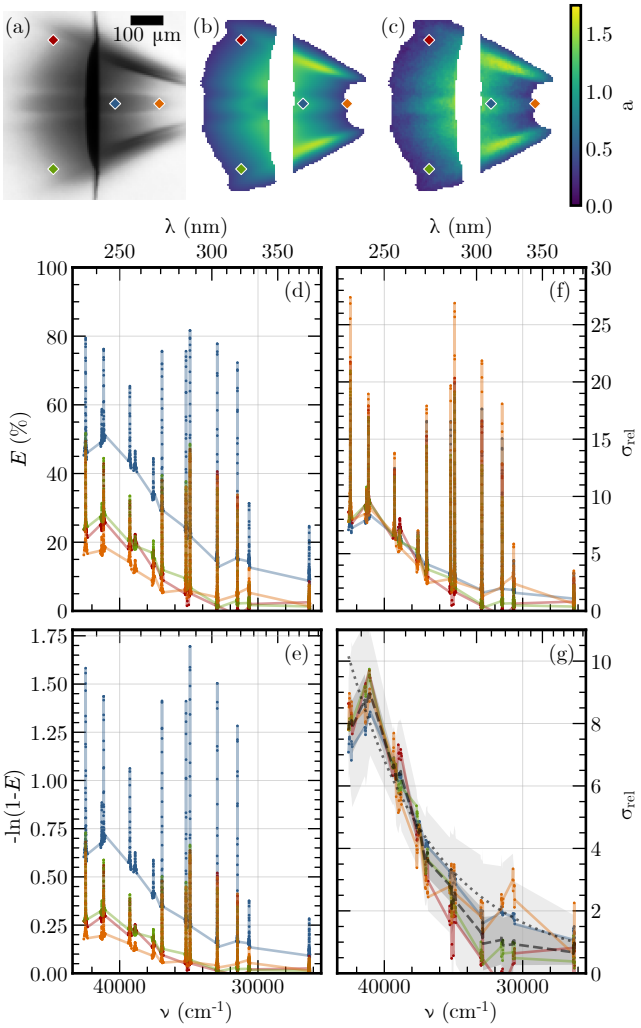

FIGURE 1.3: (a) Image of the vapor at 284.08 nm (on an atomic resonance). Four different locations for which the curves are shown in (d-g) are indicated. (b-c) Relative, unitless, densities a determined using the broadband extinction curve (b) or the atomic resonances (c). (d) Extinction for the four locations. (e) $-\ln(1-E)$ for the four locations. (f) Relative cross section (σ_{rel}) for the four locations. (g) Relative cross section (atomic resonances filtered out). Mean (gray, dashed) for all pixels and uncertainty bounds (at 1 and 3 standard deviations, gray shading) are also indicated. The dotted gray line indicates the best-fitting nanoparticle radius of 20 nm.

A similar estimate can be made for the broadband component of the spectrum caused by nanoparticles. We use a numerical code [85] (cross-checked with an alternative code [86]) for Mie theory [73,74] to obtain extinction cross sections, which includes both absorption and scattering, for nanoparticles (typically valid for sizes above 40–100 atoms, a radius of 1–3 nm).[75,87,88] Refractive index data is taken from Cisneros *et al.*[89] and extrapolated to wavelengths below 310 nm (4 eV) using a Drude-model fit.[90] The dotted gray line in Fig. 1.3(g) indicates the best-fitting nanoparticle radius of approximately 20 nm, obtained from a least-squares fit of the cross section predicted by Mie theory to the collapsed relative cross section, with the particle radius being the single free fit parameter. We note that Mie extinction has near-equal contributions from absorption and scattering in this size regime. A nanoparticle density of approximately 10^{12} cm^{-3} is obtained when taking the σ of a 20 nm radius nanoparticle. This means that a total number of $3(1) \times 10^{13}$ atoms are clustered in nanoparticles to create the broadband spectrum, which is close to the total number of atoms in the vaporized thin film (3×10^{13}).

The dominant uncertainties pertain to (i) the extrapolated refractive index and (ii) the estimated number of vaporized atoms. More atoms may be vaporized from parts of the thin film that did not become transparent after the laser pulse. Additionally, the atomic broadening, hidden by the complex spectral shape of the UV laser, adds uncertainty to the atomic density calculation.

Critically, we learn from this that for every free atom, several others (approximately three) are clustered in nanoparticles. We note that this estimate is relatively independent of the precise radius of the nanoparticles, with the cross section per atom being relatively constant in this range. This independence extends to below the strict validity range of Mie theory as well, providing strong support for the statement that only one out of three atoms are 'free' with the remainder bound in nanoparticles.[75]

The obtained densities and temperatures of the atoms can be combined to obtain a local electron density (which is an important quantity for laser absorption in media, and thus for the industrial application of EUV generation) within the vapor using the Saha-Boltzmann equation.[91] Given the rather uniform temperature profile [cf. Fig. 1.2(e)], this local electron density closely follows Fig. 1.3(c) and yields a maximum electron density of approximately 10^{13} cm^{-3}, six orders of magnitude below the critical electron density for a 10 µm-wavelength CO_2 main pulse. Only under EUV-generating conditions, when high tin charge states (Sn^{10+} – Sn^{14+}) are generated, does the atomic vapor reach the critical density—enabling sustaining the plasma, with laser light absorbed via the inverse Bremsstrahlung mechanism,[44] but not explaining its 'ignition'. The current vapor could still offer an effective advanced target in EUV sources given that nanoparticles may instead 'ignite' the plasma, leading to

rapid ionization and the formation of a critical surface. Additionally, the increased laser-material interaction length scale may promote laser absorption.

Besides the value of our method to diagnose tin vapor targets, the observed broadband extinction spectrum with its spatial invariance and density independence may provide insight into the vapor production mechanism. Two well-known mechanisms are (i) Hertz-Knudsen evaporation and (ii) homogeneous nucleation (also known as phase explosion or explosive boiling).[92–97] Our detailed calculations (see Supplementary Material Note 2[76]) indicate that vaporization following the Hertz-Knudsen equation can explain the observed rate of double-sided vaporization (dividing the typical thickness ~25 nm by the 6 ns VP pulse length [38]) when taking as input the tin vapor pressure in vacuum [98,99] and assuming a surface temperature of approximately 4000 K. We note that this temperature, while sufficient to explain the observed vaporization rate, lies well below the thermodynamic critical temperature (which is between 7073 K and 8800 K for tin [100,101]) and is very close to the observed late-time temperature obtained from Fig. 1.2. Since vaporization following the Hertz-Knudsen model only describes the formation of free atoms,[95,97] any nanoparticles must have been formed through coalescence processes which we may hypothesize to lead to a broad range of cluster sizes. The production of particles with the current best-matching radius of 20 nm is not fully understood from this picture. Smaller objects, specifically clusters Sn_n ($n = 6...40$), exhibit extinction cross section spectra,[75] dominated by absorption, that can produce broadband responses similar to the observed broadband component.

The much more violent process of homogeneous nucleation, which occurs when the liquid is heated close to thermodynamic critical temperature,[93] may well explain the formation of larger nanoparticles. Typical reported nanoparticles sizes resulting from homogeneous nucleation range 5–25 nm [102–107] similar to the current observation. Homogeneous nucleation leads to rapidly expanding gas bubbles expelling nearby liquid mass and thus creating nanoparticles.[107] The used VP intensities in our experiment heat the thin film at a rate of approximately 10^{12} K/s. At these intensities and time scales, homogeneous nucleation has been observed previously.[108] The identification of the underlying vaporization mechanism is, thus, strongly intertwined with the origin of the broadband extinction spectrum. Future work could probe the thin-film vaporization process in a time-resolved manner, thereby enabling the separation of the two vaporization mechanisms, with the longest VP and shortest possible SP pulses maximizing the effective temporal resolution, employing the method introduced in this work.

In conclusion, we introduce an optical diagnostic method for characterizing the composition of a vapor based on UV spectroscopic absorption imaging. We use the method to study tin vapor created by irradiating a thin film with a laser; a case inspired

by industrial LPP EUV sources. We obtain high-resolution images containing a high-resolution spectrum for the vapor in each pixel. Using our spectroscopic imaging method, we reveal a rather homogeneous temperature profile throughout the vapor, close to the boiling temperature of tin, and obtain a density map for atoms and nanoparticles, both of which are shown to be present in the vapor. For each free atom, several others appear to be clustered in nanoparticles and the composition appears to be frozen in. We combine the density and temperature maps for free atoms to obtain the electron density in the vapor, which is highly relevant to industrial applications. Finally, besides the clear value of our method to quantify tin vapor targets for industrial applications in EUV lithography and fusion alike, it may also provide more general insight into vapor production mechanisms under extreme conditions and can also be applied to broader studies of the dynamics of phase changes in free-standing thin films.

Acknowledgments

This work has been carried out at the Advanced Research Center for Nanolithography (ARCNL). ARCNL is a public-private partnership with founding partners UvA, VU, NWO-I, and ASML, and associate partner RUG. The authors thank Niek Lopes Cardozo, Michael Purvis, and Haining Wang for valuable discussions and ASML for loaning a laser system. We would also like to thank Henk-Jan Boluijt and Laurens van Buuren for their work on the experimental setup.

This research was funded by the European Research Council (ERC StG 802648) and the Nederlandse Organisatie voor Wetenschappelijk Onderzoek (OTP 19458).

Chapter 2

Scaling Relations in Laser-Induced Vaporization of Thin Free-Flying Liquid Metal Sheets

Karl Schubert*, Dion Engels*, Randy Meijer, Bo Liu, and Oscar Versolato.
Physical Review Research **6**(2), 023182 (2024).

We experimentally study the vaporization of free-flying liquid tin sheets when exposed to a 100 ns laser pulse with an intensity between 0.2–4 $\times 10^7$ W/cm^2, a case inspired by current developments around 'advanced target shaping' in industrial laser-produced plasma sources for extreme ultraviolet (EUV) nanolithography machines. Our findings reveal a gradual vaporization and a linear relationship between the average vaporization rate and laser pulse intensity (with a prefactor of 1.0(3) 10^{-7} ms^{-1}/Wcm^{-2}), for various targets ranging 20–200 nm in thickness. We introduce a numerical 1-D heating and vaporization model based on Hertz-Knudsen evaporation and find excellent agreement between simulations and experimental data. We furthermore demonstrate that the amount of vaporization of liquid tin targets in the investigated laser intensity range is governed solely by the deposited fluence, and collapse all data onto a single non-dimensional curve — enabling the accurate prediction of vaporization dynamics in applications in future development of EUV sources.

* These authors contributed equally to this work. Dion participated in the experiments and was in charge for the theoretical and modeling part of this work.

Introduction

Improvements in semiconductor devices are driven by advances in state-of-the-art nanolithography machines that generate and utilize extreme ultraviolet (EUV) light. This EUV light is produced by the irradiation of 'mass-limited' liquid tin micro-droplets with a double laser pulse scheme.[35,63,64] First, thin liquid tin sheets ('targets') are produced from droplets using a ns laser 'pre-pulse' (PP).[39,47,70–72,109,110] Picosecond pre-pulses have also been explored in this context previously.[63,64,111] This first step enhances EUV light generation in a second step where an energetic 'main pulse' (MP) produces a plasma.[35,64] Further efficiency gains in the conversion of MP laser photons into relevant EUV photons in laser-produced plasma (LPP) could potentially be obtained by using 'advanced' target shaping approaches.[35] Such approaches may include using, e.g., a laser-generated 'pre-plasma' as suggested in Refs. [68, 69].

Inspired by such concepts, Liu *et al.*[38] and Engels *et al.*[76] investigated ns laser-vaporization of tin sheet targets with some direct relevance to the industrial use case. More specifically, Liu *et al.*[38] used laser-induced vaporization to uncover previously invisible but important features of the target, such as the center mass and the rim bounding the sheet,[39] and proposed scaling relations (relating, e.g., vaporization times to local sheet thickness) in the underlying dynamics. However, no mechanism was identified and no direct experimental evidence was yet provided in support of the scaling relations. There is a range of literature for metals that are subject to ns laser pulses, where three relevant processes can be been identified, namely (a) boiling, (b) vaporization, and (c) phase explosion.[93–95,97] Normal boiling (heterogeneous nucleation), perhaps the most intuitive and well-known response of a hot liquid, can be ruled out because of the (µs) long time scales involved in the diffusion of vapor bubbles to the surface,[94,95] leaving only vaporization (described by the Hertz-Knudsen equation) and phase explosion (also known as explosive boiling or homogeneous nucleation) as viable options. The work of Engels *et al.*[76] focused on spectroscopic analysis of vapor that was laser-produced from tin targets. The vapor was found to have a homogeneous temperature distribution averaging approximately 3000 K and to contain both atomic and nanoparticulate tin. The observation of the rather low-temperature vapor (near the 2875 K boiling point to tin) may fit a gradual Hertz-Knudsen-type vaporization mechanism and could tentatively be interpreted to rule out phase explosion as a mechanism.[76] However, the authors indicated that the presence of nanoparticles could in fact perhaps best be explained by explosive boiling, thus leaving the vaporization mechanism as an open question.

The prior recent works by Liu *et al.*[38] and Engels *et al.*[76] provide a strong basis but leave significant gaps in the understanding of the vaporization dynamics in qualitative (i.e. the vaporization mechanism) and quantitative (i.e. the scaling relations) terms.

Addressing these gaps will benefit and steer ongoing developments in improving LPP EUV sources. In this study, we address these gaps in understanding by employing two distinct methods to quantify the vaporization process initiated by an auxiliary laser pulse following a PP, for a range of intensities ($0.2–4 \times 10^7$ W/cm^2) and a range of target types and thicknesses (20–200 nm). Our approach involves using a long (100 ns) auxiliary vaporization pulse (VP) with a temporal and spatial box pulse profile. We image the vaporization during this long pulse stroboscopically using a 'shadowgraphy' technique with 5 ns temporal resolution. The obtained data is employed to demonstrate that the sheet gradually vaporizes (following Hertz-Knudsen evaporation) and to quantitatively study scaling relations to enable predictive modeling of the dynamics.

Experiment

Our experimental setup has previously been described in detail.[38,46,70] Here, we present a summary. In the experiment (Fig. 2.1) a kHz train of liquid tin droplets (temperature 270 °C in the current experiments) set to a diameter $D_0 \approx 27$ or 35 µm is vertically dispensed in a vacuum environment (10^{-7} mbar) by a droplet generator. These droplets pass with a speed of the order of 10 m/s through a horizontal sheet of light that is produced by a continuous-wave HeNe laser and positioned a few mm above the center of the vacuum chamber and thus above the laser-droplet interaction point. This light is scattered by the droplets and detected by a photomultiplier tube. Subsequently, the kHz signal is down-sampled to 10 Hz and serves as a trigger for the start of the experiment.

Figs. 2.1(a–d) present a schematic of the laser pulse scheme. First, a droplet is hit by the pre-pulse [$\lambda = 1064$ nm, circularly polarized]; Fig. 2.1(a) shows the typical response of the droplet to such PP impact. The PP is generated from a seeded Nd:YAG laser system (Continuum Surelight III) that emits temporally Gaussian intensity pulses with a duration of about 10 ns at full width at half-maximum (FWHM). The PP is focused to a Gaussian spot size of approximately 100 µm (FWHM) at the droplet location (at the center of the vacuum chamber). The PP creates a plasma on the droplet, exerting pressure on the remaining liquid tin, which rapidly propels and expands on the order of several 100 m/s to a thin axisymmetric sheet.[47,70] The propulsion, with a velocity U, is oriented along the propagation direction of the laser, while the orthogonal radial expansion starts with an initial velocity $\dot{R}_0$ at $t = 0$ that is subsequently reduced until it leads to sheet contraction due to the surface tension that is exerted on the edge of the sheet.[70,72,112] The timescales that set both accelerations are similar to the duration of the laser pulse (ns) and are much shorter than the timescale of the subsequent fluid dynamic deformation (µs).[70,72]

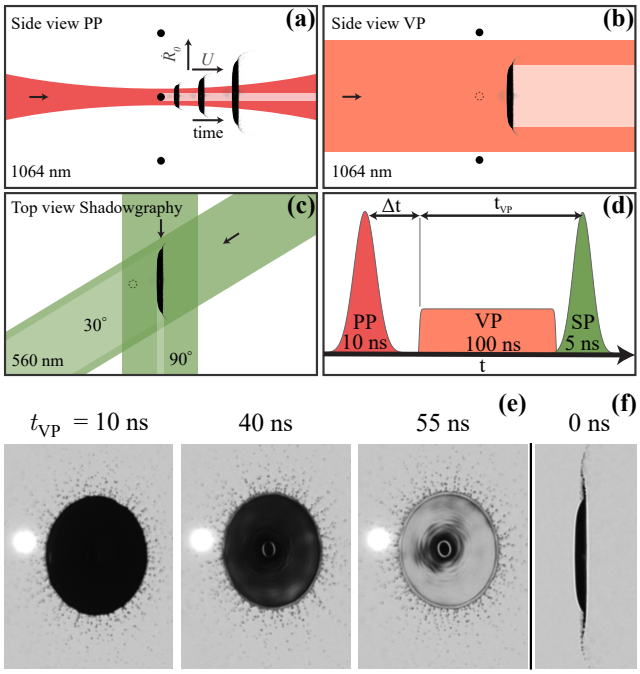

FIGURE 2.1: (a-d) Illustration of the laser pulse schemes with their irradiation geometries. (a) Side-view schematic of the pre-pulse (PP) including the tin droplet dynamics of propulsion and expansion resulting from the interaction of PP and the spherical liquid tin drop. (b) Side-view schematic of the vaporization pulse (VP) that irradiates a liquid tin target. (c) Top-view schematic of the shadowgraphy illumination pulses. Arrows indicate the viewing angle. (d) Laser pulse scheme in time, starting with the PP that is followed by the VP after Δt. At time $t = 0$ the PP initiates the droplet deformation process. The time $t_{VP} = 0$ indicates the onset of the VP. The shadowgraphy pulse (SP) is scanned in time over the ongoing VP irradiation of the liquid tin target to capture the vaporization dynamics. (e) A series of front-view green shadowgraphs (at 560 nm) of the thinnest target (B_{II}, see Tab. 2.1) during irradiation by the VP for different t_{VP} with a VP energy $E_{VP} = 2.5$ mJ. The bright spot visible on the left-hand side in the shadowgraphs is due to the PP-induced plasma, the intense radiation of which causes saturation of the CCD chip. (f) Green side-view shadowgraph before irradiation with the VP. PP and VP impact from the left.

Following Klein *et al.*[113] and Liu *et al.*[71] we obtain the initial radial expansion speed $\dot{R}_0$ by fitting a linear function through the first three tracked data points of the liquid tin sheet radius, avoiding shadowgraphs with a strong imaging influence of the PP plasma. A higher E_{PP} causes a higher $\dot{R}_0$, hence less time is required to obtain a certain sheet size D_s.[71]

Inspired by previous work,[38] we start our studies on a liquid tin target that provides thickness ranges between 20 nm and 30 nm (according to semi-empirical thickness model predictions following[71] for a 25 mJ PP on a 27 µm diameter droplet) and refer to it as target B_{II} consistent with Ref. [38] (for more information about the targets used see Tab. 2.1). Note that the variation in sheet size is very small, with the relative standard deviation of the B_{II} target size being approximately 1 %. We continue our study on a thicker target for the same conditions (i.e., using the same PP and droplet size) but 1 µs prior to the target B_{II} and call it for consistency B_I. This target B_I carries more mass than B_{II} given the continuous mass loss during expansion.[71,114] It also exhibits a stronger thickness gradient along the radial coordinate compared to B_{II}, providing a thickness range between 20–50 nm.[71] By increasing the PP energy (E_{PP} = 56 mJ) we extend our study to a thicker target, achieving a similar D_s but thicker target at even earlier times (Δt = 1.2 µs). This target is labeled target A[38] with a 50–150 nm thickness range. Lastly, we shoot a significantly stronger PP (E_{PP} = 100 mJ) at a larger 35 µm diameter droplet and thus create a target 'C' with an approximate 70-250 nm thickness range.[71] Tab. 2.1 also provides non-dimensional times $\Delta t/t_c$ using the capillary time $t_c = \sqrt{(\rho D_0^3)/(6\sigma)}$ which sets the typical time scale for expansion and subsequent retraction, with as input ρ from Tab. 2.2 and σ = 0.54 N/m. The non-dimensional apex time for liquid tin droplets is approximately $\Delta t/t_c \sim 0.4$.[112] This means that only target B_{II} has passed its expansion apex.

In summary, we create different targets to access profiles of different thicknesses (see

Target	D_0 [um]	E_{PP} [mJ]	$\dot{R}_0$ [m/s]	Δt [us]	$\Delta t/t_c$	D_s [um]
A	27	56	227	1.2	0.19	396
B_I	27	25	171	2	0.31	382
B_{II}	27	25	171	3	0.46	391
C	35	100	208	1.2	0.13	449

TABLE 2.1: Table of targets used in the experiments with columns of their initial droplet diameter D_0, pre-pulse energy E_{PP}, initial expansion speed $\dot{R}_0$, time in expansion trajectory Δt, non-dimensional time $\Delta t/t_c$ (see the main text), and the column for their sheet diameter D_s.

Tab. 2.1 above, and Fig. 2.7 in the Appendix for more details) enabling the study of the vaporization dynamics over approximately an order of magnitude in thickness.

We next irradiate these targets with a vaporization pulse with a duration of 100 ns [$\lambda =$ 1064 nm, circularly polarized, see Fig. 2.1(b)]. The VP is produced by a laser system with arbitrary sub-nanosecond pulse shaping capabilities.[50] The VP laser system generates temporal box-shape pulses of approximately 100 ns and is imaged to a spatial top-hat shape at the center of the vacuum chamber with a size of approximately 820 µm×820 µm. We use photodiodes (PDs, DET025AL/M) to monitor the VP before entering the measurement chamber, and after transmitting through the chamber. Both laser pulses (PP, VP) are collinearly aligned onto the droplet.

To observe the interaction of the liquid tin sheet with the VP, an imaging setup is used, which is described in detail in Ref. [46]. Briefly, it consists of a dye-based illumination source and CCD cameras that are coupled to long-distance microscopes, yielding a spatial resolution of approximately 5 µm. The illumination source produces pulses with a duration of 5 ns (FWHM) and a spectral bandwidth of 12 nm (FWHM) at 560 nm. We use two synchronous shadowgraphy pulses (SP) for backlight illumination of the front- and side-view acquisitions [at 30° and 90° concerning the laser axis, respectively, see Fig. 2.1(c)] to capture the liquid tin sheet dynamics. Fig. 2.1(d) depicts the time sequence of the aforementioned pulses, highlighting the fact that the SP is scanned (in delay steps) over the ongoing VP ($t_{\mathrm{VP}} = 0$ marks the start of the VP); the VP itself impacts at a time Δt after PP. During each delay step, we record 20 frames in a stroboscopic manner, each representing a different laser-droplet interaction event. This allows us to apply post-filtering techniques, e.g., for selecting sufficiently good laser-to-droplet alignment. The excellent reproducibility of the experiment (showcased, e.g., in the small variation in target sheet size) allows the majority of the collected frames to be used for averaging in the following. Fig. 2.1(e) presents front-view shadowgraphs during VP-induced vaporization with $E_{\mathrm{VP}} = 2.5$ mJ, at various t_{VP}. The shadowgraphs clearly show the presence of the sheet's main features: center mass, bounding rim, ligaments, and fragments.[71] We observe gradual mass removal from the sheet with increasing t_{VP} through the increase in transparency of the sheet to shadowgraphy backlight illumination (see Ref. [38]). Fig. 2.1(f) shows the side-view shadowgraphy of the same target before VP impact at $t_{\mathrm{VP}} = 0$.

Results

First, we investigate the vaporization dynamics of the thinnest target $\mathrm{B_{II}}$ using its partial transparency to the green shadowgraphy backlighting. We introduce a 1-D

vaporization model based on the Hertz-Knudsen equation. Next, we characterize also the thicker targets. Lastly, we combine and generalize observations of all targets.

Characterization of target B_{II} using partial transparency of the sheet

In Figure 2.2(a), a heat map is presented that shows the transmission of background light through the target B_{II} for $E_{VP} = 2.5$ mJ. This heat map illustrates the variation in transmissivity as a function of t_{VP}, here taken along a vertical lineout passing through the center of the target [cf. Fig. 2.2(b)]. These lineouts are aligned and averaged per delay step. The heatmap shows that as t_{VP} increases, the target gradually becomes more transparent, indicating a gradual thinning process. The choice of a logarithmic scale is motivated by the near-exponential scaling of the absorption of shadowgraphy light with the thickness of the liquid tin target. We note that the central mass feature (see Refs. [39, 71]) appears to remain unvaporized. The halo-like, high transmissivity region observed around the center suggests that the connecting sheet part is particularly thin between the sheet and the central mass feature. Figure 2.2(b) displays a front-view shadowgraph, shown with artificially enhanced contrast, taken at $t_{VP} = 36$ ns. At this specific time point, the sheet exhibits significant transparency, illustrating the ongoing gradual reduction in thickness.

In Figure 2.2(c), we present averaged transmission values as a function of t_{VP} for various E_{VP}. These curves provide a quantitative representation of how transmission values evolve with t_{VP} across the dynamic range of our 12-bit acquisition. To obtain these values, we average transmission values between 100 and 155 µm radius on both sides of the vertically centered sheet lineout. This selected radial range deliberately excludes the center mass and rim features, focusing on regions of this target with approximately uniform thickness (cf. Ref. [71]). The shaded areas surrounding the plotted data points represent the uncertainty range (see discussion below).

We determine the target thickness using a method that utilizes its partial transparency to green backlighting. This approach follows the methods previously outlined by Vernay,[115] further developed for liquid tin targets by Liu *et al.*[71] We employ the `tmm`[116] Python package to establish a connection between optical target transmission and target thickness. This general transfer-matrix method optics package is used for calculating the reflection, transmission, and absorption of multilayer films. Our more versatile method here slightly deviates from the method outlined in,[71,117] but does not lead to significant numerical differences. We extract, pixel-wise, raw optical target transmission values, denoted P_{ij} with i and j representing pixel indices. Before linking the local transmission with thickness, we preprocess the shadowgraphs to account for backlight intensity fluctuations and 'dark' value. The parameter P_0 characterizes this overall dark value, including imaging glare sources such as PP plasma, VP

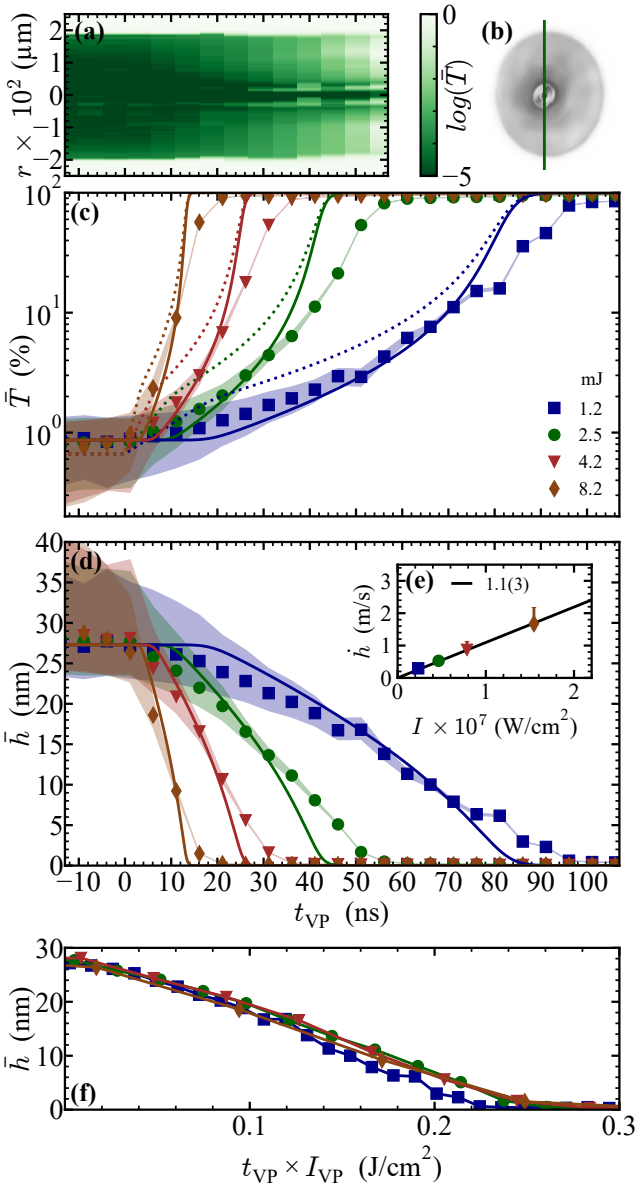

FIGURE 2.2: Caption on next page.

FIGURE 2.2 *(previous page)*: (a) 'Heatmap' of background light transmission constructed from vertical lineouts through the center of the liquid tin target B_{II} from front-view shadowgraphs, as a function of t_{VP} using $E_{VP} = 2.5$ mJ. (b) Front-view shadowgraph with digitally enhanced contrast at $t_{VP} = 36$ ns. (c) Average target transmission values $\bar{T}$ (on a logarithmic scale) during the vaporization of the target $B_{II}$for energies $E_{VP} = 1.2$ (blue data), 2.5 (green), 4.2 (red), and 8.2 mJ (brown). Shaded areas represent the uncertainty (see the main text). Bold and dashed lines show simulation results using the refractive index with the highest temperature in the literature available (1373.15 K[89]) and an extrapolated refractive index for the expected temperature for each energy case, respectively. (d) Average target thickness values $\bar{h}$ during the vaporization, obtained by applying the transmissivity method to the average transmission values shown in the upper graph. The bold lines show the simulation results. Inset (e) shows average vaporization rates $\dot{h}$ over VP intensity and the result of a linear fit to the data yielding a 1.1(3) proportionality factor. (f) Average target thickness values $\bar{h}$ as a function of deposited fluence.

scattering, target emission, SP, and electrical noise, all of which contribute to camera exposure. We employ the formula $T_{ij} = (P_{ij} - P_0)/(P_b - P_0)$, with P_b as the mean background value determined from the shadowgraph bin count. To determine P_0, we average the values of a 9x9 pixel area centered around the center of mass in front-view shadowgraphs, which corresponds to the thickest (and thus darkest) part of the sheet.[39] We separately obtain P_0 values for each VP energy, using frames where the SP arrives before the VP, thus enabling accounting for any potential scattering of the VP onto the imaging system. After establishing the relationship between T_{ij} and thickness h (using the `tmm` package), we correct for the 30° acquisition angle via $\bar{h} = \bar{h}_{30} \cdot \cos(30°)$. In Fig. 2.2(d), average sheet thickness values, obtained using the data from Figure 2.2(c), are presented. The curves demonstrate a continuous decrease in average sheet thickness with increasing t_{VP}. The shaded areas indicate uncertainty ranges resulting from error propagation, dominated by uncertainties in establishing the dark value at 0.046(5), which incorporates a ±10% uncertainty in its determination [this uncertainty also gives rise to the uncertainty region shown in Fig. 2.2(c)]. We note that the uncertainty, also in a relative sense, increases sharply with increasing thickness, limiting the application range of the current method to sheet thicknesses below approximately 25 nm. As a consequence, a different quantification method is required for studying thicker sheets. The gradual reduction in sheet thickness over time due to vaporization, as depicted in Figure 2.2(d), displays a nearly linear behavior. This motivates us to extract a (averaged) rate or, a recession *speed*, of vaporization. To calculate the vaporization rates, we determine the time required for the sheet to reduce from its original thickness to approximately 2 nm, using the data from Figure 2.2(d).

Figure 2.2(e) presents the resulting vaporization rates for the various VP intensities.

The data reveal a linear dependence of vaporization rate on VP intensity, in line with the claims of Liu *et al.*[38] By applying a linear fit to these vaporization rates for all intensities, we determine a proportionality factor $d\dot{h}/dI_{\mathrm{VP}}$ of 1.2(2) 10^{-7} $\mathrm{ms^{-1}/Wcm^{-2}}$, linking vaporization rate to VP intensity. This scaling factor enables us to predict average vaporization rates for a given VP intensity. The observed linear dependence of vaporization rate on VP intensity motivates plotting the sheet thickness as a function of deposited laser fluence $t_{\mathrm{VP}} \times I_{\mathrm{VP}}$, as shown in Figure 2.2(f). This approach results in the collapse of the full dataset, supporting the linear scaling of vaporization rate with intensity and indicating that the thinning is solely a function of the deposited laser pulse energy.

We next use an energy balance model to explain the apparent linear scaling of vaporization rate with VP intensity. The energy required to vaporize a unit volume of tin is $\rho H/M$ ($\mathrm{J/m^3}$), where ρ is the density, H is the latent heat and M is the molar mass. This energy will be supplied by the laser, which deposits per unit area a power aI ($\mathrm{J/m^2 s}$), where a is the absorptivity of the metal, and I is the intensity of the laser. Balancing these energy terms out gives a rate (m/s)

$$\dot{h} = \frac{aI}{\rho H/M} \tag{2.1}$$

Filling in typical values (see Appendix B for these values) and assuming 20 % absorptivity (typical for ~25 nm thick tin films according to multilayer optical calculations[116]) gives a predicted dependency of the thickness change rate due to vaporization $\dot{h}$ on intensity of 1.2 10^{-7} $\mathrm{ms^{-1}/Wcm^{-2}}$.

Inspired by the close match of the simple energy balance argument with the experimental observation, we create a numerical 1-D heat diffusion and vaporization solver to model and gain insight into the vaporization dynamics. The 1-D space is divided into individual cells with typical cell lengths of 100 pm. For each cell, the temperature is the key variable. Four steps are performed for each time step in the code.

(i) A surface recession speed (v, also one-sided vaporization rate) is calculated based on Hertz-Knudsen evaporation[98] for the front and back surfaces. For the pressure, the vapor pressure following the Antoine equation is used, resulting in

$$v = \frac{10^{A-[B/(T+C)]}}{\sqrt{2\pi MRT}} \frac{M}{\rho}, \tag{2.2}$$

where T is the surface temperature, M the molar mass, and R the gas constant. The parameters A, B, and C are 6.60, 16 867, and 15.47 respectively.[99,118] A cell

is considered vaporized when the surface recession (along the surface normal) has passed through the entire cell size. At that moment, it is removed from the simulation domain and no longer interacts with the remaining liquid via heat diffusion.

(ii) Recession of the surface causes a reduction in temperature in the cells where vaporization occurs, which are the first and last active cells. This is due to the latent heat required to transform the liquid atoms into gas, and thus to recess the surface. We can obtain a temperature reduction in the cell by balancing the energy input (heat capacity) and output (vaporization)

$$c_p \Delta x \Delta T = H v \Delta t \rightarrow \Delta T = \frac{H}{c_p \Delta x} v \Delta t, \tag{2.3}$$

where c_p is the molar heat capacity (with units [J/(mol K)]), Δx the cell size, and ΔT the temperature change, giving the input. The output is given by the latent heat H, and the size of the vaporized part, which is given by v, the recession speed, multiplied with Δt, the time step. This temperature reduction (and the recession) is calculated at every time step, not only when the entire cell is vaporized; this makes the temperature reduction and thickness reduction 'continuous' (with fs time steps) while the cell deactivation is discrete (a few hundred cells).

(iii) The first active cell is heated by the incident laser light. The absorptivity of the laser light is continuously updated based on the current remaining thickness of the tin. The absorptivity is calculated using the `tmm`[116] Python package. The refractive index used is the highest temperature data available for tin.[89] Thus, an energy balance for the laser heating, where absorbed energy is equated to a change in temperature, can be used to obtain a temperature change of the front cell

$$a I \Delta t = (c_p/M) \rho \Delta x \Delta T \rightarrow \Delta T = a \frac{I \Delta t}{(c_p/M) \rho \Delta x}. \tag{2.4}$$

(iv) The heat is diffused through the active cells. Fourier's law is discretized using a forward Euler method, resulting in

$$T_i^{t+1} = T_i^{t-1} + \frac{\alpha \Delta t}{\Delta x^2} \left(T_{i-1}^t - 2T_i^t + T_{i+1}^t \right), \tag{2.5}$$

where i indicates the different cells, and α is the thermal diffusivity. The pre-factor needs to satisfy $\alpha \Delta t / \Delta x^2 < 0.5$ to ensure stability of the forward Euler method and sets the maximum time step to typically 10 fs for our 100 pm discretization.

The sole inputs of the code are the starting thickness and the laser intensity, after which the model calculates the thickness and temperature of the 1-D tin slice over time

and saves this in output files. Appendix B includes some detail on the sensitivity of the model to the input parameters, and provides an overview of the input parameters used in the simulation. Within the model, the vaporization time t_{vap} is defined as the moment when only 2 nm of liquid tin is left, just as in the experiment. A $\dot{h}$ consistent with the experimental definitions can also be defined by dividing the initial thickness by the time period t_{vap}. To complete the comparison with the experimental observable, the transmission of the 1-D liquid slice is calculated using the same `tmm` package. We also account for the change in the refractive index of tin as it heats and the 30° observation angle of incidence when calculating the transmission via the 1-D model.

Fig. 2.3 shows detailed outputs from the code for the $E_{VP} = 2.5$ mJ case in Fig. 2.2. Initially, the tin is heated rapidly. As the temperature increases, so does the surface recession velocity, as it strongly depends on T. At a certain point, the energy loss to vaporization starts to dominate and even completely stops any heating, perfectly balancing out the input energy by the laser. The final temperature is around the temperature found (approximately 3000 K) in experimentally produced tin vapors,[76] underwriting the validity of our approach. We only show the temperature on the laser side since thermal diffusion keeps both sides of the 1-D domain at the same temperature within a few Kelvin. This equality aligns with expectation, given the typical thermal diffusion timescale that can be obtained from Fourier's law

$$\Delta t \approx \frac{h^2}{\alpha}, \tag{2.6}$$

where α is the thermal diffusivity. Taking a conservative value of $\alpha = 16.5\,\mathrm{mm^2/s}$ at a low temperature of 505 K[119] and a typical $h = 25$ nm results in a timescale of ~40 ps, much shorter than the relevant vaporization dynamics. We also note that the rapid heating induces a refractive index change and thus adds uncertainty to the transmissivity method because this heating cannot be experimentally observed.

The right axis of Fig. 2.3 also shows an energy balance of the calculations. The energy balance highlights the points mentioned above: an initial heating phase is present before the energy loss to vaporization balances out with the laser input, stabilizing the temperature of the liquid. The absorbed energy peaks when the 1-D slice is around 4 nm thick as the absorptivity increases as the sheet thins, increasing the temperature with it and thus speeding up the surface recession. The absorptivity of the liquid reduces strongly at even lower thicknesses, causing a rapid temperature drop at the end of the vaporization process.

The resulting thicknesses, as a function of t_{VP}, for the different cases are shown in Fig. 2.2(d). The simulated curves overall show good agreement with the experimental data given the absence of any free-fit parameters. We note that the experimental

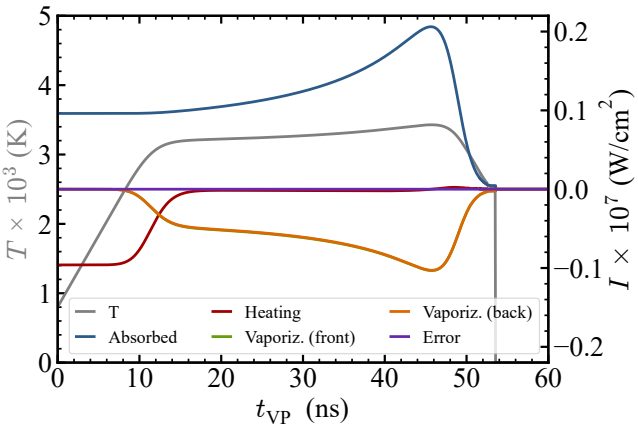

FIGURE 2.3: Example time-resolved output from the 1-D numerical code (aligning with the $E_{VP} = 2.5$ mJ case from Fig. 2.2). The left axis shows the temperature at the laser side over time. The right axis shows the code's internal energy balance, split in absorbed laser energy, heating of the liquid (which is an energy sink and thus negative, even though the temperature in the liquid goes up), vaporization on the front and back surfaces (which are indistinguishable), and an internal energy 'error,' being the difference between absorbed energy and the energy loss mechanisms.

data points appear to lack the clear plateau that is present in the simulations due to the heating phase. We hypothesize two reasons for this discrepancy. First, the initial temperature of the liquid in the simulation (set to 800 K based on radiation hydrodynamic simulations[120,121]) could be too low, increasing the heating period in the simulation. However, much higher values are not supported by the radiation hydrodynamic simulations. Second, the differences may be due to changes in the refractive index due to heating, causing the experimental method to misinterpret the measured transmissivity. The experimental method cannot distinguish the transmission changing through thinning or heating, and thus will interpret any refractive index change as a thickness change. To investigate the impact of heating on the transmissivity method more, we show two transmission curves (solid and dotted) in Fig. 2.2(c) that we obtain by applying the (inverse) transmissivity method to the thickness prediction curves from the 1-D heat simulation. These curves correspond to two refractive index cases, with the solid line corresponding to the highest temperature for which there is literature data available, $n_{1373.15K} = 3.93 + 7.87j$,[89] and the dotted line using a linear extrapolation of the literature data to the actual temperature (as predicted by the 1-D simulations). The results show that the observed transmission falls between the two lines, indicating that the lack of a plateau in the experiment may be due to the changing refractive index — although our linear extrapolation

most likely strongly exaggerates the change in refractive index. A second deviation between the simulation and experiment is the lack of increased vaporization rate at very low thicknesses in the experimental data. As mentioned, this accelerated vaporization is a simple consequence of the Fresnel equations, as discussed in detail in Ref. [122]. We speculate that the vapor surrounding the liquid (which absorbs a small amount of light and thus skews the transmissivity measured) obstructs the observation, or that the finite 5 ns length of the illuminating pulse blurs out the effect. Overall, besides these minor differences, we find excellent agreement between simulation and observational experimental data, indicating that the model reliably describes the vaporization process. Our experimental observations, combined with this agreement between simulation and experiment, validate the view of the vaporization process as a gradual process according to Hertz-Knudsen, rather than as violent explosive boiling.

Characterization of thicker targets A, B_I, and C using edge tracking

After gaining an understanding of the vaporization mechanism for the thinnest sheet in our studies (approximately 25 nm for B_{II}), we now extend our studies to much thicker targets, reaching up to approximately 200 nm in thickness. For these large thicknesses, the transmission method cannot be used to track the thinning over the full vaporization of the sheet. These thicker sheets are expected to exhibit a larger spatial thickness gradient (see Appendix A, Fig. 2.7). The presence of such a steep thickness gradient enables us to define and track the edge of the vaporizing sheet, which effectively represents a nearly discrete transition between the fully vaporized and remaining liquid regions. The two regions are characterized by very different contrast levels. This contrast difference is due to the green backlight being able to penetrate through the tin vapor while being extinguished by the remaining liquid sheet part. We refer to the method of tracking the discrete transition as 'edge tracking'. We explain the method in detail in Appendix C. This method relies on PD data of the VP exiting the vacuum chamber.

Fig. 2.4(a) displays shadowgraphs of the liquid tin target B_I, A, and C before VP irradiation in front and side view, allowing a qualitative comparison of the target morphology. Fig. 2.4(b) shows front-view shadowgraphs of the target A for three times t_{VP} for an $E_{VP} = 8.4$ mJ, clearly showcasing the recession of the inner sheet due to vaporization. We observe that the outer and thinner sections of the sheet become transparent earlier than the inner and thicker regions, leaving behind an identifiable inner remaining sheet. This inner radius $R_{inner}(t_{VP})$ is tracked, following the edge-tracking method introduced above. At $t_{VP} = 60$ ns, Fig. 2.4(b) shows that the rim, ligaments, fragments, and center mass do not fully vaporize. This can be understood

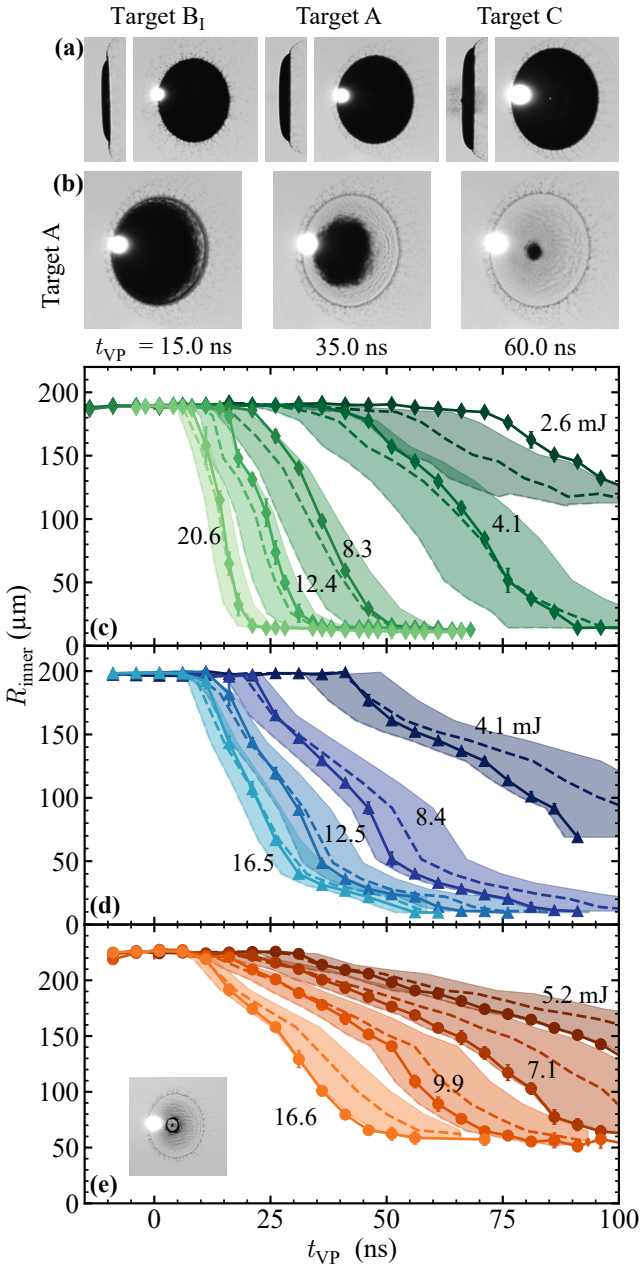

FIGURE 2.4: (a) Side- and front-view shadowgraphs of target B_I, A, and C before VP irradiation. The bright spots are due to the plasma emission caused by the PP. (b) Front-view shadowgraphs of target A visualizing the vaporization process at times t_{VP} for $E_{VP} = 8.4$ mJ. (c,d, and e) Inner sheet radii during vaporization for targets B_I, A, and C, respectively. The inset numbers indicate the used VP energy and the dashed lines are corresponding simulation results (see the main text).

from their considerably larger, micrometer-scale thickness.[39] Vaporization of these thick features is only observed when there is a significant increase in VP energy.

Figs. 2.4(c, d, and e) show the edge-tracking results for the inner sheet radii results for targets B_I, A, and C, respectively. Fig. 2.4(c), shows that the inner sheet radii decrease as t_{VP} increases and that this reduction is sped up at higher VP energies. This observation aligns with our observations shown in Fig. 2.2 for a much thinner target. The reduction of the inner sheet of the target B_I [Fig. 2.4(c)] with time highlights certain differences in target morphology when compared to A and C [Fig. 2.4(d,e)]. In the case of target A [Fig. 2.4(d)], we observe that the rate of reduction of R_{inner} slows down significantly for radii below 50 µm. This suggests the presence of a thicker center region. The edge-tracking analysis of target C [Fig. 2.4(e)] reveals even more pronounced differences around the center, with its inner radii converging to approximately 50 µm after which the vaporization process seems to end. As shown in the shadowgraph inset, the converging radius is not due to a thicker center region but, rather, a thick rim surrounding a center mass. See Appendix A, Fig. 2.8 for further detailed shadowgraphs showing this specific feature. The occurrence of such peculiar center mass features is yet not fully understood. In previous work, such features were hypothesized to be attributable to compressible flow effects, specifically to a collapsed cavity generated by the PP.[39] In the current study, we focus on the sheet vaporization dynamics away from any such compressible flow artifacts.

To relate the inner sheet radii to a local thickness, with the final goal of studying the local vaporization rates, we next employ the semi-empirical thickness model introduced by Liu *et al.*[71] for laser-shaped tin targets such as ours. This model is based on a self-similar solution derived from the model by Wang *et al.*[123] It assumes an inviscid radially outward flow in the expanding sheet, neglecting curvature-induced radial pressure gradients and sheet features such as the center mass. A solution to the non-dimensionalized equation governing the sheet expansion can be found in the form[123]

$$h^* t^{*2} = f(\frac{r^*}{t^*}), \tag{2.7}$$

with the self-similar variables denoted as $r^* = r/D_0$, $t^* = \dot{R}_0 t/D_0$, and $h^* = h/D_0$. Any actual (dimensional) thickness profiles $h(r, t, \dot{R}_0, D_0)$ can be collapsed onto a single self-similar curve $y = f(x)$. Conversely, given any set of experimental inputs (such as droplet radius, time after impact, etc.), the local thickness can be obtained if $f(x)$ is known. Precisely this function was previously obtained by Liu *et al.*[71] as

$$f(x) = \frac{1}{a_0 + a_1 x + a_2 x^2}, \tag{2.8}$$

with $a_0 = 1.65(2)$, $a_1 = 6.9(3)$, and $a_2 = -2.4(8)$ as parameters that were determined by fitting the proposed $f(x)$ to the available experimental data,[71] thus yielding a semi-empirical thickness model

$$h(r, t, \dot{R}_0, D_0) = \frac{D_0^3}{a_0 \dot{R}_0^2 t^2 + a_1 \dot{R}_0 t r + a_2 r^2}. \tag{2.9}$$

Here, $\dot{R}_0$ is input from the measured initial droplet expansion speed (following Ref. [38] in contrast with the choice of using propulsion U of the original Ref. [71]), D_0 is the initial droplet diameter, and t, r represent time and radial coordinates, respectively. This semi-empirical model allows us to effectively characterize the used targets (see Fig. 2.7 in the Appendix).

Before using this model, we note that target C exhibits a prominent and peculiar inner center rim surrounding the center mass. This feature along with a center mass is not predicted by the model. Consequently, we may expect that the mass that is assumed to be available to produce the sheet is overestimated. We first seek to correct target C for the additional mass loss channels. According to findings from Ref. [39], between 5 and 20 % of the mass is concentrated in a center mass remnant, with no obvious predictive scaling available. Given that we observe both a prominent center mass and an additional ring-like feature, we conservatively take the upper limit (20 %) as an estimate for the mass lost to such compressible flow features. Furthermore, given the large PP energy, we also should correct for the amount of mass that is lost through the ablation process that sets in motion the dynamics. From prior simulations in Ref. [39], and the heuristic scaling law provided therein, we may estimate such ablation losses to account for an additional 20 % mass loss. Thus, in the following, we take target C to have approximately 40 % less mass available on the sheet as would be expected from the initial large droplet size (cf. Fig. 2.7 in the Appendix).

Next, we return to the vaporization model of the previous section. The model requires as input h, here obtained from the semi-empirical thickness model, which enables converting the measured R_{inner} (cf. Fig. 2.4) to a local thickness h. Taking this local thickness h for each R_{inner} as input, the simulation results in a t_{vap}, which is plotted in Figs. 2.4(c-e) as the dotted curves. The colored bands depict uncertainty estimates based on a 15% uncertainty on the actual thickness. Overall, good agreement is found between simulations and experimental data, well within the uncertainty estimates. The agreement is most striking for target B_I aside from the lowest energy case (2.6 mJ). This minor discrepancy may in part be attributed to uncertainty in the energy calibration. Target A also shows good agreement but a systematic offset towards later t_{VP} can be tentatively identified. Such an offset may be attributed to the fact that mass is also lost on target A, given that ablation and compressible flow also

feature here if less strongly than for target C. Target C shows the same systematic offset towards later t_{VP} which may indicate that the applied compressible flow (or ablation) correction still underestimates the true value. Still, there is full agreement between simulation and experimental data within the stated uncertainty estimates over both approximately an order of magnitude in thickness and vaporization laser intensity.

To enable the accurate prediction of vaporization dynamics given a certain laser intensity, we next turn to averaged vaporization rates — reducing the data in Fig. 2.4 effectively to a single key parameter, $\dot{h}$. This parameter is obtained by minimizing the difference between (h, r) and $(\dot{h}t_{\mathrm{VP}}, r)$ curves with $\dot{h}$ a free fit factor, a method that is inspired by the approach of Liu *et al.*[38] We perform the fit in the region of the sheet, well away from the rim and center mass features. The (h, r) values are obtained from Eq. (2.9) at R_{inner} at $t = \Delta t$ [cf. Table 2.1].

Fig. 2.5 depicts a linear correlation between the thus obtained vaporization rates ($\dot{h}$) and VP intensity for all targets within the investigated vaporization laser intensity range of approximately 1–5 $\times\, 10^7$ W/cm^2.

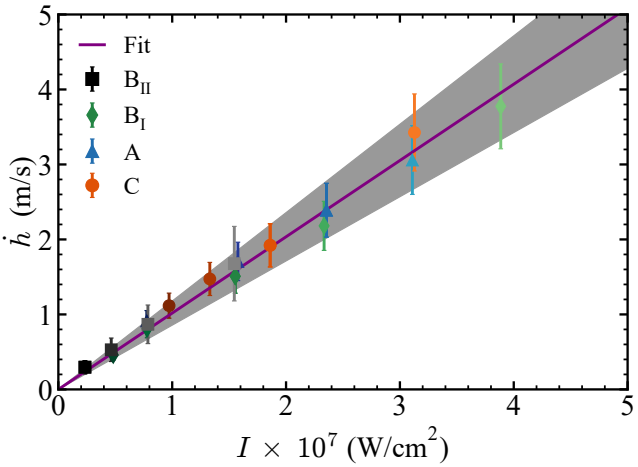

FIGURE 2.5: Average vaporization rates of the targets $\mathrm{B_{II}}$, $\mathrm{B_I}$, A, and C as a function of VP intensity. The purple line shows the result of a linear fit to the concatenated data. The shaded area indicates the fit uncertainty.

The rate values for target $\mathrm{B_{II}}$ are directly taken from Fig. 2.2(e). For all other targets ($\mathrm{B_I}$, A, C), the vaporization rates ($\dot{h}$) are the result of the comparison between t_{VP} and the thickness prediction obtained from the semi-empirical thickness model as explained above (cf. Fig. 2.7). For target $\mathrm{B_{II}}$, the uncertainty arising from the initial

target thickness was taken into consideration with ± 15 % (from the dark value correction), and for all other targets (B_I, A, C), a standard deviation of ± 15 % was assumed as an uncertainty measure (dominated by the uncertainty in available mass). The observed increase in uncertainty with the VP intensity (cf. Fig. 2.5) is a direct result of the constant delay step size when scanning the SP over the VP, for all measurements, leading to fewer steps during the VP for higher intensities. Finally, we perform a linear fit to the merged dataset of average vaporization rates and obtain a $d\dot{h}/dI_{VP}$ of 1.0(3) 10^{-7} ms^{-1}/Wcm^{-2}, in agreement with and extending the linear scaling of the previous section over an order of magnitude in both thickness and laser intensity. The vaporization rate is thus observed to linearly scale with intensity, *independently* from both initial and instantaneous thickness; the time t_{vap} required to vaporize a sheet of thickness h will scale as $t_{vap} \propto hI_{VP}^{-1}$ with the $\dot{h}$ at every instant scaling as $\dot{h} \propto I_{VP}$.

We note that a previous study[38] reported a vaporization rate of 4.4 m/s for a ~0.7 J/cm^2 fluence laser pulse, 50 ns in duration (yielding an intensity of approximately 1.4 × 10^7 W/cm^2) which is a faster rate than would be expected from our observations. However, the authors of Ref. [38] acknowledge an error in a double correction of the vacuum window transmissivity (upscaling the input I_{VP}). Additionally, we have improved on the edge tracking method by benchmarking it to the photodiode data, which also causes a slightly different result. Accounting for both differences brings the previous data again in agreement (at ~3 m/s at 2.2 × 10^7 W/cm^2) with the present more accurate observations.

Self-similarities and generalization

We next revisit all experimental data and further study two key findings of this work, namely that $t_{\mathrm{vap}} \propto h I_{\mathrm{VP}}^{-1}$ and $\dot{h} \propto I_{\mathrm{VP}}$ which can be transformed into each other $\dot{h} \propto h/t_{\mathrm{vap}} \propto I_{\mathrm{VP}}$. Fig. 2.6(a) shows the result of multiplying the t_{VP} time axis by the VP intensity I_{VP} to arrive at a local fluence $t_{\mathrm{VP}} \times I_{\mathrm{VP}}$ previously presented only as an Ansatz in Ref. [38]. It demonstrates that the vaporization of liquid tin targets in the investigated laser intensity range 0.4–4 $\times 10^7$ W/cm^2 is solely a function of the deposited fluence, across all individual targets. This underpins the first key finding that $t_{\mathrm{vap}} \propto I_{\mathrm{VP}}^{-1}$.

Fig. 2.6(b) presents all experimental data (including that of target $\mathrm{B_{II}}$ obtained using the transmission method) in non-dimensional units ($h^* t^{*2}, r^*/t^*$), with $h = t_{\mathrm{VP}} \cdot I_{\mathrm{VP}} \cdot d\dot{h}/dI_{\mathrm{VP}}$ taking $d\dot{h}/dI_{\mathrm{VP}}$ =1.0(3) 10^{-7} ms^{-1}/Wcm^{-2}. All data is found to collapse on a single curve, which underlines the validity of our approach in invoking the self-similar model and in the mutual agreement of the (transmission vs. edge tracking) methods employed. We may further compare our findings directly with Eq. (2.9), depicted as a black solid line in the same figure. The edge tracking curves show reasonable agreement with the self-similar solution that represents a thickness profile, indicating that the edge tracking data is a good measure to quantify the vaporization process. The collapsed data tend to lie slightly above the self-similar curve, at early times, which may indicate an overall overestimation of the mass available for the sheet (see discussion above). Alternatively, it may point towards a small overestimation of the overall vaporization rate, well within the error bars of Fig. 2.5. More noticeable deviations occur at the smallest r^*/t^* values, where the experimental data seems to vertically diverge. These deviations are due to the center mass features. Also at the largest r^*/t^* values deviations appear to occur but here we note that the self-similar model contains no edge and does not end where the sheet does. Further deviation at the larger r^*/t^* values may be attributed to finite curvature of the targets, the investigation whereof is left for future work.

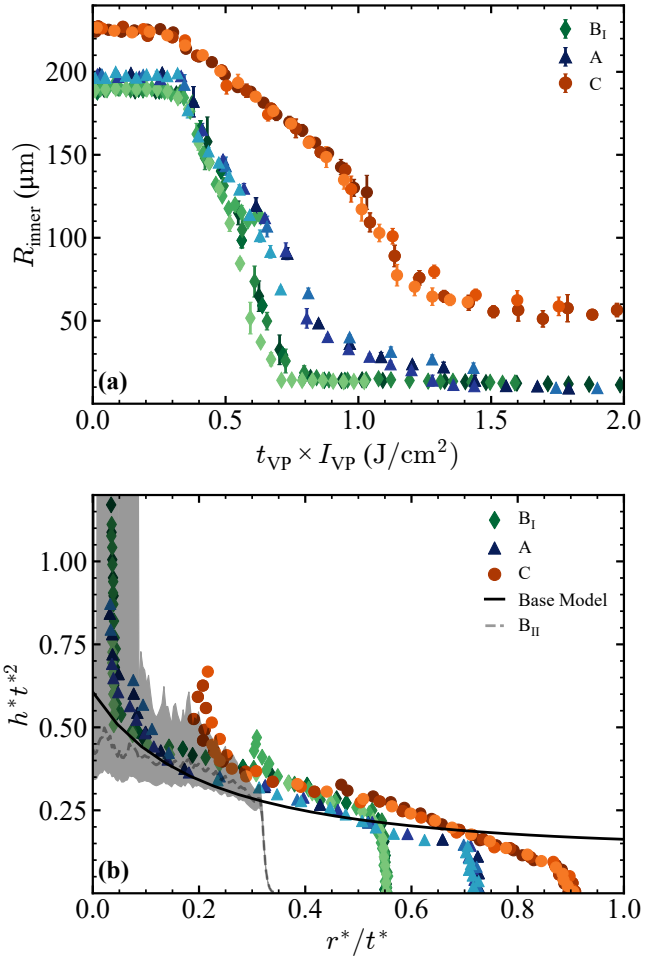

FIGURE 2.6: (a) 'Collapse' of the edge-tracking data for $R_{\text{inner}}$for targets B_I, A, and C [cf. Fig.2.4(c-e)] when plotted as a function of fluence $t_{VP} \times I_{VP}$. (b) Global collapse of the edge-tracking data (targets B_I, A, and C) and B_{II}data (gray data; includes an uncertainty band) in dimensionless units (see the main text). The solid black line indicates the semi-empirical thickness model of Ref. [71].

Conclusions

We examine how a liquid tin target vaporizes when exposed to a 100 ns laser pulse (box-shaped in space and time). Our observations are based on stroboscopic acquisitions using an illumination pulse enabling 5 ns time resolution and 5 µm spatial resolution while scanning systematically throughout the 100 ns laser pulse. For thin (∼25 nm) and flat sheets, the absolute thickness can be obtained from the finite transmission of the backlighting through the sheet, following Liu *et al.*[71] Our findings reveal gradual vaporization characteristics and a linear relationship between the average vaporization rate with the laser pulse intensity, i.e. $\dot{h} \propto I_{\mathrm{VP}}$. Inspired by the fact that the observed scaling relation may be explained from simple energy balance, we construct a numerical 1-D heat and vaporization solver based on the Hertz-Knudsen equation and find excellent agreement between simulations and experimental data. A gradual vaporization mechanism would signal that nanoparticles, as observed in similarly prepared tin vapor targets,[76] originate from post-vaporization clustering of atomic species. We next extend our investigations to thicker (up to approximately ∼200 nm) targets, improving on an edge-tracking method previously established by Liu *et al.*[38] in tandem with a semi-empirical sheet thickness model[71] to further quantify the vaporization dynamics. Also here the 1-D simulations are in excellent agreement with the experimental data after accounting for additional mass-loss channels. By combining the vaporization rate data from all experiments, we confirm the linearity $\dot{h} \propto I_{\mathrm{VP}}$ with a prefactor of 1.0(3) 10^{-7} $\mathrm{ms^{-1}/Wcm^{-2}}$ over the full investigated intensity range (0.2–4 $\times 10^7$ $\mathrm{W/cm^2}$). We furthermore demonstrate that the amount of vaporization of liquid tin targets in the investigated laser intensity range is governed solely by the deposited fluence, across all individual targets and that the time required for vaporization follows $t_{\mathrm{vap}} \propto h I_{\mathrm{VP}}^{-1}$, validating the Ansatz proposed in Liu *et al.*[38] Lastly, we collapse all suitably non-dimensionalized data onto the self-similar solution proposed in Ref. [71].

We thus identify the mechanism of laser-induced vaporization (as a gradual vaporization governed by the Hertz-Knudsen equation) at low intensities as may be found in future advanced target preparation schemes for more efficient generation of extreme ultraviolet light. Furthermore, we provide an accurate prediction of the vaporization rates as a function of laser intensity over an order of magnitude around 10^7 $\mathrm{W/cm^2}$, which is shown to hold for all target thicknesses in a range of approximately 20–200 nm. Our work may guide and find application in the development of future EUV sources.

Acknowledgments

This work has been carried out at the Advanced Research Center for Nanolithography (ARCNL). ARCNL is a public-private partnership with founding partners UvA, VU, NWO-I, and ASML, and associate partner RUG. This research was funded by the European Research Council (ERC StG 802648).
The authors thank Diko Hemminga for valuable insights into the droplet temperature after pre-pulse impact, and John Sheil, Michael Purvis, and Haining Wang for valuable discussions. We would also like to thank Henk-Jan Boluijt and Laurens van Buuren for their work on the experimental setup.

Appendices

A Expected target thickness profiles

Fig. 2.7 depicts thickness profiles of the various tin sheet targets used in the paper, as obtained from the semi-empirical thickness model Eq. (2.9) with the required input taken from Table 2.1 in the main text. The dashed line for target C thus shows a mass correction of the target by 40 % (see the main text).

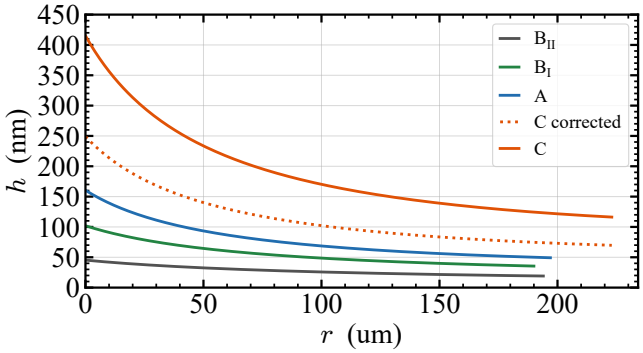

FIGURE 2.7: Thickness profiles according to semi-empirical thickness model Eq. (2.9) for the used targets, with input from Tab. 2.1 in the main text.

Fig. 2.8 displays target C at various stages of vaporization, highlighting an additional feature around its center mass. It shows that this feature is significantly thicker than the sheet and even the rim and center mass given that it is not vaporized even after the 100 ns-long VP. For more information about the center mass feature in general see Ref. [39].

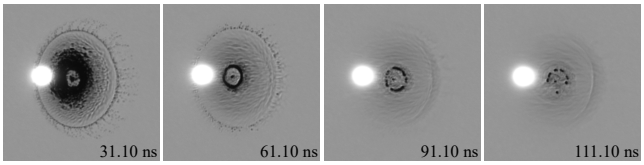

FIGURE 2.8: Shadowgraphs of target C showcasing the observed feature (see the main text) around its center mass at different stages of vaporization.

B Input parameters in 1-D numerical code

Table 2.2 shows the used input parameters for the 1-D numerical simulation. The initial liquid temperature of 800 K is estimated from the temperature after the end of the laser pulse in RALEF-2D radiation hydrodynamic simulations such as performed by Poirier *et al.*[121] A sensitivity study of the model predictions is performed for all input parameters. It is found that t_{vap} is most strongly influenced by the latent heat, which also follows directly out of the energy balance (see the main text). However, the uncertainty on the latent heat is below 0.1 % according to literature, so this has a negligible effect on the simulation.[124]

Parameter	Value	Source
Refractive index	$3.93 + 7.87j$	Highest T value of[89]
Conductivity (κ)	43.6 W/(m K)	Highest T value of[125]
Initial T	800 K	RALEF simulations
Density	6787 kg/m^3	Density at 800 K[126]
Molar mass	0.118 71 kg/mol	[118]
Molar heat capacity (c_p)	27.2 J/(mol K)	Value at highest T available[127,128]
Latent heat	301×10^3 J/mol	[124]
Diffusivity (α)	28.0 mm^2/s	Calculated from $\frac{\kappa}{\rho(c_p/M)}$

TABLE 2.2: Table of input parameters used in the 1-D numerical simulation.

The next strongest sensitivity of t_{vap} is density, and thus also initial temperature, which influences the density. Again, this can be seen in the energy balance in the main text. The uncertainty on ρ itself is only ~1 % according to a review of thirteen papers.[126] Thus, the initial temperature, and its indirect effect on ρ gives the largest uncertainty on t_{vap}. We estimate the uncertainty in the initial temperature to be approximately ~100 K due to uncertainties in the influence of the pre-pulse, translating to a 3 % effect on the predicted t_{vap}. This uncertainty is significantly smaller than the uncertainty originating from the thickness estimation. Thus, the model

predicted t_{vap} may considered to be rather insensitive to the input parameters. The temperature during the vaporization predicted by the model is even less sensitive to changes in the input parameters. This originates from the exponential dependence on the temperature for the vapor pressure (nominator in Eq. 2.2), meaning that only small changes in temperature are required to respond to changes in the input parameters such as ρ or latent heat. Thus, the change in temperature stays below 1 %, even for conservatively large (10 %) changes in used input parameters.

C Edge Tracking Method

The edge tracking method relies on PD data of the VP exiting the vacuum chamber. Here, we assume that the geometrical obstruction created by the target, as identified via the 560 nm shadowgraphy, applies directly also to the 1064 nm VP laser light. Separately, we note that neither VP nor SP laser light is absorbed by the vapor (also see Ref. [76]). We establish a correlation between the VP laser light transmitted along the sheet (S, as measured by a PD after the chamber) and our observations of inner sheet radius (R_{inner}), which we extract from the shadowgraphs. This correlation is based on the Ansatz that the VP is spatially blocked by the remaining liquid and that the increase of the PD signal S is directly proportional to the decrease in sheet area

$$(1 - S(t_{\mathrm{VP}})) \propto (R_{\mathrm{inner}}(t_{\mathrm{VP}}))^2. \tag{2.10}$$

Note that both quantities (S and R_{inner}) are normalized. Next, to define a sheet edge, a suitable threshold (T) needs to be defined. For this purpose, we perform a Gaussian fit to the background distribution counts, individually for all shadowgraphs, which allows us to determine its mean value (P_{val}) and width (P_{width}). We determine the benchmarked threshold using the relation $T = P_{\mathrm{val}} - B_{\mathrm{level}} \cdot P_{\mathrm{width}}$ where we subtract a value $B_{\mathrm{level}} \cdot P_{\mathrm{width}}$ from P_{val} that is proportional to the background distribution width with prefactor (B_{level}). This approach enables us to effectively deal with intensity-induced speckle broadening in the illumination. Subsequently, we iteratively adjust the parameter B_{level} and, consequently, the threshold T. With each adjustment, we obtain a threshold-specific inner sheet $R_{\mathrm{inner}}(t_{\mathrm{VP}})$. The optimal value for B_{level} is then found by minimizing the differences between the left- and right-hand side of Eq. (2.10). In summary, we obtain a threshold such that the obtained R_{inner} best matches the transmitted VP signal.

Chapter 3

Spectroscopic Imaging of Tin Vapor Near Plasma Threshold

Dion Engels, Karl Schubert, Mikheil Kharbedia, Wim Ubachs, and Oscar Versolato.
Physical Review Research **7**(2), 23307 (2025).

We report on the spectroscopic imaging of tin vapors laser-generated from thin liquid tin targets using laser intensities around the threshold of plasma formation. Specifically, we study tin vapor using an extinction imaging method in the UV regime (230–400 nm) to obtain 40-µm-spatial-resolution images with 10-cm^{-1}-resolution spectra 100 ns after vaporization. The vapor is created by irradiating a non-oxidized free-flying thin film with a nanosecond laser pulse, the intensity of which is varied between 1–130 $\times$ 10^7 W/cm^2, from below to above the threshold of producing plasma. Vapors created with laser intensities below 40 $\times$ 10^7 W/cm^2 exhibit a spatially homogeneous neutral atomic component, with a temperature around 3000 K, as well as a broadband component due to nanoparticles. The morphology and composition of the vapor change as the plasma forms during vaporization at higher intensities, with the temperature of the vapor rising to 8000 K at the highest intensity. At these intensities, the broadband component disappears, indicating that it is a vapor composed only of free atoms.

Introduction

Vapors near plasma formation threshold find applications in high-tech fabrication technologies as well as in next-generation fusion power generation concepts. In pulsed laser deposition (PLD),[129] as an example of physical vapor deposition (PVD) techniques,[130] a $\sim 10^9$ W/cm^2 laser pulse ablates a target, creating a plasma vapor plume, to deposit thin layers for the fabrication of high-performance multi-element coatings. Plasma-assisted atomic layer deposition (ALD) enables the synthesis of ultra-thin films with atomic resolution.[131] In liquid metal divertor (LMD) technology for nuclear fusion, specifically in 'vapor box' concepts, vapor is used to reduce and radiate away[132,133] the heat load on the wall of fusion devices.[65–67] Vapor is also of interest for extreme ultraviolet (EUV) lithography, which uses hot-and-dense tin plasma to produce EUV light.[64] To generate the required light, liquid tin droplets are first pre-shaped into thin films before being irradiated by the EUV-producing 'main pulse'[35,40,134] (for alternative approaches see, e.g., Refs. [109, 135–139]). Pre-plasma formation[68,69,139] and 'advanced target shaping' concepts[34] are proposed to extend current pre-shaping techniques for improved operation efficiency. All such applications benefit from having diagnostics to obtain vapor characteristics and to provide feedback for control loops.

Inspired by these applications, in particular those related to EUV generation, we apply a spectroscopic absorption imaging method following Engels *et al.*[76] to diagnose tin vapor created by irradiating a thin film with a nanosecond laser pulse over a range of intensities spanning $1–130 \times 10^7$ W/cm^2 around the threshold to produce plasma. Prior work[76] provided a view of the local temperature, composition (i.e. atoms vs nanoparticles), and local densities of such tin vapor at an intermediate laser intensity ($\sim 10^8$ W/cm^2) where no plasma was generated. The current range of laser pulse intensities allows us to witness and study in detail the changes in target morphology and composition with laser intensity, ranging from below to above the threshold of producing plasma from the liquid target, and to demonstrate the applicability of the spectroscopic imaging method also in the regime of plasma generation in tin vapor.

Methods

In the experiment (see Fig. 3.1), a non-oxidized free-flying liquid tin sheet is created in a vacuum by expanding a molten microdroplet using a nanosecond laser pulse. The sheet (the 'target') has a diameter of approximately 500 µm with a thickness of 25–10 nm (decreasing radially outward[71]). This target serves the purpose of providing an isolated thin layer of metal and is kept constant throughout the current study (for details on the dynamics of target preparation see Ref. [39] and references therein). To

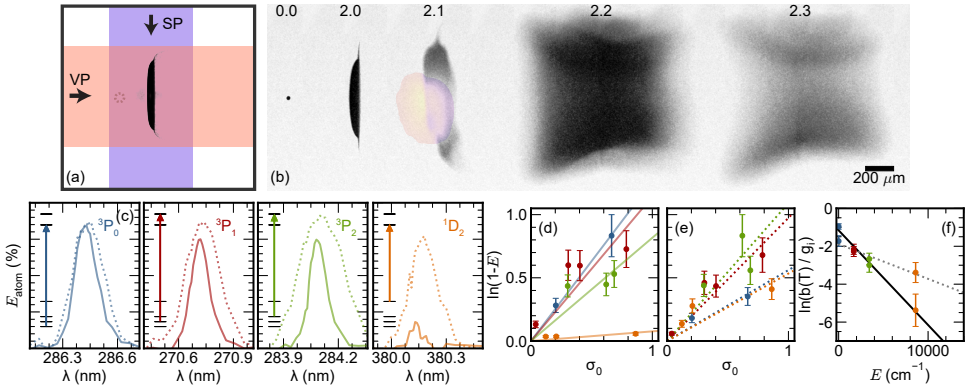

FIGURE 3.1: Setup and methods. (a) The direction of the vaporization pulse (VP, orange) and the perpendicular shadowgraphy pulse (SP, purple) that follows 100 ns later from a top view perspective. (b) Processed side-view shadowgrams created with 284.08 nm-backlighting at different times in the droplet to sheet to vapor process. The VP (here at its highest intensity) arrives 2.1 µs after the droplet is expanded into a sheet. The light produced from plasma generated during the vaporization is highlighted in false color. (c) Extinction (scattering + absorption) around several atomic resonances when the broadband term is subtracted (E_{atom}). The plot colors are related to the ground levels of the resonances (also indicated on the top right). The transition is also shown in a schematic level diagram of ground state tin ($5s^25p^2$) on the left of each resonance. The solid line is the 5×10^7 W/cm^2 case, while the dotted line is the 130×10^7 W/cm^2 case. Note the strongly increased absorption for the highest ground state. (d) σ_0 vs ln(1-E) integrated over the resonance, for the low-intensity case. See the main text for information. Panel (e) shows the high-intensity case. (f) Boltzmann plot for the two intensities (dotted is the high intensity).

vaporize the target, we employ a vaporization pulse (VP, 6 ns, $\lambda = 1064$ nm) focused to a circular spot with a diameter of ∼1.5 mm at the target location (the laser intensity is nearly constant over the sheet, decreasing only ∼5 % from the center to the edge). To create different vapors, the intensity of the vaporization pulse is varied over a range 1–130×10^7 W/cm^2, keeping all other things constant.

We image the vapor with a UV 'shadowgraphy' pulse (SP) at a 90° angle to the VP. The UV pulse has a length of 4 ns, a spectral bandwidth of 5–10 cm^{-1}, and a tunable wavelength between 230–400 nm for spectroscopy. Figure 3.1(b) shows the evolution of the droplet into a thin film target and, subsequently, into a vapor.

We capture 25 frames at each UV wavelength with a fixed 100 ns delay between the VP and the SP (each frame is a new laser-droplet event). The 100 ns delay between VP and SP is chosen such that the camera exposure start can be placed in between, avoiding plasma emission in the images (which would interfere with the absorption

measurements) without the vapor thinning too much and reducing signal-to-noise. Varying the VP and SP delay would provide further insights on the dynamics of the expanding vapor, such as composition or density changes. Here, we focus on the impact of a single parameter, the VP intensity, with a study of the vapor dynamics left for future work. The ten best-aligned, most up-down-symmetric frames are selected from the 25 frames. Next, they are geometrically overlapped, averaged, and corrected for differences in magnification (which changes with wavelength due to chromatic aberrations of the single-lens imaging setup). Finally, all CCD pixels are binned into 16 by 16 bins (called a pixel hereafter) to prevent the impact of any misalignment, resulting in images without visible 'speckle' and improved signal-to-noise, with an effective resolution of 40 µm.

We determine the vapor temperature, per pixel, via strong Sn-I resonances originating from four electronic levels [see Table 3.1 in the Appendix and cf. Fig. 3.1(c)]. Figure 3.1(c) shows extinction (scattering + absorption) profiles (for two separate VP intensity cases, dotted and solid lines, respectively) for each of four selected atomic resonances, one from each of the four lowest-lying electronic levels. The broadband contribution is removed from the extinction, yielding E_{atom}. For three of the transitions [cf. Fig. 3.1(c)], we note a significantly increased absorption for the high-intensity case compared to the low-intensity case, with the difference increasing with the energy of the bottom level. This behavior is indicative of a significant temperature change. To further quantify the temperature and any changes therein, we employ a Boltzmann plotting technique (see, e.g., Ref. [140] for reference) closely following the approach of our previous work.[76] We plot the integral over the wavenumber (ν) of the logarithm under the atomic resonances $\ln(1 - E_{\mathrm{atom}})$ versus the transition's resonance cross section σ_0. This enables extracting the occupation of each level from the Boltzmann factor $b(T)$

$$\int -\ln(1 - E_{\mathrm{atom}}(\nu))d\nu \propto b(T)nL\sigma_0, \tag{3.1}$$

where n is the density of the vapor and $b(T)n$ is the density of the absorbing state; L is the path length through the vapor, which with n defines the column density nL. The strength of the resonance is determined by the resonance cross section σ_0. Thus, for a single pixel, we can extract the occupation $b(T)$ from slopes in Fig. 3.1(d-e). Finally, by fitting a straight line through the occupation versus the energy of the level, a temperature T is extracted [see Fig. 3.1(f)].

Results

Spectroscopy

Figure 3.2 shows all the created vapors, with VP intensities ranging between 1–130×10^7 W/cm^2, increasing from left to right. The top row shows shadowgrams at 254.73 nm (at the center of the atomic resonance, cf. Table 3.1), and visualizes how the shape of the vapor changes when changing VP intensity. At low intensity [panels (a,f)] the vapor has a cone shape.[76] For somewhat higher intensities [panels (k,p)], the rim starts vaporizing and contributes to the absorption, as highlighted by the gray cloud near the edges of the shadowgram. At these VP intensities, plasma light emission is particularly noticeable near the center (intentionally filtered out by the camera exposure and hence not visible in the shadowgrams). Finally, in panel (u), plasma forms nearly everywhere on the sheet, creating an additional pressure field that changes the shape of the vapor.

The target has three distinct morphological characteristics following the work of Liu *et al.*[39] One feature is the 'center dot,' which usually holds about 10 % of the initial droplet mass,[39] which would make it ∼2 µm thick. The second is the 'rim,' which bounds the sheet.[39] The thickness of the rim can be predicted from hydrodynamic arguments to be approximately ∼1 µm in diameter.[71] The thinnest part is the sheet, which averages a thickness of around ∼20 nm. Our observations indicate that plasma first forms on the thickness extrema.

In the experiment, visible light emission is determined to be an indicator of plasma formation (previous experiments have correlated light emission with detected ion current[121]). The first emission of visible light is observed in the 25×10^7 W/cm^2 case, (the third column Fig. 3.2), on the center dot, the thickest part of the target.[39] At 40×10^7 W/cm^2, the fourth column in Fig. 3.2, plasma also forms on the rim. Only at the final intensity does plasma form on the entire thin film. A detailed study of the plasma formation process itself lies beyond the scope of the present study; in the current work, we focus on the impact of the plasma on the characteristics of the generated vapor.

The second row of Fig. 3.2 shows the extinction spectrum, expressed as $-\ln(1-E)$ in order to have a value linear with column density nL. The four spectra in each panel correspond to the four pixels shown in the first row. The different pixel locations exhibit nearly identical spectra except for a difference in overall amplitude which reflects different column densities. Panel (g) shows spectra taken at a VP intensity similar to that of Ref. [76] which indeed are nearly identical [we plot averaged data from Ref. [76] in panel (h)], highlighting the reproducibility of the vapor composition for similar intensities and target shapes (the current target, however, is approximately

2x thinner). The neighboring panels (b,l) show very similar spectra with only an overall change in absorption, even though the VP intensity has changed 25x. Further increasing the VP intensity leads to clear changes in the spectra, with panels (q,v) depicting a decrease and, finally, the disappearance of the 'broadband' component previously hypothesized[76] to be caused by Mie scattering by nanoparticles.

To more clearly show the change in the broadband component, we invert Beer-Lambert's law to an equation for the cross section

$$\sigma(\nu) = -\frac{\ln(1 - E(\nu))}{nL}. \tag{3.2}$$

The absolute column density nL cannot be directly determined from the experiments without a detailed model for the cross section σ which necessarily would need to include physical effects such as power, collisional, and Stark broadening. Following Ref. [76], we instead introduce a dimensionless parameter a to describe a 'relative density,' enabling the comparison of densities within a vapor and also between the various vapors in the experiment. We note that this 'relative density' is a measure of nL and, thus, is a relative *column* density as it includes the path length L.

We obtain the values for a via two complementary methods. The first method is to compare the extinction of the broadband component, resulting in a value for a defined by the Mie scattering component from fitting the spectrum over every pixel to the reference pixel

$$\min_{a_{\text{Mie}} \in \mathbf{R}} |a_{\text{Mie}}[\ln(1 - E_{\text{Mie}}(\nu))] - \ln(1 - E^{\text{ref}}_{\text{Mie}}(\nu))|. \tag{3.3}$$

Note that a_{Mie} (and also a_{atom} below) is a scalar independent of ν. Having obtained a_{Mie}, we can rewrite Eq. (3.2) with only known parameters

$$\sigma_{\text{rel}}(\nu) = -\frac{\ln(1 - E(\nu))}{a} \frac{1}{\ln(1 - \tilde{E})}, \tag{3.4}$$

with a single normalization applied to all intensity cases at $\tilde{E} \equiv E^{\text{ref}}(\nu = 42\,000\,\text{cm}^{-1})$ from a single pixel [near the blue pixel indicated in Fig. 3.2(f)] in the 5×10^7 W/cm^2 case enabling the direct comparison to Ref. [76]. The rewriting of the equation allows us to show how the cross section changes over wavelength, regardless of the density-length scale product. This evolution is especially important in Mie theory, where the evolution of the cross section with wavelength is solely determined by the nanoparticle size (together with the refractive index). The resulting relative cross section σ_{rel} is shown in the third row of Fig. 3.2. The atomic resonances are filtered out to focus on the broadband component of the spectrum. Again, the results of selected pixels (cf.

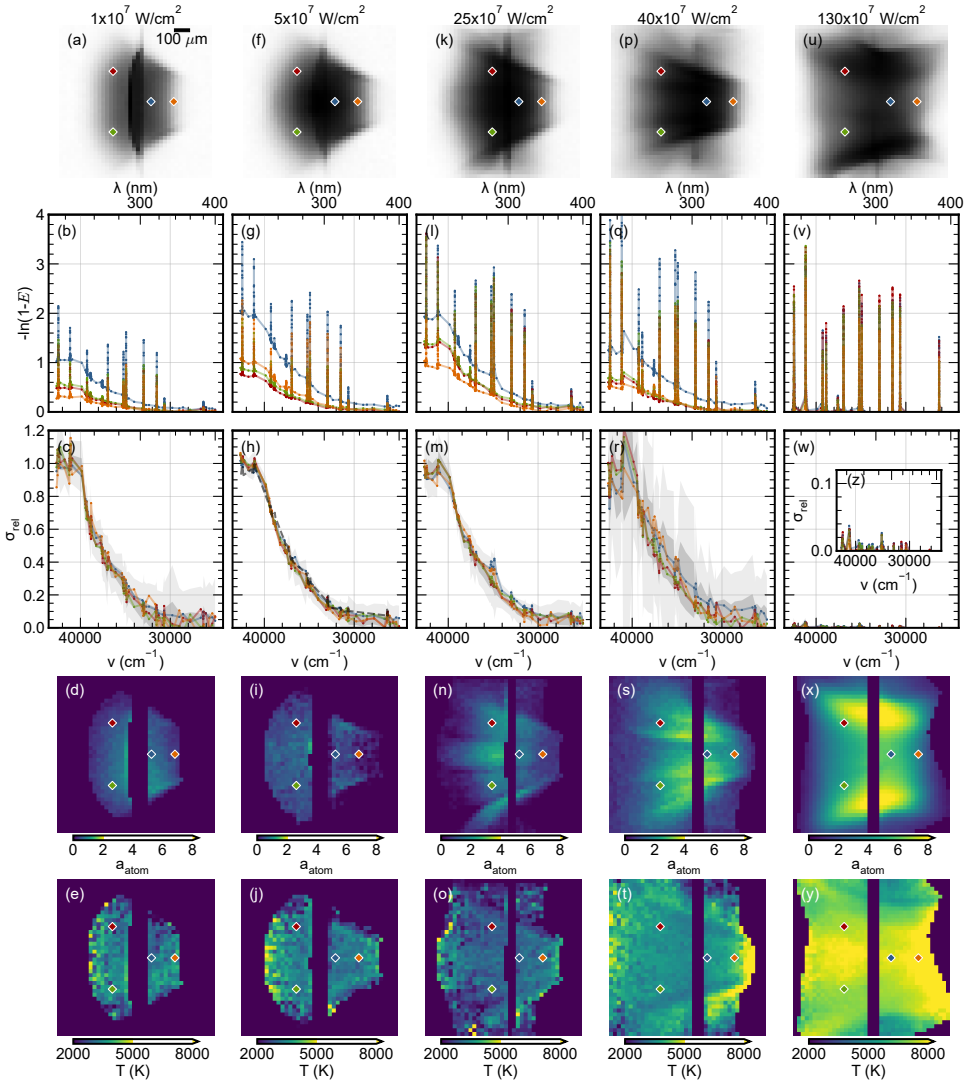

FIGURE 3.2: Analysis of tin vapors at five laser vaporization intensities. Row 1 shows shadowgrams of the relatively weak 254.73 nm atomic resonance ($5s^2 5p^2\ ^3P_0$, see Table 3.1), showing detailed structures in the atomic vapor cloud and highlighting the shape change of the vapor with VP intensity. Row 2 shows the extinction spectra for the four highlighted locations in row 1. Row 3 shows the relative cross section (σ_{rel}) for the four locations (the atomic resonances are filtered out). We also indicate the spread over all the pixels (at 1 and 3 standard deviations; gray shading). Panel (h), which closely matches previously published data (see the main text), also shows (gray dashed line) the previously published mean for all pixels for comparison. Row 4 shows the relative, unitless, densities a_{atom} determined using the atomic resonances. Pixels where no value could be determined are colored dark blue. Row 5 shows the temperature maps for each intensity.

Fig. 3.2 row 1) are shown, along with two gray bounds (dark and light gray) indicating the 1 and 3 sigma spread for *all* the pixels in the vapor, respectively. Panels (c,h,m) show nearly identical curves, indicating that all pixels in the vapor have the same nanoparticle size distribution underlying this broadband spectrum. The gray bounds are very small, indicating a particular uniformity of the size distribution throughout the vapor. We note that this uniformity holds over a 25x change in VP intensity. The uniformity breaks down in Fig. 3.2(r) at 40×10^7 W/cm^2. Although the same trend in the broadband spectrum is still visible, the variation in vapor increases significantly, as indicated by the much larger gray bound [cf. Figs. 3.2(m,r)]. Finally, for the highest intensity case [Fig. 3.2(w)] the broadband component disappears completely. The inset (z) presents a close-up view of panel (w) with the same data (10x zoom on the y-axis) and clearly shows that the broadband is negligible. Thus, it appears that the nanoparticles deemed responsible for the background component have disappeared completely.

Given that the broadband component is absent at the highest intensity, it is advantageous to instead define a via the atomic resonances, which are still very much present in this highest intensity case. We sum over a full atomic resonance (to accommodate varying broadening effects due to varying density) to obtain an integrated line strength. By comparing the line strengths for different pixels, we again obtain a value for a much like Eq. (3.3)

$$a_{\mathrm{atom}} = \frac{\sum^{n_{\mathrm{peaks}}} \sum_{\nu_{\mathrm{min}}}^{\nu_{\mathrm{max}}} \ln(1 - E_{\mathrm{atom}}(\nu))}{\sum^{n_{\mathrm{peaks}}} \sum_{\nu_{\mathrm{min}}}^{\nu_{\mathrm{max}}} \ln(1 - E^{\mathrm{ref}}_{\mathrm{atom}}(\nu))}, \tag{3.5}$$

where ν_{max} and ν_{min} are 0.4 nm around each atomic resonance (cf. Fig. 3.1(c) for example of the summation range). Previous work[76] demonstrated that the two methods to obtain a representative relative density a provide very nearly identical values, with the a_{Mie} exhibiting a better signal-to-noise ratio and having the advantage of being insensitive to complex atomic broadening dynamics. Hence, we use a_{Mie} to collapse σ_{rel} in panels (c,h,m,r); for the highest intensity case (w) we resort to using a_{atom}. The values for a_{atom} are of particular interest for a consistent interpretation of the spatial changes in the relative density when varying the intensity of the VP in the following.

Imaging

Our spectroscopic imaging method enables us to spatially characterize the relative densities for the various VP intensities used. The fourth row in Fig. 3.2 shows the determined values of a_{atom} for each pixel. Similarly to σ_{rel}, the relative density a_{atom} is normalized by its value for the same single pixel in the 5×10^7 W/cm^2 case. This

single normalization enables the direct comparison of the relative densities between all the VP intensities used. In general, a trend to higher values for a_{atom} is observed as intensity increases. In part, this trend is explained by more vaporized mass as the fluence increases with intensity. We note that the rim and center mass hold nearly as much mass as the sheet itself for this target[71] and continue to be a source of atoms. Another factor in explaining the observed trend may be the redistribution of the vapor mass constituents, as the broadband component due to nanoparticles disappears and this mass shows up as free atoms. This mass redistribution is clearest in Fig. 3.2(x), the highest intensity case, without a broadband component in the spectra, where the values for a_{atom} have risen to $\sim$ 8x the value of panel (i). The highest values for a_{atom} are near the edges of the vapor, likely originating from the thick rim, a source of many atoms at high fluences.

We can also employ the Boltzmann plotting method for each pixel at each intensity. The final row shows the resulting temperature maps. The first four intensities [panels Fig. 3.2(e,j,o,t)] do not deviate significantly from a ~3000 K temperature in the vapor, near the boiling point of tin (at 2875 K). However, the temperature jumps to around 8000 K for the final intensity in panel (y). The hottest area seems to be around the center. This could be explained by the presence of the center dot feature here, which is the thickest and thus sustains a plasma the longest before vaporizing.

Scaling of key parameters

We leave behind the imaging and investigate key parameters of the vapor over the two orders of magnitude change in VP intensity. In Fig. 3.3, we plot the mean and spread over *all* pixels for the various parameters as a function of laser intensity.

First, we show the extracted temperature in Fig. 3.3(a) as it rises from the boiling temperature towards 8000 K. The rather sudden temperature increase is observed to coincide with the formation of plasma. In panel (a), the light gray background represents the onset of plasma on the thicker parts of the target (being the rim and center dot), while the dark gray area indicates the intensity region at which plasma is seen to form everywhere on the sheet. These regions are also indicated in panels (b,c,d). Next, we show the change in the relative density a_{atom} in Fig. 3.3(b). Starting around 1 ($a_{\text{atom}} = 1$ is defined for one pixel in the 5×10^7 W/cm^2 case), the relative density increases with the laser intensity. The large monoatomic vapors created with high VP intensities could be excellent targets to effectively absorb a following (main) laser pulse in EUV lithography, as such vapors offer a long path length of absorbers.

Next, we turn toward the broadband part of the spectrum, which is associated with scattering from nanoparticles. Comparing Figs. 3.2(m,r,w), we observe a strong reduction in this broadband part of the spectrum, indicating that the nanoparticles

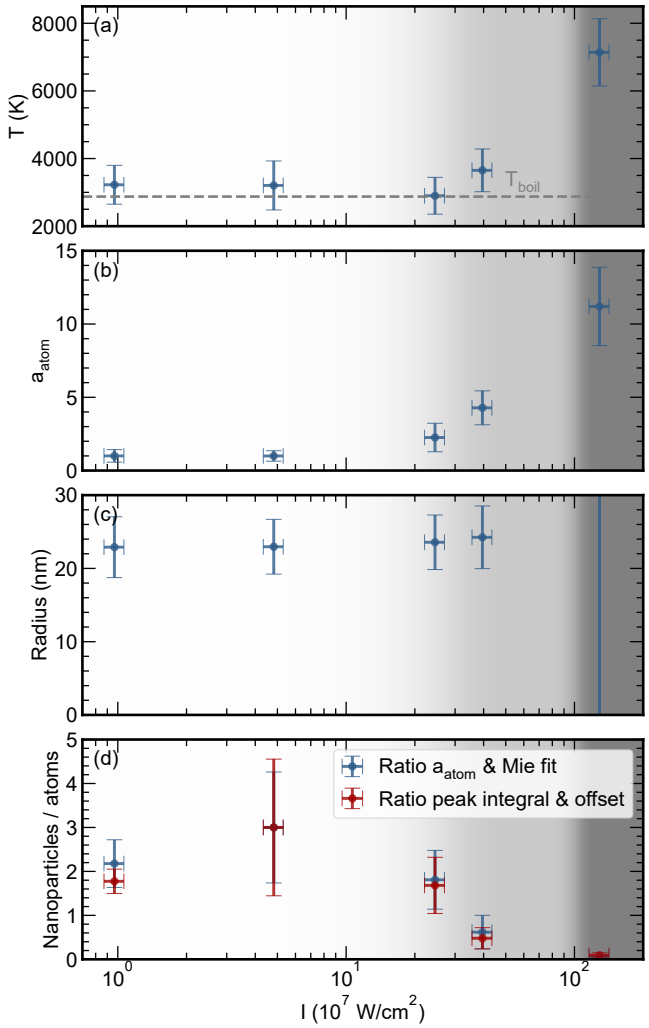

FIGURE 3.3: Key parameters over VP intensity. (a) The temperature of the vapor. The boiling temperature (2875 K) is also indicated. The gray-shaded background indicates whether plasma forms on the thin film. In the light gray area, the intensity is high enough to form plasma on the 'thick' features of the target, such as the center dot and rim. In the dark gray area, plasma forms on the entire thin film. We plot the mean and spread over all pixels as an error bar. (b) The relative density of the atoms a_{atom}. (c) The fitted nanoparticle radius. A fit is performed per pixel. (d) The mass ratio of nanoparticles and atoms. This value is set to three at 5×10^7 W/cm^2 (matching previously published work).[76]

disappear at the highest intensity. To quantify the change in the composition of the vapor, we fit each spectrum per pixel (after filtering out the atomic resonances) with the extinction curve predicted by Mie theory. We use a numerical code[85] for Mie theory and use as input the refractive index data from Cisneros *et al.*,[89] extrapolated to wavelengths below 310 nm using a Drude-model fit. This fit results in a column density and a best-fit nanoparticle size for each pixel.

In Fig. 3.3(c), we show the result of these fits by showing the mean and spread of the nanoparticle size. At low intensities, the nanoparticle radius obtained from the fit is nearly constant, around 23 nm, in line with the finding of Ref. [76] that the radii are at, or below, the 25 nm level. However, as plasma is formed at the highest intensity, the fit fails (indicated by the vertical blue line) due to the negligible remaining signal in the broadband curve. We note that the Mie theory fit carries significant uncertainties due to the work function of tin being passed around 280 nm (thus allowing ionization of clusters) and the fact that we extrapolate the refractive index below 310 nm.

We now focus on the column density of the nanoparticles. We obtain this value (in nanoparticles per volume) from the same fit for each pixel and convert it into atoms in nanoparticles per volume. Having obtained this value for each pixel, we now have a value for the change in atomic density (our relative atomic density a_{atom}) and a value for the change in nanoparticle density. With both of these, we can determine how the ratio of atoms contained in nanoparticles versus free atoms changes with VP intensity and show the results in Fig. 3.3(d). We set the ratio of nanoparticles versus atoms to 3 at the 5×10^7 W/cm^2 intensity, using input from Ref. [76] as a reference value. A clear downward trend of the ratio with increasing laser intensity is observed. The uncertainty is dominated by the uncertainty in the nanoparticle size, but also includes a measure of the spatial variation throughout the vapor.

We next confirm this trend in the ratio by introducing a second metric that has no model dependence. Here, we compare the integral under the 235 nm atomic resonance (see Table 3.1, this resonance has the highest broadband baseline) to its broadband baseline, caused by the nanoparticles. Thus, by tracking how the ratio of the integral of E_{atom} and the baseline changes, we obtain a proxy for the bound-to-free-atom ratio. These results are shown in Fig. 3.3(d) in red. Again, we fix the resulting ratio to 3 at the 5×10^7 W/cm^2 intensity. This independent, model-free approach closely matches that of the Mie fit and enables us to conclude that the ratio strongly decreases with the VP intensity to create a nearly pure atomic vapor at the highest VP intensity, effectively transferring mass from bound to free atoms and increasing atomic absorption cf. Fig. 3.2(i–x).

Overall, we have shown that the various vapors are quite similar, with respect to their spectral and spatial aspects, over the intensity range 1–25 $\times 10^7$ W/cm^2. This

similarity indicates that vaporization in this intensity range is governed by the same physical processes as those identified by Schubert *et al.*[141] given the partial overlap on the lower end of the studied intensity range ($0.2–4 \times 10^7$ W/cm^2 in cf. Ref. [141]). The dissimilarity of the vapor at the highest intensity, in particular the absence of broadband absorption, indicates that a different physical process starts to contribute. It remains an open question what is the exact process that causes the transition to a nearly pure atomic vapor at the highest intensity, around the plasma threshold. We hypothesize that plasma prevents the formation of clusters from the flux of free atoms coming from the liquid surface.[141] However, to prove this decisively versus an alternative hypothesis such as plasma-induced atomization of clusters, further studies are required.

3

Conclusion

In this work, we report on the spectroscopic imaging of pure metallic tin vapors generated from thin liquid tin targets over a range of intensity of the vaporizing laser pulse, from below to above the threshold of producing plasma. We show that vapors created with laser intensities below 40×10^7 W/cm^2 consist of a spatially homogeneous atomic component, with a temperature around 3000 K, and a strong broadband component due to nanoparticles. The vapor morphology and composition change considerably as plasma forms at higher intensities, with the temperature rising to 8000 K at the highest intensity. Here, the broadband component completely disappears, indicating that the vapor is composed of free atoms only. With the current studies, we demonstrate the applicability of the spectroscopic imaging method also in the regime of plasma generation.

Acknowledgments

This work was conducted at the Advanced Research Center for Nanolithography (ARCNL), a public-private partnership between the University of Amsterdam (UvA), Vrije Universiteit Amsterdam (VU), Rijksuniversiteit Groningen (UG), the Dutch Research Council (NWO), and the semiconductor equipment manufacturer ASML and was partly financed by 'Toeslag voor Topconsortia voor Kennis en Innovatie (TKI)' from the Dutch Ministry of Economic Affairs and Climate Policy. This publication is also a part of the project 'Plasma driven by a variable-wavelength laser for next-generation EUV sources for nanolithography' (with project number 19458) of the Open Technology Programme which is financed by NWO.

The authors thank Michael Purvis and Haining Wang for valuable discussions and ASML for loaning a laser system. We would also like to thank Henk-Jan Boluijt and

Laurens van Buuren for their work on the experimental setup and Jorijn Kuster for his work on the acquisition software.

Appendix

Atomic resonance overview

An overview of all measured atomic transitions is presented below.

TABLE 3.1: An overview of the measured atomic transitions for neutral tin.[77] Vacuum wavelengths are used.

λ (nm)	Einstein coefficient (1/s)	Transition	Level energies (cm^{-1})
235.56	1.70×10^8	$5p^2\,{}^3P_1 - 5p5d\,{}^3D_2$	1692 – 44144
242.24	2.50×10^8	$5p^2\,{}^1D_2 - 5p5d\,{}^1F_3$	8613 – 49893
243.02	1.50×10^8	$5p^2\,{}^3P_2 - 5p5d\,{}^3F_3$	3428 – 44576
254.73	2.10×10^7	$5p^2\,{}^3P_0 - 5p6s\,{}^1P_1$	0000 – 39257
257.24	4.50×10^7	$5p^2\,{}^1D_2 - 5p5d\,{}^3D_3$	8613 – 47488
266.20	1.10×10^7	$5p^2\,{}^3P_1 - 5p6s\,{}^1P_1$	1692 – 39257
270.73	6.60×10^7	$5p^2\,{}^3P_1 - 5p6s\,{}^3P_2$	1692 – 38629
284.08	1.70×10^8	$5p^2\,{}^3P_2 - 5p6s\,{}^3P_2$	3428 – 38629
286.42	5.40×10^7	$5p^2\,{}^3P_0 - 5p6s\,{}^3P_1$	0000 – 34914
303.50	2.00×10^8	$5p^2\,{}^3P_1 - 5p6s\,{}^3P_0$	1692 – 34641
317.60	1.00×10^8	$5p^2\,{}^3P_2 - 5p6s\,{}^3P_1$	3428 – 34914
326.33	2.70×10^8	$5p^2\,{}^1D_2 - 5p6s\,{}^1P_1$	8613 – 39257
380.21	2.80×10^7	$5p^2\,{}^1D_2 - 5p6s\,{}^3P_1$	8613 – 34914

Chapter 4

Full Energy Partitioning in 2-µm-Wavelength Laser Driven EUV Sources

Dion Engels*, Felix Kohlmeier*, Yahia Mostafa, Edcel Salumbides, Bas Slotema, Ronnie Hoekstra, John Sheil, Wim Ubachs, and Oscar Versolato.
Submitted.

State-of-the-art nanolithography uses extreme ultraviolet (EUV) radiation at 13.5 nm emitted from tin laser-produced plasma (LPP), driven by a 10.6-µm-wavelength CO_2-gas laser, to create the smallest features on semiconductor devices. Advances in solid-state laser technologies have led to the alternative concept of a 2-µm-wavelength-driven LPP as a promising candidate for a more efficient and more powerful EUV source. We present the complete energy partitioning for a 2-µm-wavelength-driven LPP, reconstructing the full input laser energy. With ∼70 %, most of the energy goes into photons, the largest part of which is emitted in the 5–80 nm wavelength range. Plasma ions contribute ∼30 % of the energy, and, contrary to available theory and numerical simulations, we find that this fraction decreases as a function of the laser intensity, a key insight in finding pathways to optimize plasma for industrial application. Our results offer insight into the energy partitioning of EUV-emitting plasmas for research and industrial nanolithography alike, and provide a benchmark for plasma light source development.

* These authors contributed equally to this work. Dion was in charge for the experimental campaign, analysis of the ions and neutrals, and writing. Felix was the main responsible for the laser system and the EUV-related diagnostics.

Introduction

Modern nanolithography machines use extreme ultraviolet (EUV) light to create the most advanced semiconductor devices. To produce this EUV light, tin microdroplets are first laser-shaped into disk targets[35–37,111,142,143] which are subsequently illuminated with 10.6-µm-wavelength pulsed laser light, generating plasma containing highly charged, multiply excited tin ions.[144–147] These ions emit EUV light in the desired ±1 % 'in-band' region around 13.5 nm that is reflected by the Mo/Si multilayer mirrors used.[27,28,148,149] A key performance indicator of these laser-produced plasmas (LPPs) is the conversion efficiency (CE): the ratio of laser energy to in-band EUV energy emitted into the 2π hemisphere covered by a collector mirror. State-of-the-art industrial EUV sources, driven by 10.6 µm CO_2 gas laser technology, have CEs of 5–6 %,[26,35,142] with ongoing developments to improve their total EUV output and, with it, the wafer throughput of lithography machines.[33]

The concept of an LPP driven by 2-µm-wavelength laser light has gained traction as a promising alternative candidate in the quest for even more efficient and more powerful EUV sources.[29,42,150–152] This activity has been fueled by the rapid development of powerful 2 µm solid-state laser technology[153–155] with the promise of wall-plug efficiencies much higher than CO_2 systems, and pioneering LPP experiments using 2 µm lasers.[29,30,150,151,156] These experiments showed that competitive CE values of up to ∼4.5 % can be achieved in a 2-µm-driven system when using a disk target.[30] Radiation hydrodynamic simulations furthermore hinted at the viability of EUV sources driven by 2 µm light without the need to first create a disk target,[45] which would strongly simplify the system when suitable long-pulse lasers would become available.

Conversion efficiency, however, is only one figure of merit for EUV-emitting plasmas. A holistic view of all relevant channels distributing the energy of an LPP (see Fig. 4.1) is required to assess the applicability of new source concepts to EUV lithography. Previous studies have investigated the anisotropy of EUV emission, key to obtaining reliable CE values, specifically for plasmas driven by 2 µm lasers[29,30,150–152,156,157] and other drive laser wavelengths.[40,83,136,139,158–176] Many studies have focused on the emission spectra of tin plasmas in general, identifying charge states and other features prominent in radiative emissions to understand the origins of EUV emission[28,177–191] or quantifying photon yields in a wide range of wavelength bands.[56,192–199] The kinetic energy, number, and anisotropy of ions emitted from the plasma[121,200–212] and their interaction with the plasma surroundings[212–220] have also been studied in detail; such studies are key to designing effective mitigation strategies (which typically involve a H_2 buffer gas) to avoid ion-induced damages.

Yet, in spite of the importance of a holistic view, there are no experimental studies available in the public literature that quantitatively combine all of the above channels. In this work, we quantify the *full* energy partitioning for 2-µm-wavelength-driven laser-produced plasmas. The independently measured total energy of the dissipation channels matches the input laser energy over a wide range of drive laser intensities. Thus, a complete picture of the output of an EUV-emitting plasma is obtained.

Results

The experiment is described in detail in Methods with the main elements summarized here. We create a tin disk in a vacuum environment from a tin droplet using a laser pre-pulse.[36,37,39,70] This tin disk is illuminated with a 2-µm main pulse to create an EUV-emitting plasma, cf. Fig. 4.1. The main pulse originates from a laser system[51]

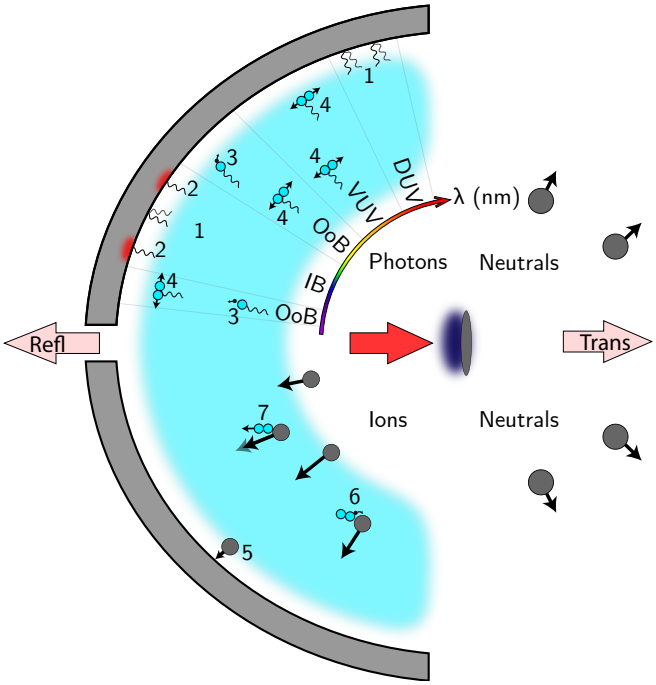

FIGURE 4.1: Schematic of an industrial laser-produced plasma EUV source and its energy partitioning channels. A preformed tin disk is illuminated with a high energy ns-laser pulse (red, can also transmit or reflect) to generate plasma. Photons and ions, each of a wide range of energies, interact with the surrounding hydrogen buffer gas (blue) and, if not mitigated, the collector mirror. Finally, neutral tin can also be left over after the plasma extinguishes. The numbered processes indicate the various interaction channels (see the main text).

producing high-energy pulses to enable exploratory lab scale experiments at 10 Hz repetition rate, well below that of industrial levels at several 10 kHz. We further note that our setup does not include buffer gas or a collector mirror. For homogeneous heating of the plasma, optimizing CE, the main pulse has a temporal box-shape, and its spatial flat top is imaged onto the disk target.[30,45,156] The various types of emission from the plasma are measured by absolutely calibrated in-band EUV diodes, a spectrometer, and a set of ion diagnostics mounted to the vacuum chamber. Additionally, we capture the experiment with shadowgraphic imaging and measure the laser profile, reflection, and transmission with 2-µm-sensitive photodiodes.

Plasma photons

Emitted photons affect the surroundings of the plasma and interact in the EUV lithography machine in different ways. The in-band radiation window used in EUV lithography, (IB, 13.5 nm ±1 %) is set by the reflection bandwidth of the multilayer mirror (Fig. 4.1 process 1). Since ≳30 % of these IB photons is absorbed by the mirror,[17] they may reduce the performance of the multilayer mirrors via heating or deformation (process 2).[221,222] The surrounding out-of-band EUV photons (OoB, 5–80 nm, excluding IB) interact with the H_2 buffer gas, that embeds the LPP under industrial operating conditions, via photoionization and photodissociation (processes 3 and 4)[223] to form a secondary hydrogen plasma, which can affect nearby optics.[224] Vacuum ultraviolet (VUV, 80–130 nm) radiation is absorbed by the H_2 gas inducing photodissociation (process 4) but has photon energies below the ionization threshold of H_2[223] and does not contribute to direct secondary plasma formation. Finally, deep ultraviolet (DUV, 130–265 nm) can in fact be reflected by the multilayer optics (process 1) towards the wafer and affect the contrast of the exposure in the nanolithographic process;[145,198] the upper limit (265 nm) here is set by our spectrometer.

Figure 4.2(a) shows 5–265 nm emission spectra for three (of seven measured) main pulse laser intensities: 2×10^{10} W/cm^2, 6×10^{10} W/cm^2, and 26×10^{10} W/cm^2. Each spectrum is normalized to the area under the curve to highlight the shift of the emission spectrum to shorter wavelengths with increasing laser intensity. Figure 4.2(b) zooms in on the 13.5 nm in-band region. It is immediately visible that in-band 13.5 nm radiation is strongest for the 6×10^{10} W/cm^2 intensity case. Three additional features are noted [and are labeled accordingly in Fig. 4.2(b)]. First (1) are well-defined peak structures between 7 and 10 nm for the two highest intensities. These structures originate from highly charged tin ions of charge states 12+–15+.[188,189] They become more pronounced at the highest laser intensity shown, where additional line structures (associated with charge states beyond 15+) also appear at the shortest wavelengths. Second (2) is a shoulder to the main emission peak around 15 nm that is due to the emission by Sn^{7+}, and thus is only prominent until the laser intensity reaches the

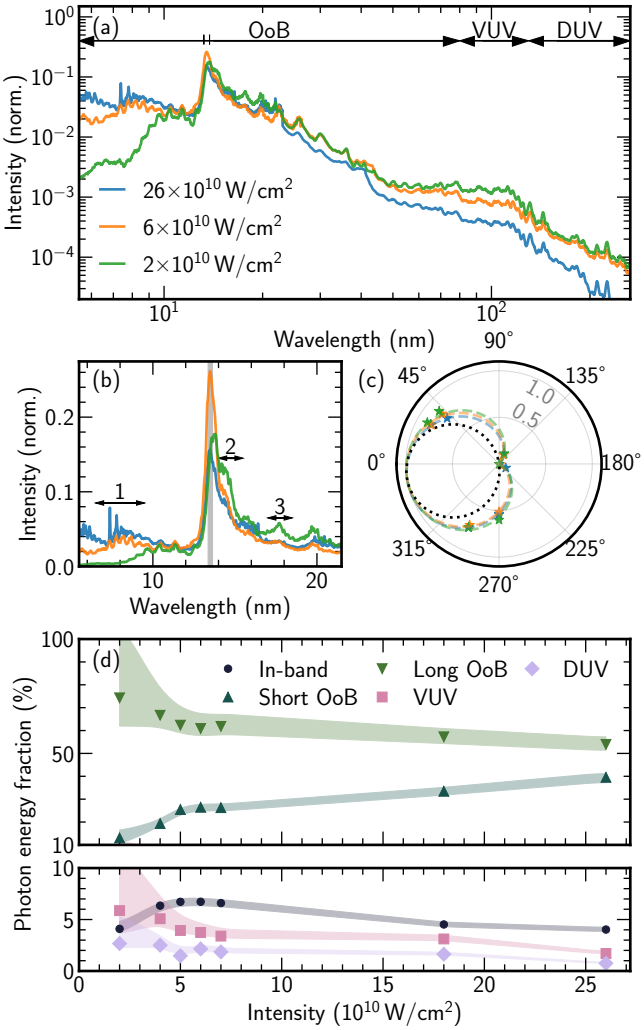

FIGURE 4.2: Photon energy partitioning. Panel (a) shows the full spectrum 5–265 nm for three laser intensities. Each spectrum is normalized to have a constant area under the curve. Panel (b) shows a zoom-in on the 13.5 nm in-band region for the same three laser intensities, with three features highlighted (see main text). The in-band region is denoted in gray. Panel (c) shows the anisotropic emission of the in-band EUV light as measured by EUV-sensitive photodiodes with a cosine function for reference in black (laser incident from left). Panel (d) shows the resulting photon energy partitioning, splitting the emissions into in-band EUV (13.5 nm ±1 %), short OoB (5–13.4 nm), long OoB (13.6–80 nm), VUV (80–130 nm), and DUV (130–265 nm), see the main text.

optimum.[187] Third (3) is a small peak at 17.5 nm that is associated with Sn^{6+} and is only visible at very low drive laser intensities.[171,191]

We next quantitatively study the evolution of the charge states z (the average of which $\bar{z}$ scales with the plasma temperature T as $\bar{z} \propto T^{0.6}$ [44,219,225]) of the emitting Sn ions as a function of the laser intensity. We do this by fitting individual emission features in the 7–11 nm range using a method introduced by Torretti *et al.*,[189] see Methods. This approach to obtain a plasma temperature yields a power law scaling of the plasma temperature T with laser intensity as $T \propto I^{0.3(1)}$, somewhat weaker than the $T_e \propto I^{0.44-0.6}$ scaling found from modeling[44,226,227] and more in line with Torretti *et al.*, who found $T \propto I^{0.2}$ for a plasma driven by a CO_2 laser. We hypothesize, following Torretti *et al.*, that the weaker-than-expected scaling may reflect the limited validity of using a single temperature in describing a complex evolving plasma that is not perfectly homogeneously heated. On the other hand, we also note that the aforementioned models do not take into account the radiative loss fraction[44] that changes with the laser intensity. Regardless, the weak scaling supports a steady performance in terms of the emission of in-band radiation over a wide range of intensities.

The anisotropy of the in-band EUV emission is shown in Fig. 4.2(c). The data points for the individual EUV diodes, and the results of a fit (see Methods) to the data, are normalized to their respective maxima. The emission is strongly anisotropic, relatively close to Lambert's cosine law (which describes the angular emission of a diffuse planar emitter), and this anisotropy does not change with the drive laser intensity.

Fig. 4.2(d) shows the photon energy fractions emitted in the various wavelength bands. The out-of-band is split into short (5–13.4 nm) and long OoB (13.6–80 nm). For each intensity, the values are normalized to the total photon energy across the full wavelength range, highlighting relative changes in emission. Thus, the photon energy fractions sum to 100 %. The uncertainties (see Methods) on the energy fractions are visualized with colored bands. The IB peaks at a laser intensity of 6×10^{10} W/cm^2, around the expected optimum intensity for CE,[150] and slowly decreases for higher drive laser intensities.[30] The largest fraction of light is in the OoB range, accounting for more than 80 % of the radiation. The fraction in short OoB increases from 10 % to 40 % when the laser intensity is increased by an order of magnitude, reflecting a higher plasma temperature and with it enhanced emission from the higher charge states. Long OoB emission decreases steadily with increasing intensity, as expected given that line radiation here comes from low charge states whose presence decreases with laser intensity. VUV emission accounts for up to 6 % of the output at the lowest intensity, but is typically around 3 %. DUV emission carries only ∼1 % of the total

energy emitted in photons. Both VUV and DUV emission fractions reduce for increasing laser intensity. This reduction could be beneficial for exploring pathways that aim to minimize spurious DUV exposure of the wafer.

Plasma ions

Quantifying the ion emission of the plasma is important as ions, the debris of the plasma, are a risk to surrounding diagnostics and optics, especially the collector mirror, which focuses the EUV light and sends it further into the lithography machine. The impact of keV ions would lead to sputtering or implantation (Fig. 4.1 process 5), degrading mirror performance.[228] To avoid ion impact, the ions are stopped by an H_2 buffer gas. Ions interact with the buffer gas through inelastic (electron capture, molecular fragmentation, process 6),[217,218,220] and elastic (kinetic energy loss, process 7) collisions.[215]

Figure 4.3 shows the kinetic energy distributions of plasma ions for laser intensities ranging between $2–26 \times 10^{10}$ W/cm^2. Figure 4.3(a) shows the energy spectrum recorded by the ion diagnostic (see Methods) set up at 64° for three different laser intensities (cf. Fig. 4.2). A wide range of ion energies are present in the spectrum, with a relatively constant contribution between 50–500 eV, followed by a drop. The energy position of this drop increases with laser intensity in line with predictions that the kinetic energy of plasma ions (E_{kin}) scales as $E_{\mathrm{kin}} \propto \bar{z}T$[229] and thus as $E_{\mathrm{kin}} \propto I^{0.5(2)}$ by inserting the previously found scalings. We note that the spectrum is relatively smooth as in Refs. [166, 200, 206, 229] and does not feature any peaks such as those prominently observed for 1 µm laser impact on a droplet.[120,121] Differences in wavelength, temporal pulse shape (from Gaussian to box-shaped), as well as geometry of the system could underlie the presence or absence of the ion peak. In addition to the changes in the ion energy distribution, the overall amplitude of the spectrum also increases with laser energy. This follows the expectation since the mass ablation rate (for tin planar targets) was found to scale as $\dot{m} \propto I^{0.6}$.[230,231] The total number of ions detected (integrating over all angles) in our experiment closely matches this scaling, yielding $N_{\mathrm{ion}} \propto I^{0.6}$.

In addition to recording overall charge-energy dQ/dE spectra, our ion diagnostics can be used to reconstruct the individual spectra of the contributing charge states (see Methods). Such a reconstruction is required to be able to assess the total kinetic energy carried by the plasma ions. Figure 4.3(b) depicts an example charge-state-resolved spectrum for the 6×10^{10} W/cm^2 case. The raw data (dQ/dE) and the reconstructed total charge (with the individual charge states shown separately) agree well. Further comparisons are shown in Fig. 4.3(a) where dashed lines depict the total charge from the charge-state-resolved reconstructions. Overall, the reconstructed total charge

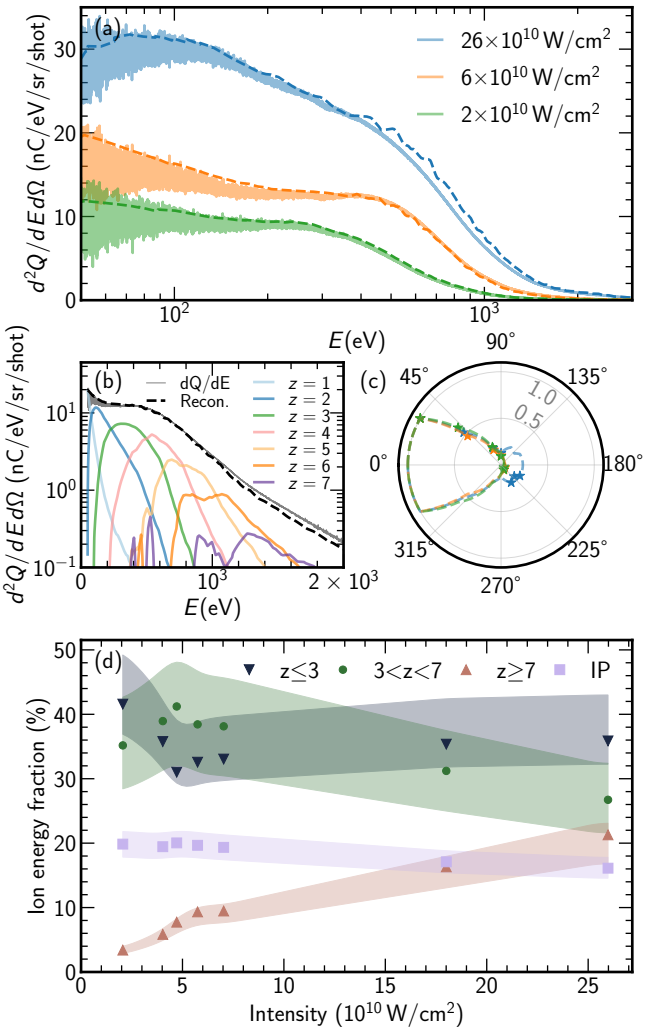

FIGURE 4.3: Ion energy partitioning. Panel (a) shows the kinetic energy spectra at 64° for three different laser intensities. The dashed lines are the result of our ion charge state reconstruction. Panel (b) zooms in on the ion charge state reconstruction performed for the 6×10^{10} W/cm^2 case at 64° compared to the overall charge-energy dQ/dE spectrum measured. Panel (c) shows the anisotropy of the ion emission as recorded by the seven ion diagnostics and the interpolating curve. Panel (d) shows the resulting ion energy partitioning. Four different components are shown: the first three are different charge state ranges, while the fourth is the potential energy carried by the ions (sum of sequential ionization energies, IP, see Methods).

is in agreement with the raw data, highlighting the quality of the reconstruction of the individual spectra. Charge states up to Sn^{7+} are shown; small amounts of up to Sn^{10+} are included in the reconstruction. Higher charge states become dominant with increasing ion energy.[219] We note that while Sn^{15+} is present in the plasma and its emission lines appear in the photon spectrum, these highly charged tin ions recombine into lower charge states during plasma expansion.[214,219,232] Thus, at the long distances of the detectors from the plasma (∼1 m, while charge state freezing already occurs at a distance of several 100 µm[219]), only lower charge states ≤ 10+ are detectable and only in the absence of any buffer gas[217] as in the current case.

Figure 4.3(c) shows the anisotropy in the kinetic energy of the plasma ions, normalized to the highest value. Curves interpolating the angularly resolved data are integrated to obtain an angle-integrated kinetic energy of the plasma ions. A dominant fraction of the ions is emitted in the hemisphere on the laser side, similar to the EUV emission but in a much narrower cone – in line with models that predict ions to be emitted predominantly along the surface normal.[204,214] Only in the highest-intensity case is a measurable but still small amount of ions emitted to the back side. This can be explained by the finite thickness of the target, which, with a thickness of 1.5 µm, is thick enough to sustain the plasma for the full duration of the laser pulse. At the highest laser intensities, however, the plasma is close to using up all the tin in the disk, and some ion emission starts appearing beyond a 90° angle relative to the laser.

Figure 4.3(d) presents the ion energy fractions (again summing to 100 %). Uncertainties (see Methods) are represented by transparent bands. The main change in the ion energy partitioning with laser intensity is the steady increase of the energy carried by the highest charge states, ≥ 7+. As mentioned above, this can be explained by an increased average charge state in the tin plasma, scaling as $\bar{z} \propto I^{0.2(1)}$, while the kinetic energy corresponding to this $\bar{z}$ is known to scale as $E_{\mathrm{kin}} \propto \bar{z}^{0.4}$.[219] Thus, the energy fraction carried by the higher charge states increases. In apparent contradiction, the fraction of potential energy carried by the ions remains relatively constant and even slightly decreases with intensity. This behavior can be understood by considering that the number of ions emitted scales as $N_{\mathrm{ion}} \propto I^{0.6}$ [230,231] and that the total energy to ionize a tin atom to an average charge $\bar{z}$ scales with $\bar{z}^{2.3}$.[77] These scalings are heuristically combined into a scaling of the value of the ionization potential in the energy partitioning $\mathcal{E}_{\mathrm{IP}} \propto N_{\mathrm{ion}} \bar{z}^{2.3} \propto I^{1.0(1)}$ and thus lead to a constant fraction when expressed as a ratio of the laser intensity (energy).

Power partitioning

Besides the ions and photons, there are three other small energy channels to be considered: laser reflection, transmission, and kinetic energy carried in neutral

tin. We measure laser reflection and transmission using high-speed photodiodes, sensitive to the 2 µm laser wavelength. The experimental data, in accordance with the simulations by Hemminga *et al.* and de Lange *et al.*,[42,45] indicate that some reflectance, at the percentage level, occurs at early times when the plasma is still in the process of forming. However, accurately determining the absolute value of this reflection is experimentally challenging. Therefore, since the signals show similar evolution in experiments and simulations, we adopt a common 1.5 % reflection value for all intensities, following prior simulation work.[42,45] No laser transmission through or around the target is observed. The final energy channel is that of the kinetic energy carried by neutrals in the form of atomic or liquid debris [see Fig. 4.4(a)]. We conservatively estimate (see Methods) that the neutrals carry at maximum 4 % of the energy at the lower intensities, decreasing to less than 1 % with increasing laser intensity mainly due to a higher ionization degree.

Figure 4.4(b) shows the full energy partitioning as a function of laser intensity. We show the total photon emission [a sum of the contributions of all wavelength ranges cf. Fig. 4.2(d)], total ion emission [a sum of all contributions cf. Fig. 4.3(d)], and the total reconstruction, which also includes the minor contributions from neutrals and reflection [cf. Fig. 4.4(a)]. For completeness, the in-band emission [part of the photon yield in panel (b)] is separately shown together with the CE (2π) in the zoom-in at the bottom. These two curves are nearly identical because of the constant anisotropy in the photon emission.

Adding all the contributions, we obtain an average total of 101(14) % with respect to the input laser energy, demonstrating a full reconstruction of the input laser energy.

We observe two main trends. First, CE peaks at 6×10^{10} W/cm^2, around the optimal intensity for EUV generation, and follows the expected behavior throughout the entire intensity range.[150] Underheated plasma cases quickly underperform in terms of CE, while the drop-off in CE with increasing laser intensity is slower. Our CE peaks at 3.5 %, somewhat lower than the ideal 4.5 %.[30,156] However, this CE value is expected for our beam with 66 % of its energy enclosed within the FWHM of the spatial beam profile (cf. Ref. [30] where the concept of enclosed energy was introduced as a beam quality metric of the top hat for the production of EUV). Second, the balance of photon and ion emission changes as a function of laser intensity, resulting in a decrease of ion emissions from approximately 40 to 25 % in the intensity range studied.

Next, we compare the energy partitioning values with simulations of a 2-µm-driven plasma by Hemminga *et al.*[42] to validate the predictive power of these simulations performed with a simpler case considering a spherical droplet instead of a disk. They find that 68 % of the energy is converted to radiation and 27 % goes into kinetics

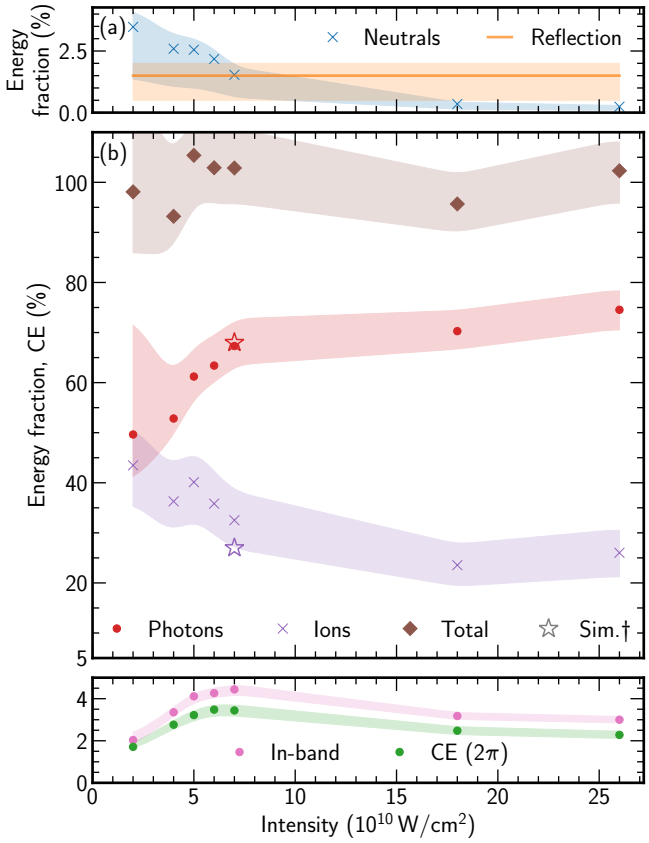

FIGURE 4.4: Energy partitioning as a function of laser intensity. Panel (a) shows contributions of laser reflection and neutrals being propelled by the plasma. Panel (b) shows the total energy partitioning shown together with the two main energy channels: ions and photons cf. Figs. 4.2 and 4.3. Simulation data points from Hemminga *et al.*[42] are also shown. The zoom-in panel at the bottom shows the CE (2π) as the typical parameter describing EUV-producing laser-produced plasma performance together with the total 4π in-band emission.

at the optimum intensity for CE, as also shown in Fig. 4.4. Other simulations also find 70–90 % energy in radiation[173,233,234] (a lower value of 30–45 % is reported in Ref. [235]). Around the optimum intensity (6–7 $\times$ 10^{10} W/cm^2 in Fig. 4.4), we find that ∼65 % of laser energy is channeled into plasma photons, and ∼28 % in ions, which matches the numerical results.

Hemminga *et al.* also studied the dependence of the energy partitioning on the drive laser intensity (over a range similar to ours) considering a 1-µm-driven plasma. They report an almost constant energy partitioning as a function of the laser intensity, in apparent contradiction to our experimental results for a 2-µm-driven system. We can resolve this contradiction when considering the weaker scaling of plasma temperature T uncovered in the current work, which propagates in the expected scaling for the kinetic energy flux density $\mathcal{E}_{\mathrm{Ions}} \propto \rho_s c_s^3 \propto (\bar{z}T)^{3/2} \propto I^{-0.3(2)}$ (with ρ_s the density at the sonic surface, here assumed constant, and the sound speed $c_s \propto \sqrt{\bar{z}T}$ [42,236]) consistent with our observations of a decreasing ion load with increasing laser intensity.

The complete energy reconstruction demonstrated in the current work provides key input toward industrializing a 2-µm wavelength EUV light source. Moreover, our findings also lead to a consideration of using a laser intensity higher than that leading to optimum CE: overheating the plasma at ∼3× the optimum would lead to a ∼30 % reduction of the ion load and a ∼12 % reduction in tin mass consumption per in-band photon at the expense of a reduction in CE of ∼25 %.

Conclusions

We quantify the energy dissipation channels for a 2-µm-driven EUV-emitting light source. The energy of all channels adds up to the input laser energy at all drive laser intensities, with an average deviation of just 1 %. The dominant energy channel is the emission of out-of-band (5–80 nm) light, which carries ∼45–70 % of the input energy, increasing with the laser intensity. With increasing light output, the number of atoms required per emitted photon decreases. A weaker-than-expected scaling of plasma temperature with laser intensity, uncovered in the current work, brings our experiments in agreement with pre-existing scaling laws. The second in importance is the fraction of energy channeled into plasma ions, which decreases from ∼40 to 25 % with laser intensity. This finding provides a path for limiting the energy in ions and mass usage, with a relatively small impact on CE. Our findings demonstrate the completeness of our efforts to reconstruct the energy partitioning of a 2 µm-laser-driven plasma light source that is considered as a promising alternative candidate for ever more powerful future EUV sources and provide key input toward industrializing

a 2-μm wavelength EUV light source. Moreover, we provide a benchmark for current and future plasma sources of EUV light and provide the required validated toolset for full diagnosis thereof.

Methods

Laser systems & Tin disk creation

We generate a stream of microdroplets by flowing liquid tin through a nozzle within a vacuum chamber at $\sim 10^{-6}$ mbar, as seen in Fig. 4.5. The tin microdroplet is deformed into a disk by a low energy 8 mJ 1 µm pre-pulse, visualized in the inset of Fig. 4.5. A Spectra-Physics Quanta-Ray Pro-250 Nd:YAG laser produces the 10 ns FWHM pre-pulse. We ensure that our energy partitioning measurements do not include (percentage-level) contributions from the pre-pulse by also taking measurements that include a pre-pulse but no main pulse, which are subsequently subtracted from the data. After a set time (1 µs), the 2 µm main pulse generates an EUV-emitting plasma from the tin disk. At this time delay, the disk is 245 µm in diameter and approximately ~1.5 µm thick (on average),[39] significantly larger than the 85 µm diameter ($1/e^2$) of the main pulse and thick enough to ensure that the plasma does not run out of tin for the full duration of the main pulse.

We generate the plasma by illuminating a tin disk with a high-intensity master oscillator power amplifier (MOPA) 2 µm main pulse laser.[51] The 2 µm main pulse laser operates at 10 Hz and emits a signal beam with a wavelength of 2080 nm (the idler output is not used).[51] The laser temporal profile is a uniform box-shape, shaped using a series of Pockels cells. We additionally optimize the spatial profile to be a top hat, which is imaged and demagnified into the vacuum chamber. The energy and intensity I of the main pulse can be changed by a combination of a half-wave plate and a thin-film polarizer. For this work, the pulse length of the laser is kept at 27 ns, where the highest energies, up to 300 mJ, can be produced from the laser system. The energy enclosed within the full width half maximum, E_{encl}, a metric for the quality of the top hat, of the beam is 66 % (cf. [30]) typical for the current system.

Diagnostics

A wide range of diagnostics are used to study the generated plasma, as visualized in Fig. 4.5. Emissions may be anisotropic with the angle α to the laser axis but are rotationally symmetric around the laser axis given the system's symmetry; thus, a single angle (α) describes the location of the various detectors w.r.t. the plasma. We typically capture 100 laser shots for each data point to improve signal-to-noise ratio. The uncertainty in the total reconstructed energy from its components is calculated based on the quadratic sum of the different components given by each diagnostic.

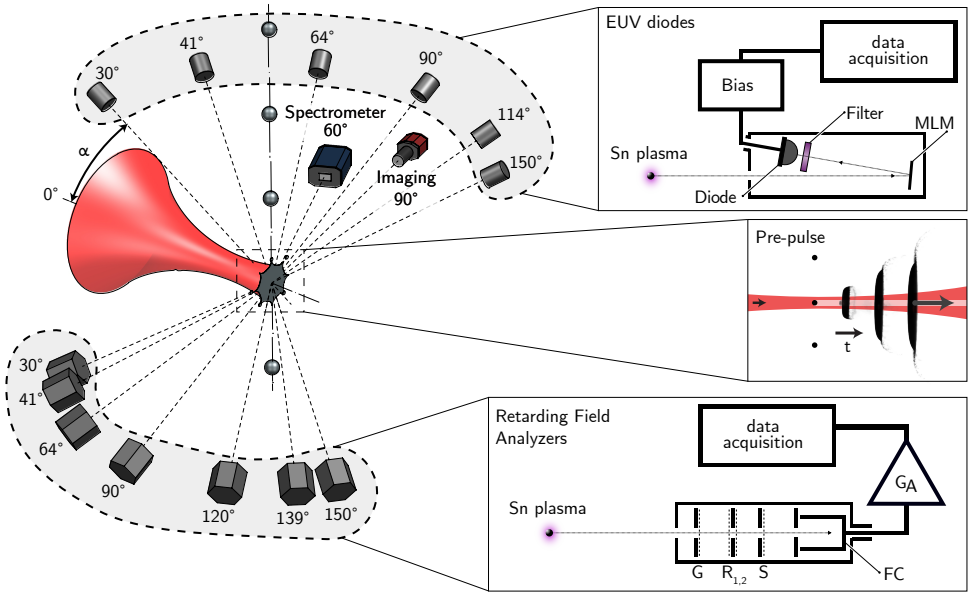

FIGURE 4.5: Schematic view of the experimental setup. At 0°, the imaged main pulse 2 µm-wavelength laser enters and hits the expanded tin disk. We use a pre-pulse to expand the droplet into a disk over time, as shown in the inset. The six EUV-sensitive diodes are shown at the top, with their respective angles to the laser indicated. The inset shows their working principle, with a multi-layer mirror (MLM) reflecting the in-band EUV light onto a photodiode that sits behind a filter. The diode is reverse-biased for faster charge collection. The bottom shows the seven retarding field analyzers (RFAs). Their working principle is shown in an inset as well. The RFAs use four grids: a ground grid, two retarding grids, and a suppressor grid stop the desired ions before the charge is collected in a Faraday Cup. After amplification, the signal is saved and processed. Clustering the detectors on one side is for visualization purposes; they are evenly distributed over both sides and all angles in the actual experiment. The 5–25 nm and 5–265 nm transmission grating spectrometer is at 60°. Finally, the shadowgraphy setup images the experiment using UV light, at 90°, to track the liquid before the main pulse and the liquid and vapor remains after the main pulse. The fast 2-µm-sensitive photodiodes are not shown.

In-band EUV

First, six absolutely calibrated custom in-band-EUV-sensitive photodiodes are placed at angles α=30°, 41°, 64°, 90°, 114°, and 150° to the laser axis. The diode angles, together with their working principle, are also shown in Fig. 4.5. The diodes are cross-calibrated to a synchrotron-calibrated diode not used in the experiments to avoid any degradation. The EUV in-band emission is calculated separately per diode for each laser shot. The anisotropy function of $E_{\mathrm{IB}}(\alpha) = a + b\cos(\alpha/2)^c$ is fit to the measured EUV values from the photodiodes to obtain the total emission of EUV light, following Schupp *et al.*.[151] This is converted to a shot-by-shot conversion efficiency (CE) by dividing it by the exact energy for that laser shot. The main source of uncertainty in the in-band EUV measurement comes from the calibration of the EUV diodes. They are calibrated before the experiment, but they degrade slightly in their response (on a percentage level) during the experimental campaign. The total uncertainty in the in-band EUV measurement ranges 5–10 % as visible for the individual diodes in Fig. 4.2(c).

Full emission spectrum

Second, we study the emission spectrum of the plasma using a transmission grating spectrometer,[198] placed at 60° to the laser axis. The transmission grating spectrometer has two modes of operation, a high resolution mode (0.11 nm resolution at 13.5 nm) to investigate the 5–25 nm range using a 10 000 lines/mm grating and a wide-range mode to study 5–265 nm using a 1000 lines/mm grating (with 0.8 nm resolution at 13.5 nm).[198] Exposures with various filters (Al, Si, MgF_2, LiF, Zr, UVFS, and 4B SiC), with exposure times varying between 1–500 s, are used to mitigate higher diffraction orders in the measured spectrum. The measured spectra for the different grating and filter combinations are stitched into one full spectrum after correction for filter transmission, diffraction efficiency, and CCD quantum efficiency (cf. Bouza *et al.*[198]). The spectra of the two diffraction gratings are combined into a single spectrum by first normalizing them to each other with the emissions in their overlapping range. Absolute emission values are obtained by normalizing the single obtained spectrum to the average in-band EUV emission during its ∼30 min capture. In calculating the total radiative energy, we assume that the spectrum does not change with the emission angle. Comparing this emission energy to the mean laser energy during the measurement gives a single value for the energy partitioning.

Several sources of uncertainty exist for the full emission spectrum. First, there is uncertainty in the stitching[198] of spectra from various combinations of filters and gratings into one spectrum, which is mitigated by having overlapping regions when stitching. The uncertainty band is estimated from the difference between the spectra

in the overlapping regions. Second, uncertainties arise from the quantum efficiency of the CCD, the efficiency of the grating, and the transmissions of the filters as discussed in Bouza *et al.*[198] Statistical noise is also factored into the uncertainty calculation, but is typically negligible. Third, an uncertainty arises from the assumption that the emission spectrum does not change with the angle to the laser axis. Explorative RALEF-2D simulations similar to those of Ref. [120] show that this assumption may lead to an error of by 5–10 % (relative) on the total reconstructed photon emission. Future work could incorporate multiple spectrometers, or multiple photodiodes sensitive to different wavelength bands, to study how the relative emission of wavelengths varies over angle. Combining this uncertainty with the other uncertainties mentioned above yields the error bars as presented in Fig. 4.2(d).

Plasma temperature

To obtain a plasma temperature, separate known spectra of charge states 9+–15+ are fit to the measured emission spectrum in the range to 7–11 nm where the contributions of the individual charge states can be clearly resolved, following Torretti *et al.*[189] An example of the result of this fit to the data is shown in Fig. 4.6(a). In this case and in the others, the model fit captures well over 90 % of the emission. As discussed by Torretti *et al.*, this fitting routine is a robust method to obtain radiation contributions for each charge state. We apply the method to cases with a laser intensity between 4×10^{10} W/cm^2 and 7×10^{10} W/cm^2, which is the intensity regime in which emission lines from 9+–15+ are dominant. The resulting relative contributions are shown in Fig. 4.6(b). The dependence of the plasma temperature on the laser intensity is deduced, following the methods of Torretti *et al.*, by taking the ratio of the $12^+/13^+$ contributions and comparing it with calculations from FLYCHK.[237] The result of this method is shown in Fig. 4.6(c) and shows a monotonically increasing temperature in this intensity range. The resulting scaling of the temperature with laser intensity at $T \propto I^{0.3(1)}$ is weaker than the values in the literature of 0.44[227] and 0.50[44] more in line (but still above) the weak $T \propto I^{0.2}$ scaling found by Torretti *et al.* for a CO_2 laser-driven plasma.[189] Several explanations that can affect the relatively weak temperature scaling are discussed in the main text.

Plasma ions

The third set of diagnostics comprises seven retarding field analyzers (RFAs, Kimball Physics FC73) ion diagnostics. These RFAs are placed at α=30°, 41°, 64°, 90°, 120°, 139°, and 150° to the laser axis, at a distance of ∼1 m from the plasma. Their working principle, including the grids used to stop the ions, is shown in Fig. 4.5. We incrementally vary the retarding voltage on the RFAs for a total of 60 voltage

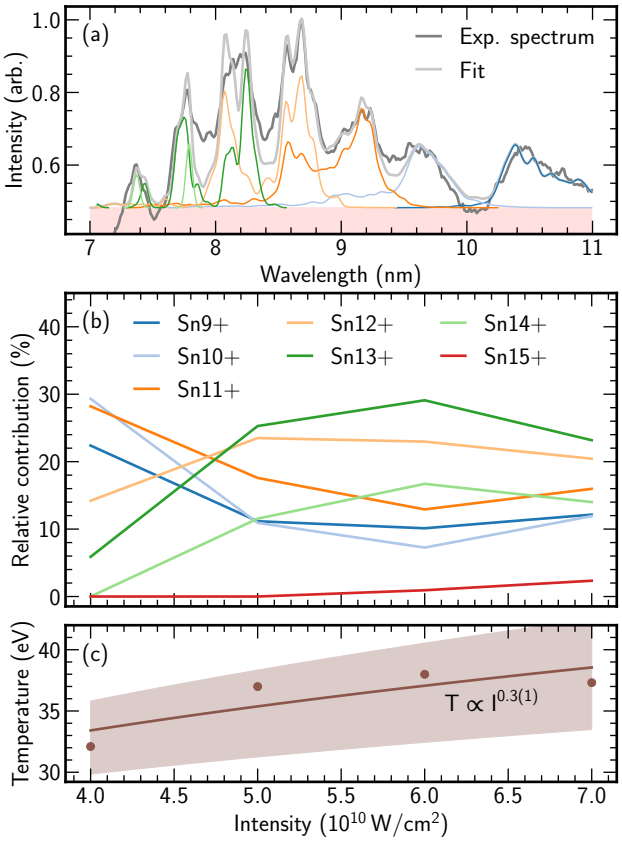

FIGURE 4.6: Temperature scaling of the plasma. Panel (a) shows an example of the fit of the charge-state specific emission peaks to the experimental spectrum at a laser intensity of 6×10^{10} W/cm^2. The underlying charge-state spectra contributing to the fit as well as the constant pedestal are additionally plotted. Panel (b) shows the evolution of the different charge states as the laser intensity is increased. Panel (c) shows the resulting estimated plasma temperature, together with a power law fit $T \propto I^{0.3(1)}$ with the transparent region indicating the uncertainty interval.

values, capturing 150 shots for each voltage. These 150 shots are averaged to improve signal-to-noise before the 'bottom-up analysis' is performed to obtain a charge-state-resolved energy spectrum (dN/dE) at each angle (cf. Poirier *et al.*[209]). These dN/dE spectra are integrated to obtain the energy (or momentum/mass) carried by the individual charge state and by all charge states combined. An anisotropy-corrected absolute energy of ion emission is derived from the combined set of seven RFAs by interpolating between the individual RFAs. Additionally, the ionization energy required to create these ions from neutral tin is calculated by summing over all charge states z, i.e. $\sum_{z=1} \mathrm{IP}_z N_z$, where IP_z is the total energy needed to ionize from neutral tin to that charge state, and N_z is the total number of ions with that charge state.[77,208] While the ions will have had significantly higher charge states within the plasma, any recombination (dominated by the dielectronic recombination process[238]) within the core of the plasma will emit light and thus will be captured by our photon emission diagnostics. Outside of the center 200 µm of the plasma, the charge state is frozen and thus the ionization energy measured at the RFA in our high-vacuum setup is a metric for the total energy in ionization that has not produced light afterward.[120,214,219,232] Electrons are also emitted by the plasma. However, since the electron and ion (kinetic) temperatures are not so different (nearly thermal) in the plasma,[211] around 30 eV, and the ions are 200.000 times more massive, these do not carry any significant kinetic energy. Finally, the obtained values are divided by the mean laser energy during the measurement. This gives a single value for the energy partitioning, just like for the obtained spectra, making the RFA somewhat more sensitive to long-term drifts in laser energy.

The uncertainty in the values obtained by the RFAs originates from four sources. The first uncertainty is due to the transmission of the gridded RFAs. For each RFA, the geometric transmission [averaging at 0.39(4)] is determined via optical inspection of the alignment of the four grids. In addition to geometric transmission, the transmission of the RFA depends on the retarding field applied[239] and may vary on the order of 10 %. Second, the bottom-up[209] reconstruction method introduces potential errors and necessarily relies on simplifications. Some of the uncertainty caused by the bottom-up method is inherent to the method, such as the fact that the multiple isotopes of tin cannot be separated, which reduces the effective resolution. Furthermore, as can be seen in Fig. 4.3(a), some reconstruction cases deviate from the Faraday Cup-like data (that is, RFA data obtained at 0 V retarding voltage). Such deviations may be explained by drifts in laser energy or small changes in laser-to-droplet alignment, visible from the changing RFA reconstruction for RFAs on different sides of the vacuum chamber. Finally, the interpolation over angle, especially the interpolation below 30°, adds uncertainty to the total error bar for ion energies. In total, a 20 % error bar is used as a conservative estimate for any values determined from the ions.

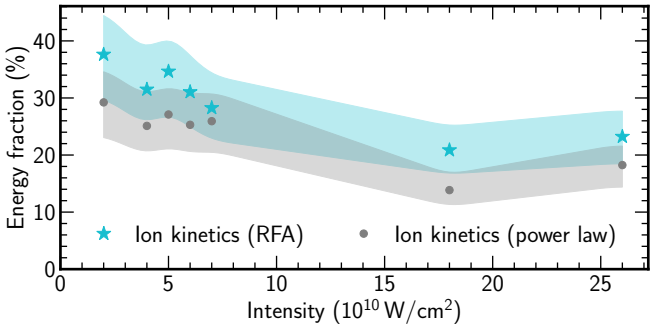

FIGURE 4.7: Reconstructed ion energy fraction into ion kinetics from two methods. First, the method as shown in Fig. 4.3. Second, a method based using the power law scaling (see the main text).

We employ a second method to determine the kinetic energies of the ions to validate the bottom-up RFA reconstruction. This second method is based on a finding by Sheil *et al.*[219] on a power law scaling for the average charge state as a function of kinetic energy $\bar{z}(E)$, independent of the drive laser intensity. The number of ions N at each energy can be calculated by $dN/dE = dQ/(dEe\bar{z}(E))$, where e is the elementary charge. Following Sheil *et al.*,[219] we define $\bar{z}(E) = 0.3E^{0.4}$, resulting in a simple equation $dN/dE = 2.1 \times 10^{19} dQ/dE \times E^{-0.4}$. This equation shows the advantage of the second method: The obtained dN/dE only depends on the dQ/dE measured at 0 V retarding voltage (Faraday Cup-like). Thus, it is not dependent on the bottom-up reconstruction method nor is it impacted by drifts during the 30 minute RFA scan. However, a similar conservative uncertainty of 20 % is still invoked given the common dependence on the RFA transmission function and the uncertainties related to applying the power law. Figure 4.7 compares the ion kinetics as calculated by the RFA method with the $\bar{z}(E)$ power law calculation. The methods show good overall agreement, both qualitatively (showing a decrease over intensity) and quantitatively (in absolute value). The power-law method is consistently slightly below the RFA method, but the difference remains well within the uncertainty estimates.

Neutrals

A fourth diagnostic is spectroscopic shadowgraphic imaging using UV (UV shadowgraphy), which images the tin (before and after the main pulse) at a 90° angle, as can be seen in Fig. 4.5. We use wavelengths around the 284.08 nm $5p^2\ ^3P_2 - 5p6s\ ^3P_2$ neutral tin atomic resonance (cf. Engels *et al.*[76]) which has the highest possible absorption by neutral tin vapor and enables tracking low-density neutrals leaving the plasma in

addition to tracking the liquid before and after the main pulse. The light is generated by a Continuum Horizon OPO and imaged via a single-lens imaging system onto a PCO.ultraviolet camera. Typical velocities of the vapor expansion after laser impact can be observed directly from the shadowgraphy images. This velocity is around 4000 m/s, and the fast neutrals mostly propagate along the laser axis (z). Following Poirier *et al.* who showed that the neutrals balance the momentum carried by ions for pre-pulse cases,[121] we impose that the neutrals post-main pulse should also balance the momentum of the detected ions. Thus, we can combine this momentum obtained with the typical velocity to obtain an estimate of the kinetic energy carried by the neutrals. The results of this method are shown in Fig. 4.4.

Laser energy, reflection & transmission

We use two 2 µm-sensitive high-speed EOT InGaAs ET-5000 photodiodes to measure laser reflection and transmission. A photodiode at 21° measures reflection from the tin disk, while a photodiode at 180° measures transmitted laser light.

The input laser energy is measured by a calibrated power meter for 2 µm laser light. Such devices carry around 5 % calibration uncertainty. The input laser energy measured in the lab is decreased by the transmission of the final window into the vacuum chamber, which is continuously coated with tin and thus varies during the measurement campaign. This decrease in transmission is carefully quantified, and the input laser energy is corrected for it, without additional significant uncertainty. The quality of the top hat spatial profile of the beam ensures that every position in the beam has sufficient intensity to spark plasma and contribute to the plasma and its emission. Thus, we can state that our input laser energy is not a large source of uncertainty in our energy partitioning, except for the aforementioned 5 % uncertainty due to the externally calibrated power meters.

Acknowledgements

This work was conducted at the Advanced Research Center for Nanolithography (ARCNL), a public-private partnership between the University of Amsterdam (UvA), Vrije Universiteit Amsterdam (VU), Rijksuniversiteit Groningen (UG), the Dutch Research Council (NWO), and the semiconductor equipment manufacturer ASML and was partly financed by 'Toeslag voor Topconsortia voor Kennis en Innovatie (TKI)' from the Dutch Ministry of Economic Affairs and Climate Policy and the European Research Council (ERC StG Project no. 802648 and CoG Project no. 101086839). This publication is also a part of the project 'Plasma driven by a variable-wavelength laser for next-generation EUV sources for nanolithography' (with project number

19458) of the Open Technology Programme, which is financed by NWO. The authors thank Stan de Lange and Jorge Gonzalez for valuable discussions and ASML for loaning the Horizon OPO laser system. We would also like to thank Henk-Jan Boluijt and Laurens van Buuren for their work on the experimental setup and Jorijn Kuster for his work on the acquisition software.

Conclusion & Outlook

In the four Chapters of this Thesis, we have seen novel applications of solid-state lasers related to EUV sources, taking inspiration from developments surrounding the EUV lithography machines that are indispensable for our electronic devices. We investigated the vaporization of tin using a solid-state laser by studying the resulting vapor with a novel diagnostic method and by studying the liquid tin during the vaporization process itself. We also analyzed the impact of laser intensity on the vaporization of tin. Finally, we have taken this intensity to the extreme and examined solid-state 2-µm-driven EUV sources. Next, we review the research questions from the Introduction and discuss how each of the chapters has helped answer the questions posed and which questions remain open. Finally, a short Outlook will discuss the possible directions of future research for both UV shadowgraphy and 2 µm-driven EUV sources.

In the Introduction, we asked several questions related to the vaporization of liquid tin using a 1 µm solid-state laser, culminating in the research question: *What sets the composition of a tin vapor created by a laser pulse from a tens of nm-thick liquid tin sheet and which parameters impact this composition?* In **Chapter 1**, we started by introducing the novel 'UV shadowgraphy' diagnostic (later also patented[240]) to measure the composition of the tin vapor, inspired by the rarefication pulse in industrial nanolithography machines. We created tin vapors by vaporizing a 20–50 nm thick tin sheet using a laser pulse with a length of 6 ns and an intensity of 10^8 W/cm^2 and then studied the resulting vapor 100 ns later. We revealed that such a tin vapor consists of small nanoparticles (radius <30 nm) and free atoms with a temperature around 3000 K, near the boiling temperature of tin. Moreover, we found that the vapor is spatially homogeneous; the composition is the same for every position in the vapor, with only the density varying.
To explain what set this composition, we investigated the dynamics of the vaporization in **Chapter 2**. We found that liquid tin sheets gradually thin during the vaporization pulse, with a linear relationship between the thinning rate and the intensity of the vaporization pulse (which is varied between $0.2–4 \times 10^7$ W/cm^2). We developed and introduced a numerical 1D heating and vaporization model to explain our findings. We found excellent agreement between the simulations and the experimental

data, showing that the vaporization of sheets of liquid tin, with a thickness between 30–300 nm, using a laser pulse with an intensity between 0.2–4 $\times 10^7$ W/cm^2 is governed by the Hertz-Knudsen equation. Thus, we can now use scaling laws to predict many aspects of the vaporization. Additionally, because Hertz-Knudsen evaporation results in a vapor of free atoms only, this finding also led to the conclusion that the nanoparticles must be formed after the initial vaporization.
In **Chapter 3**, we found that the key parameter determining the vapor composition is the intensity of the vaporization pulse. We demonstrated this by making a tin sheet with a thickness of 10–25 nm, around half the thickness of the sheet in Chapter 1. The vapors created from such a sheet using a laser intensity below 40 $\times 10^7$ W/cm^2 again show strong spatial homogeneity, a broadband component due to nanoparticles, and free atoms with a temperature around 3000 K. The spectra obtained for these vapors match the spectra from Chapter 1 very well, even though the sheet is thinner. However, when we increase the intensity of the vaporization pulse to exceed the plasma threshold (roughly 20–40 $\times 10^7$ W/cm^2), the composition changes. The homogeneous vapor of nanoparticles and atoms transitions to a atom-only vapor with a temperature of 8000 K (close to the critical temperature of tin) at a vaporization pulse intensity of 130 $\times 10^7$ W/cm^2, showing that the intensity of the vaporization pulse is a key parameter for the resulting vapor. The disappearance of the nanoparticles when plasma forms during the vaporization again hints at a two-stage process in the formation of the nanoparticles: initial vaporization as free atoms followed by clustering, the latter of which seems to be inhibited by the plasma formation.
Taken together, Chapters 1–3 constitute a significant step in understanding the ns-vaporization of tens of nm-thick tin disks. We now know what the composition is of liquid tin vaporized by a solid-state laser, which process governs that vaporization, and also which main parameter impacts the composition. As shown by the patent resulting from the UV shadowgraphy diagnostic, this knowledge has already found application and will continue to contribute to the development of EUV sources such as in the area of the rarefication pulse.

For the highest intensity regime, the EUV-emitting plasmas induced by a 2 µm laser, we formulated a set of different questions in the introduction, resulting in an overarching research question of: *What physics would allow the scaling of 2-µm-driven EUV-emitting plasma sources from laboratory to industrial application?* In recent years, such 2-µm-driven EUV sources have attracted attention as a promising concept in the quest for even more efficient and more powerful EUV sources. This development has been fueled by the rapid development of powerful 2 µm solid-state lasers,[153–155] which promise higher wall-plug efficiency than the current CO_2 laser system. However, more pioneering experiments are required to show that 2 µm-driven EUV sources can also achieve industrially relevant performance levels. That is why,

in another work, we showed that 2-µm-driven EUV sources can reach industrially relevant conversion efficiency (CE) values of ~4.5 % (see List of Publications).[30] (Conversion efficiency, CE, defines the efficiency of creating EUV in the 1 % 'in-band' around 13.5 nm by dividing the total EUV energy by the input laser energy.) To add to this, in **Chapter 4**, we showed that we understand, in detail, where the input laser energy goes in such a plasma, offering a holistic view of the emission of ions, photons, and neutrals. This was achieved by combining a wide range of diagnostics developed over nearly a decade, including UV shadowgraphy. We showed that most of the laser energy, up to 70 %, in a 2-µm-driven EUV-emitting plasma goes to photons. Of these photons, only a small fraction is in-band photons, but a dominant fraction (40 % of the total energy) is in the 13.6–80 nm long out-of-band range. Short out-of-band (5–13.4 nm) photons are also emitted in large amounts, carrying between 5–30 % of all energy depending on the laser intensity. Another large contribution is the emission of ions, which decreases from an initially large 40 % to 25 % of the total energy with increasing laser intensity. We also showed that the ion kinetic energy spectrum from a 2-µm-driven EUV-emitting plasma lacks the characteristic peak seen in 1-µm-driven cases.[209] Vacuum UV (80–130 nm), deep UV (130–265.5 nm), laser reflection, and left-over neutral tin add percentage-level contributions to the power partitioning.
Thus, we have shown that we have a complete overview of what is emitted from a 2-µm-driven plasma and that we have an excellent understanding of such a plasma. We have also studied the ion emission for 2-µm-driven plasmas and shown that 'overheating,' using a laser intensity above the optimal value for CE, is a way to increase total EUV power. Increasing the laser pulse length and overheating would be the primary ways to scale up 2 µm technology to industrial levels by increasing in-band EUV dose per droplet and reducing the ion load. Although this answers our original research question, we have not yet determined what is the best 'target' for 2-µm-driven EUV sources. This will become even more important as the laser energy and pulse length increases, as the sheet targets of Chapter 4 will start to run out of tin, resulting in 'burnthrough.' Thus, more work is needed in this area of research. A small amount of this will be discussed hereafter in the Outlook.

Outlook: what is next for UV shadowgraphy?

This Thesis introduced UV shadowgraphy as a diagnostic for tin vapors, an area of research relevant to the industrial application of the rarefication pulse. We have shown that its current configuration, using the Continuum Horizon OPO laser, which allowed us to scan a wide wavelength range spanning 230–400 nm, is extremely useful as a diagnostic for a wide range of tin vapors. However, the wide scan range of the Horizon OPO comes at the cost of spectral resolution, which is determined by the

$5\,\mathrm{cm}^{-1}$ spectral linewidth of the laser. This spectral linewidth is larger than the width of the atomic resonances, as seen in Chapters 1 and 3. Thus, to study the resonances in more detail, for example, to probe atomic physics or determine absolute densities, a laser with a more narrow spectral width is needed.

A dye laser, a Lioptec Liopstar using Rhodamine 6G in this case, gives the desired narrow spectral width.[241] This dye laser outputs 560–575 nm light when pumped by a 532 nm Nd:YAG laser. By doubling the output green light, we can obtain UV light in between 280–287 nm. Compared to the Horizon OPO, the scan range is significantly reduced; however, the spectral linewidth is also significantly smaller, at $\sim 0.1\,\mathrm{cm}^{-1}$. The dye laser using Rhodamine 6G also fits perfectly into our experimental setup due to its requirement to be pumped with 532 nm light. That is because the Continuum Surelite EX, the pump laser for the Horizon OPO, outputs 355 nm, 532 nm, and 1064 nm, of which the 355 nm and 1064 nm are used to run the Horizon OPO. This leaves the 532 nm light free to pump the dye laser, allowing for 'hot-swapping' between the Horizon OPO and Lioptec dye laser as the backlighting for the UV shadowgraphy diagnostic.

Figure 6(a,b) show a comparison of UV shadowgraphy images, taken with the Horizon OPO (panel a) and the Lioptec dye laser (panel b), both on the $5p^2\,{}^3P_2 - 5p6s\,{}^3P_2$ neutral tin atomic resonance at 284.08 nm. Two differences are immediately clear. First, the dye laser has significantly higher extinction when probing the same target, and thus same density, because of its narrower spectral linewidth, causing all photons to interact with the atomic transition. In comparison, in the OPO case, some photons will have a wavelength that does not match the transition and thus transmit unimpeded. Second, the 'speckle,' a coherent light effect due to the self-interference of the laser light, is stronger for the dye laser, again due to its more narrow spectral width. Since this speckle causes uncertainty in the extinction value (since it changes the 100 % transmission value), this speckle has to be reduced by optimizing the in-coupling optics or averaging it out.

In addition to its higher sensitivity, the dye laser offers two advantages over the OPO due to its ability to study the resonances in more detail: it can be used to obtain absolute densities and it can observe the broadening mechanisms of the resonances, such as temperature-induced Doppler broadening or density-induced collisional broadening.[242] The broadening mechanisms can be observed since the spectral line width of the dye laser is, as we will see, narrower than the width of the underlying cross section σ. The density of the vapor can be directly obtained from the observed extinction when the laser is much narrower than the resonance cross section, which is the case for the dye laser. In this case, we can rewrite the Beer-Lambert law, with

the assumption of monochromatic light

$$E(\nu) = 1 - \exp(-n\sigma(\nu)L), \tag{3}$$

to a value linear with the cross section σ

$$-\ln(1 - E(\nu)) = n\sigma(\nu)L, \tag{4}$$

where n is the density of the absorber, L the path length through the absorber, and $E(\nu)$ the extinction measured at a certain wavelength (or wavenumber ν). The density of the absorber is the gas density n_0 multiplied by the occupation of the state $b(T)$ (which is a temperature-dependent Boltzmann distribution). We can combine this with an expansion of the cross section term to get

$$-\ln(1 - E(\nu)) = n_0 b(T) L \chi(\nu) \sigma_0. \tag{5}$$

Here, $\chi(\nu)$ is the broadening term, normalized and dependent on temperature and density. σ_0 is the known base resonance strength.[77] From this equation, it is also immediately visible that the spectral width of the experimental variable $-\ln(1-E(\nu))$ can now be directly linked to the broadening width $\chi(\nu)$. Since the broadening term $\chi(\nu)$ is normalized, it will drop out when integrating a scan over a complete resonance (but only when the laser linewidth does not play a role). Then, by integrating the experimentally observed value $(-\ln(1 - E(\nu)))$, one can directly obtain a density value if the path length and temperature are known ($\int \chi(\nu) \equiv 1$ and thus drops out)

$$n_0 = \frac{\int -\ln(1 - E(\nu))d\nu}{b(T)L\sigma_0} = \frac{g_k 8\pi\nu^2}{g_i c^2 A_{ki}} \frac{\int -\ln(1 - E(\nu))d\nu}{b(T)L}. \tag{6}$$

Thus, from a single atomic resonance scan with the dye laser, we can obtain the absolute density and the cross section full-width at half-maximum (FWHM) at that density. In addition to this, there are atomic resonances from three different energy levels within the 280–287 nm range, and thus the dye laser could theoretically also be used to obtain a temperature, both by using a Boltzmann plot like the OPO, or by verifying $b(T)$ by ensuring that the densities obtained using Eq. (6) from different transitions match.

In the preliminary experiment that was performed, the results of which are shown in Fig. 6, only the 284.08 nm $5p^2\,{}^3P_2 - 5p6s\,{}^3P_2$ neutral tin atomic resonance was scanned using the dye laser. Similarly to Chapter 1, a line VP was used, in this case a line with a small spatial width of 10 µm, necessitated by the high sensitivity of the dye laser. The UV shadowgraphy imaging technique allows us to probe a wide range of densities from a single vapor by applying Eq. (6) to each pixel. We also

apply a Voigt fit to the data underlying each pixel to obtain Lorentzian broadening (together with Doppler-induced Gaussian broadening, the value of which is fixed by assuming a thermal velocity related to the known 3000 K temperature), which allows us to make a graph of broadening versus density, as can be seen in Fig. 6(b). This curve shows a nearly straight line for an order of magnitude in density. Typical broadening values in the experiment are 0.1–1 cm^{-1}. Here, the lower limit is set by the minimum signal-to-noise ratio of extinction versus speckle required. The lower limit could be decreased by using longer path lengths, which will give more

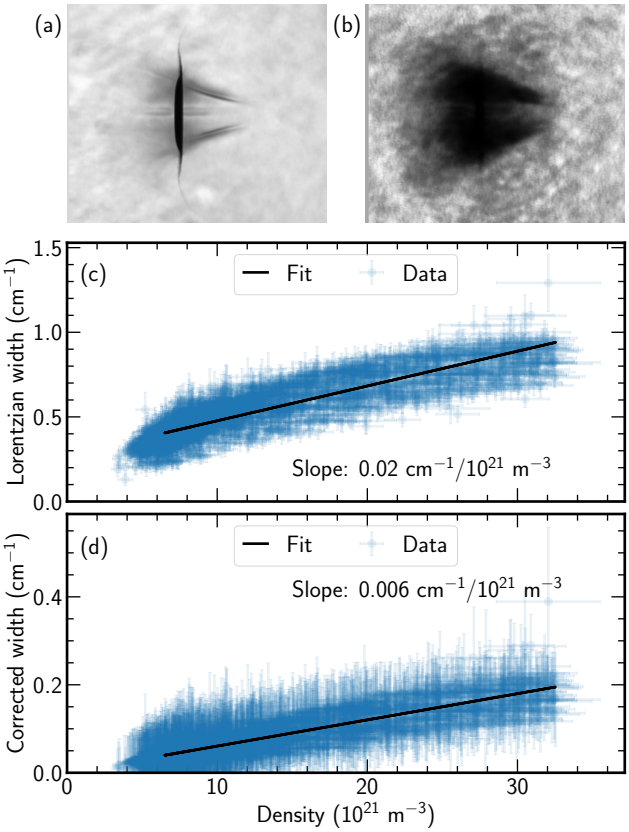

FIGURE 6: Dye-laser-based UV shadowgraphy. Panel (a) shows a OPO-based UV shadowgraphy image, which can be directly compared to the dye-based-based UV shadowgraphy of the same vapor in panel (b). Note the increased absorption in the dye laser case, but also the increased 'speckle' in the background. Panel (c) shows the density and linewidth extraction for the dye laser case for each pixel in the image of panel (b), probing the underlying physics of the atomic resonances. Panel (d) shows the same data but corrected for saturation broadening effects.

extinction at similar densities, and thus at similar broadening values. A straight-line fit results in a broadening of $0.02\,\mathrm{cm}^{-1}$ per $10^{21}\,\mathrm{m}^{-3}$ of atomic density. This behavior of a spectral width that increases linearly with density and the fact that the width is higher than the Doppler broadening ($0.1\,\mathrm{cm}^{-1}$ at 3000 K) confirm that collisional broadening is the main source of broadening in tin vapor such as the one in this experiment.

The straight line fit results in a non-zero y-intercept, which cannot be explained by the collisional broadening alone, especially since we show the Lorentzian width, which is not influenced by the aforementioned Gaussian Doppler component. This can be explained by saturation broadening, which can become an important effect due to the complete spectral overlap of the dye laser with the resonance. In saturation broadening, the excitation rates (from absorption of the laser in the lower state) and deexcitation rates (from relaxation of the upper state) become similar, resulting in broadening because of a reduced amount of atoms available in the lower state to absorb.[242] Whether saturation broadening is important is described by the saturation parameter S

$$S = \frac{2\sigma(\nu)I}{h\nu A_{ki}}, \tag{7}$$

where $\sigma(\nu)$ is the atomic resonance cross section at a specific wavenumber, I the laser intensity, $h\nu$ the photon energy, and A_{ki} the Einstein coefficient of the transition. The spectral width of the resonance will scale up with $\sqrt{1+S}$, so a value of S of at least unity is required for significant increases in the observed line width. The peak value of $\sigma(\nu)$ depends on the density in that location, since additional collisional broadening will reduce the peak value (since $\chi(\nu)$ is normalized). Thus, the S value is different per pixel, but since the intensity of the dye laser pulse in this experiment was $\sim 2 \times 10^3\,\mathrm{W/cm}^2$, it is typically around ~10. Correcting the observed linewidth of saturation broadening results in Fig. 6(c). It is immediately visible that the small deviations from a straight line have been reduced due to the increased effect of saturation broadening on lower density cases. Additionally, the offset at the y-axis intercept has completely disappeared. The straight-line fit of this curve results in a broadening of $0.006\,\mathrm{cm}^{-1}$ per $10^{21}\,\mathrm{m}^{-3}$ of atomic density, roughly three times lower than the uncorrected fit. Considering that self-broadening parameters typically scale with the polarizability of the element,[243] our determined value for tin, between the values for Xe/He/H_2[84] and Na/Cs[244,245] is in line with the literature.[241,246]

With that, this preliminary experiment has shown two things previously unknown when using UV shadowgraphy with Horizon OPO backlighting. First, it has shown that typical densities in our vapor are in $5\text{–}30 \times 10^{21}\,\mathrm{m}^{-3}$. Second, it has shown that the self-broadening parameter for tin-tin collisions in the vapor is the dominant

broadening mechanism, broadening the resonances by 0.006–0.02 cm^{-1} per 10^{21} m^{-3} of atomic density. These broadening parameters are higher than the values used in the model of Chapter 1, which used the order of magnitude lower values for Xe/He/H_2.[84] If correct, the higher broadening parameter would decrease the estimated density of free atoms in Chapter 1 by more than an order of magnitude. However, the central conclusions of Chapter 1, such as the homogeneity of the composition, are independent of this density and remain valid. In conclusion, although these numbers still carry significant uncertainty, due to the saturation broadening effects and the large speckle in the dye laser images (which can be improved as shown in Ref. [241]), this first experiment clearly shows that the dye laser, with its extreme sensitivity, is an excellent tool for future research on absolute densities in the vapor.

Outlook: future research into 2-µm-driven EUV sources

In Chapter 4 and earlier in the Conclusion, we made a case for 2-µm-driven EUV sources as promising candidates for future EUV sources. We showed that competitive CE values can be obtained using a 2 µm main pulse and a pre-deformed target.[30] Furthermore, we showed that we have a detailed understanding of such 2-µm-driven EUV sources, having quantified the full power partitioning. In these works, we also discuss ways to scale up 2-µm-driven sources: by using longer laser pulses, or by using more laser energy, more than the optimum for CE, since the total in-band emissions will continue to increase. In parallel, simulations of 2 µm-driven EUV sources have been performed,[42,45,247] supporting the potential of 2-µm-driven sources. But one question remained open in the Conclusion. What target (droplet, sheet, or vapor) should we use for a 2-µm-driven EUV source with industrially relevant in-band EUV doses per droplet (using long pulses, potentially overheated)?

A concept for 2 µm that has shown promise in simulations[45,247] but has not yet been experimentally investigated is that of a single laser slowly (over >100 ns long) ablating a full droplet without any pre-pulse. As shown in simulations by de Lange *et al.*,[45] such a concept could result in large amount of EUV in-band per pulse, with around 50 mJ in-band EUV being extracted from a 40 µm droplet. An additional advantage would be that this concept using the 2 µm wavelength would not require complex target shaping procedures that are required for the case of 10.6 um CO_2.[42]

Experimentally studying such an alternative concept is challenging, since lasers producing >100 ns long pulses of 2 µm light are not commercially available at the pulse energies required. Still, that does not stop us from testing what happens when we do not use a pre-pulse. So, in an exploratory experiment, we took the pre-pulse and main pulse setup as described in Chapter 4, and simply turned off the pre-pulse.

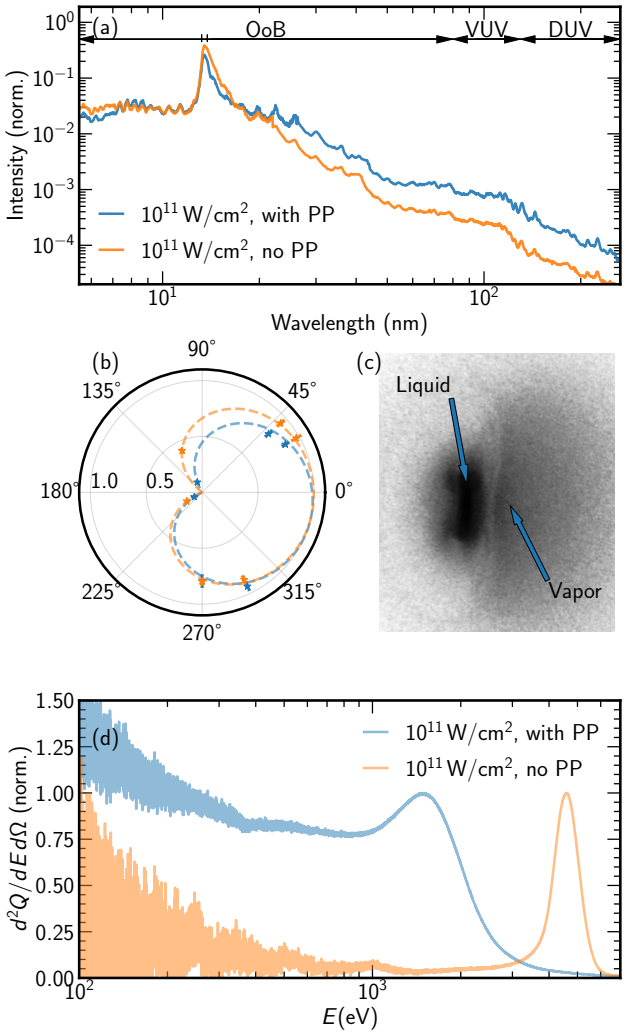

FIGURE 7: Comparison of a 27 ns main pulse with (blue) and without pre-pulse (orange). Panel (a) shows the emission spectrum, normalized to the area under the curve. Panel (b) shows the EUV emission, normalized to the peak. The pre-pulse case emits 3.8 mJ of in-band, for a CE of 3.8 %, while the main pulse only case emits 3.5 mJ of in-band for a CE of 2.4 %. Panel (c) shows a UV shadowgram (using the OPO, at 284.08 nm) of the remaining tin mass in the main pulse only case, which forms a liquid sheet. Panel (d) shows the normalized ion energy spectrum.

C

Figure 7 shows the result of that experiment, compared to a similar case with a pre-pulse. Figure 7(a) shows the plasma emission spectrum between 5–265 nm captured at a 60° angle with respect to the laser. The case without pre-pulse has a higher spectral purity, with more emissions in the in-band 13.5 nm region and less in the long-wavelength vacuum UV (VUV, 80–130 nm) and deep UV (DUV, 130–265 nm) regions. This difference may be contributed to the fact that the droplet is smaller than the laser beam spatial top-hat in the no PP case, while the post-pre-pulse sheet is significantly larger than the laser beam larger. The sheet could allow for larger parts of plasma with a lower temperature, and thus more long-wavelength emission; however, the spectral behavior of the single-pulse case will have to be studied in more detail to prove conclusively. Figure 7(b) shows the EUV emitted at different angles with respect to the laser. It shows how the anisotropic emission is very similar between the sheet and droplet cases.

The total EUV emission for the single-pulse case is 3.5 mJ, for a CE of 2.4 %. Lower, but not far off from the 3.6 % CE with a pre-pulse. Much of this difference can be attributed to the main pulse beam being larger than the droplet and thus exiting the vacuum chamber on the other side without contributing to plasma heating. Furthermore, as the shadowgram in Fig. 7 shows, a significant amount of tin mass is still available at the end of the main pulse, due to its limited 27 ns pulse length. Thus, it is easy to see how the no PP concept could be optimized for large EUV doses above >10 mJ by matching the spatial beam profile to the droplet size and increasing pulse length to use up the available tin mass.

An aspect that changes significantly when the pre-pulse is removed is the energy spectrum of the emitted ions, as shown in Fig. 7(d), detected at an angle of 30° with respect to the laser. Instead of a broadband spectrum with a small hump at 1 keV, a single, large peak at 5 keV forms for the no PP case, increasing the number of high-energy ions compared to that of a pre-pulse case. Simulations[247] also show this peak, hypothesizing that it is caused by the nature of the no PP concept: a long pulse at constant intensity keeps emitting ions at the same kinetic energy. The behavior of this single large peak in the ion energy spectrum deserves more study.

So what is next? Our laser system, previously described by Behnke *et al.*,[51] was historically limited to a pulse length of 27 ns, as is the case for the data shown above. However, through a set of improvements (more uniform seed, higher damage threshold optics), this pulse length has been extended to 37 ns. Additionally, by using both the signal and idler output beams of the laser system and delaying the idler by 37 ns, we have created a 2 µm laser with a pulse length of 74 ns. (The laser system outputs a signal at 2080 nm and idler at 2180 nm to conserve the energy of the 1064 nm pump photons. The signal is typically more well behaved and was historically the only one

used.) Such a laser, with its spatial profile optimized to match the droplet size, should allow for the scaling of EUV in-band per droplet into the >10 mJ regime. However, proving that lies in the future. At that point, we will finally be able to answer the last question we posed related to 2 µm: "What is the best 'target,' such as a sheet or vapor, for 2-µm-driven EUV sources?" Maybe the answer will not be sheet or vapor but rather simply a droplet.

Bibliography

[1] P. Seitz, *Apple stock first to close above $3.5 trillion market cap*, Investor's Business Daily (2024).

[2] C. Oguh, *Microsoft hits $3 trillion market value, second to Apple*, Reuters, Technology (2024).

[3] N. Randewich, *Nvidia surpasses $3.6 trillion market value after Trump win*, Reuters, Technology (2024).

[4] M. Lu, *Ranked: largest semiconductor foundry companies by revenue*, Visual Capitalist (2023).

[5] C. Miller, *Chip war: the fight for the world's most critical technology* (Simon & Schuster UK, 2022).

[6] S. Hung, *Taiwan's silicon shield*, Morgan Stanley Investment Management (2025).

[7] C. Trueman, *TSMC to receive first high NA EUV lithography machine from ASML in Q4*, Data Center Dynamics (2024).

[8] J. Zinkula, *Apple's made-in-the-USA chips signal a turnaround for the US' big semiconductor bet*, Business Insider Nederland (2024).

[9] M. Hijink, *Christophe Fouquet, CEO ASML: 'Je moest eens weten hoeveel fuck-ups er nodig zijn om de meest complexe machine ter wereld te maken'*, NRC (2024).

[10] C. Trueman, *TSMC could account for 24% of Taiwan's electricity consumption by 2030*, Data Center Dynamics (2024).

[11] A. M. Hawryluk and L. G. Seppala, *Soft x-ray projection lithography using an x-ray reduction camera*, J. Vac. Sci. Technol. B: Microelectron. Process. Phenom. **6**, 2162–2166 (1988).

[12] H. Kinoshita, K. Kurihara, Y. Ishii and Y. Torii, *Soft x-ray reduction lithography using multilayer mirrors*, J. Vac. Sci. Technol. B: Microelectron. Process. Phenom. **7**, 1648–1651 (1989).

[13] J. E. Bjorkholm, J. Bokor, L. Eichner, R. R. Freeman, J. Gregus and T. E. Jewell, *Printing of features smaller than 0.1 μm*, J. Vac, Sci, Technol, B **8** (1990).

[14] J. E. Bjorkholm, J. Bokor, L. Eichner, R. R. Freeman, W. M. Mansfield, L. Szeto, D. W. Taylor, D. M. Tennant, O. R. W. Ii, T. E. Jewell, D. L. White, W. K. Waskiewicz, D. L. Windt and A. A. MacDowell, *Soft x-ray projection lithography*, Opt. Photonics News **2**, 27–30 (1991).

[15]B. Wu and A. Kumar, *Extreme ultraviolet lithography: a review*, J. Vac. Sci. Technol. B: Microelectron. Nanom. Struct. Process. Meas. Phenom. **25**, 1743–1761 (2007).

[16]E. Louis, A. E. Yakshin, T. Tsarfati and F. Bijkerk, *Nanometer interface and materials control for multilayer EUV-optical applications*, Prog. Surf. Sci. **86**, 255–294 (2011).

[17]M. D. Ackermann, D. IJpes, A. E. Yakshin, M. J. Sturm and A. Valpreda, *Improving multilayers for maximum reflectivity*, in Opt. EUV Nanolithography XXXVIII, Vol. PC13424 (23 Apr. 2025), PC134240F.

[18]C. Wagner and N. Harned, *Lithography gets extreme*, Nat. Photonics **4**, 24–26 (2010).

[19]E. R. Hosler and O. R. Wood II, *Free-electron lasers: beyond EUV lithography insertion*, in EUV Source Workshop (2017).

[20]J. Y, *EUV lithography. But with a free electron laser*, Asianometry (2024).

[21]B. Jiang, C. Feng, C. Li, Z. Bai, W. Wan, D. Xiang, Q. Gu, K. Wang, Q. Zhang, D. Huang and S. Chen, *A synchrotron-based kilowatt-level radiation source for EUV lithography*, Sci. Rep. **12**, 3325 (2022).

[22]I. J. M. van Elk, C. W. Sweers, D. F. J. Nijhof, R. G. W. van den Berg, T. G. Lucas, X. F. D. Stragier, P. Tack, M. N. Boone, O. J. Luiten and P. H. A. Mutsaers, *First x-rays from a compact and tunable LINAC-based compton scattering source*, (28 Apr. 2025) pre-published.

[23]W. Tian, F. Liang, D. Lu, H. Yu and H. Zhang, *Highly efficient ultraviolet high-harmonic generation from epsilon-near-zero indium tin oxide films*, Photonics Res. **9**, 317–323 (2021).

[24]A. Piel, *Plasma physics: an introduction to laboratory, space, and fusion plasmas*, Graduate Texts in Physics (Springer International Publishing, 2017).

[25]Trumpf, *CO2-lasers | TRUMPF*, CO2-lasers, (2025) https://www.trumpf.com/nl_NL/producten/laser/co2-lasers/ (visited on 07/01/2025).

[26]I. Fomenkov, A. Schafgans and D. Brandt, *Laser-produced plasma sources for high-volume-manufacturing EUV lithography*, Synchrotron Radiat. News **32**, 3–8 (2019).

[27]G. O'Sullivan, B. Li, R. D'Arcy, P. Dunne, P. Hayden, D. Kilbane, T. McCormack, H. Ohashi, F. O'Reilly, P. Sheridan, E. Sokell, C. Suzuki and T. Higashiguchi, *Spectroscopy of highly charged ions and its relevance to EUV and soft x-ray source development*, J. Phys. B: At. Mol. Opt. Phys. **48**, 144025 (2015).

[28]F. Torretti, J. Sheil, R. Schupp, M. M. Basko, M. Bayraktar, R. A. Meijer, S. Witte, W. Ubachs, R. Hoekstra, O. O. Versolato, A. J. Neukirch and J. Colgan, *Prominent radiative contributions from multiply-excited states in laser-produced tin plasma for nanolithography*, Nat. Commun. **11**, 2334 (2020).

B

[29] R. Schupp, L. Behnke, J. Sheil, Z. Bouza, M. Bayraktar, W. Ubachs, R. Hoekstra and O. O. Versolato, *Characterization of 1- and 2-μm-wavelength laser-produced microdroplet-tin plasma for generating extreme-ultraviolet light*, Phys. Rev. Res. **3**, 13294 (2021).

[30] Y. Mostafa, L. Behnke, D. J. Engels, Z. Bouza, J. Sheil, W. Ubachs and O. O. Versolato, *Production of 13.5 nm light with 5% conversion efficiency from 2 μm laser-driven tin microdroplet plasma*, Appl. Phys. Lett. **123**, 234101 (2023).

[31] R. A. Meijer, *Tailored Laser-Droplet Interaction*, PhD thesis (Vrije Universiteit, The Netherlands, Oct. 2021).

[32] K. Hummler, Q. Zhu, K. Behm, L. Matthes, Z. He, O. Biabani, A. LaForge, B. Rollinger, D. Urone, N. Kleemans, M. Jurna, S. McGrogan, P. Mayer, M. Purvis, S. Derks, A. Villalta, A. Govindaraju, Y. Ma and D. Brown, *High-power EUV light sources (>500W) for high throughput in next-generation EUV lithography tools*, in Opt. EUV Nanolithography XXXVII, Vol. 12953 (10 Apr. 2024), pp. 309–316.

[33] Q. Zhu, A. A. Schafgans, J. Stewart, S. Rich, M. Purvis, H. Wang, K. Hummler, A. LaForge, P. Mayer, D. Urone, O. Biabani, A. Dorobantu, Y. Ma and B. Rollinger, *Evolution of EUV light source architecture for continued advancements in EUV high volume manufacturing*, in Opt. EUV Nanolithography XXXVIII, Vol. 13424 (22 Apr. 2025), pp. 363–369.

[34] I. Fomenkov, *EUV source for high volume manufacturing: performance at 250 W and key technologies for power scaling*, in EUV Source Workshop (2017).

[35] I. Fomenkov, D. Brandt, A. Ershov, A. Schafgans, Y. Tao, G. Vaschenko, S. Rokitski, M. Kats, M. Vargas, M. Purvis, R. Rafac, B. La Fontaine, S. De Dea, A. LaForge, J. Stewart, S. Chang, M. Graham, D. Riggs, T. Taylor, M. Abraham and D. Brown, *Light sources for high-volume manufacturing EUV lithography: technology, performance, and power scaling*, Adv. Opt. Technol. **6**, 173–186 (2017).

[36] I. V. Fomenkov, D. C. Brandt, N. R. Farrar, B. L. Fontaine, D. W. Myers, D. J. Brown, A. I. Ershov, N. R. Böwering, D. J. Riggs, R. J. Rafac, S. D. Dea, M. Purvis, R. Peeters, H. Meiling, N. Harned, D. Smith, R. Kazinczi and A. Pirati, *Laser produced plasma light source development for HVM*, in Extreme Ultrav. EUV Lithogr. V, Vol. 9048 (17 Apr. 2014), pp. 755–760.

[37] A. A. Schafgans, D. J. Brown, I. V. Fomenkov, R. Sandstrom, A. Ershov, G. Vaschenko, R. Rafac, M. Purvis, S. Rokitski, Y. Tao, D. J. Riggs, W. J. Dunstan, M. Graham, N. R. Farrar, D. C. Brandt, N. Böwering, A. Pirati, N. Harned, C. Wagner, H. Meiling and R. Kool, *Performance optimization of MOPA pre-pulse LPP light source*, in Extreme Ultrav. EUV Lithogr. VI, Vol. 9422 (16 Mar. 2015), pp. 56–66.

[38]B. Liu, R. A. Meijer, J. Hernandez-Rueda, D. Kurilovich, Z. Mazzotta, S. Witte and O. O. Versolato, *Laser-induced vaporization of a stretching sheet of liquid tin*, J. Appl. Phys. **129**, 53302 (2021).

[39]B. Liu, R. A. Meijer, W. Li, J. Hernandez-Rueda, H. Gelderblom and O. O. Versolato, *Mass partitioning in fragmenting tin sheets*, Phys. Rev. Appl. **20**, 14048 (2023).

[40]K. Nishihara, A. Sunahara, A. Sasaki, M. Nunami, H. Tanuma, S. Fujioka, Y. Shimada, K. Fujima, H. Furukawa, T. Kato, F. Koike, R. More, M. Murakami, T. Nishikawa, V. Zhakhovskii, K. Gamata, A. Takata, H. Ueda, H. Nishimura, Y. Izawa, N. Miyanaga and K. Mima, *Plasma physics and radiation hydrodynamics in developing an extreme ultraviolet light source for lithography*, Phys. Plasmas **15**, 56708 (2008).

[41]K. Umstadter, M. Graham, M. Purvis, A. Schafgans, J. Stewart, P. Mayer and D. Brown, *EUV light source for high-NA and low-NA lithography*, in Opt. EUV Nanolithography XXXVI, Vol. 12494 (28 Apr. 2023), pp. 334–341.

[42]D. J. Hemminga, O. O. Versolato and J. Sheil, *Simulations of plasmas driven by laser wavelengths in the 1.064—10.6 µm range for their characterization as future extreme ultraviolet light sources*, Phys. Plasmas **30**, 33301 (2023).

[43]H. França, H. K. Schubert, O. Versolato and M. Jalaal, *Laser-induced droplet deformation: curvature inversion explained from instantaneous pressure impulse*, (10 Feb. 2025) pre-published.

[44]M. M. Basko, V. G. Novikov and A. S. Grushin, *On the structure of quasi-stationary laser ablation fronts in strongly radiating plasmas*, Phys. Plasmas **22**, 53111 (2015).

[45]S. J. J. de Lange, D. J. Hemminga, Y. Mostafa, R. A. Meijer, O. O. Versolato and J. Sheil, *Modeling the hundreds-of-nanoseconds-long irradiation of tin droplets with a 2 µm-wavelength laser for future EUV lithography*, Plasma Sources Sci. Technol. **33**, 105003 (2024).

[46]D. Kurilovich, *Laser-induced dynamics of liquid tin microdroplets*, PhD thesis (Vrije Universiteit, 2019).

[47]D. Kurilovich, M. M. Basko, D. A. Kim, F. Torretti, R. Schupp, J. C. Visschers, J. Scheers, R. Hoekstra, W. Ubachs and O. O. Versolato, *Power-law scaling of plasma pressure on laser-ablated tin microdroplets*, Phys. Plasmas **25**, 12709 (2018).

[48]R. A. Meijer, D. Kurilovich, K. S. E. Eikema, O. O. Versolato and S. Witte, *The transition from short- to long-timescale pre-pulses: Laser-pulse impact on tin microdroplets*, J. Appl. Phys. **131**, 105905 (2022).

[49]J. Visschers, *Shadowgraphy of Metallic Micro-Droplets in Plasma Sources of Extreme Ultraviolet Light*, MSc thesis (Vrije Universiteit, 22 July 2017).

[50]R. A. Meijer, A. S. Stodolna, K. S. E. Eikema and S. Witte, *High-energy Nd:YAG laser system with arbitrary sub-nanosecond pulse shaping capability*, Opt. Lett. **42**, 2758 (2017).

[51]L. Behnke, E. J. Salumbides, G. Göritz, Y. Mostafa, D. J. Engels, W. Ubachs and O. Versolato, *High-energy parametric oscillator and amplifier pulsed light source at 2-μm*, Opt. Express **31**, 24142–24156 (2023).

[52]KSTAR Team, G. S. Yun, W. Lee, M. J. Choi, J. Lee, H. K. Park, B. Tobias, C. W. Domier, N. C. Luhmann, A. J. H. Donné and J. H. Lee, *Two-dimensional visualization of growth and burst of the edge-localized filaments in KSTAR H-mode plasmas*, Phys. Rev. Lett. **107**, 45004 (2011).

[53]A. Perek, W. A. J. Vijvers, Y. Andrebe, I. G. J. Classen, B. P. Duval, C. Galperti, J. R. Harrison, B. L. Linehan, T. Ravensbergen, K. Verhaegh, M. R. de Baar, Tcv and EUROfusion MST1 Teams, *MANTIS: a real-time quantitative multispectral imaging system for fusion plasmas*, Rev. Sci. Instrum. **90**, 123514 (2019).

[54]K. Verhaegh, B. Lipschultz, J. R. Harrison, N. Osborne, A. C. Williams, P. Ryan, J. S. Allcock, J. G. Clark, F. Federici, B. Kool, T. Wijkamp, A. Fil, D. Moulton, O. Myatra, A. Thornton, T. O. S. J. Bosman, C. Bowman, G. Cunningham, B. P. Duval, S. Henderson, R. Scannell and t. M. U. Team, *Spectroscopic investigations of detachment on the MAST upgrade super-X divertor*, Nucl. Fusion **63**, 16014 (2022).

[55]T. A. Wijkamp, J. S. Allcock, X. Feng, B. Kool, B. Lipschultz, K. Verhaegh, B. P. Duval, J. R. Harrison, L. Kogan, N. Lonigro, A. Perek, P. Ryan, R. M. Sharples, I. G. J. Classen, R. J. E. Jaspers and t. M. U. Team, *Characterisation of detachment in the MAST-U super-X divertor using multi-wavelength imaging of 2D atomic and molecular emission processes*, Nucl. Fusion **63**, 56003 (2023).

[56]J. Scheers, R. Schupp, R. Meijer, W. Ubachs, R. Hoekstra and O. O. Versolato, *Time- and space-resolved optical Stark spectroscopy in the afterglow of laser-produced tin-droplet plasma*, Phys. Rev. E **102**, 13204 (2020).

[57]V. Motto-Ros, Q. L. Ma, S. Grégoire, W. Q. Lei, X. C. Wang, F. Pelascini, F. Surma, V. Detalle and J. Yu, *Dual-wavelength differential spectroscopic imaging for diagnostics of laser-induced plasma*, Spectrochim. Acta, Part B, 6th Euro-Mediterranean Symposium on Laser Induced Breakdown Spectroscopy (EMSLIBS 2011) **74–75**, 11–17 (2012).

[58]H. J. van der Meiden, J. W. M. Vernimmen, K. Bystrov, K. Jesko, M. Y. Kantor, G. De Temmerman and T. W. Morgan, *Collective Thomson scattering system for determination of ion properties in a high flux plasma beam*, Appl. Phys. Lett. **109**, 261102 (2016).

[59]V. N. Ochkin, S. Y. Savinov, S. N. Tskhai, U. Czarnetzki, V. S. von der Gathen and H. F. Dobele, *Nonlinear optical techniques for plasma diagnostics*, IEEE Trans. Plasma Sci. **26**, 1502–1513 (1998).

[60] S. Hassaballa, M. Yakushiji, Y.-K. Kim, K. Tomita, K. Uchino and K. Muraoka, *Two-dimensional structure of PDP micro-discharge plasmas obtained using laser Thomson scattering*, IEEE Trans. Plasma Sci. **32**, 127–134 (2004).

[61] K. Tomita, Y. Sato, S. Tsukiyama, T. Eguchi, K. Uchino, K. Kouge, H. Tomuro, T. Yanagida, Y. Wada, M. Kunishima, G. Soumagne, T. Kodama, H. Mizoguchi, A. Sunahara and K. Nishihara, *Time-resolved two-dimensional profiles of electron density and temperature of laser-produced tin plasmas for extreme-ultraviolet lithography light sources*, Sci. Rep. **7**, 12328 (2017).

[62] K. Sakai, S. Isayama, N. Bolouki, M. S. Habibi, Y. L. Liu, Y. H. Hsieh, H. H. Chu, J. Wang, S. H. Chen, T. Morita, K. Tomita, R. Yamazaki, Y. Sakawa, S. Matsukiyo and Y. Kuramitsu, *Collective Thomson scattering in non-equilibrium laser produced two-stream plasmas*, Phys. Plasmas **27**, 103104 (2020).

[63] H. Mizoguchi, H. Nakarai, T. Abe, K. M. Nowak, Y. Kawasuji, H. Tanaka, Y. Watanabe, T. Hori, T. Kodama, Y. Shiraishi, T. Yanagida, G. Soumagne, T. Yamada, T. Yamazaki, S. Okazaki and T. Saitou, *Performance of 100-W HVM LPP-EUV source*, Adv. Opt. Technol. **4**, 297–309 (2015).

[64] O. O. Versolato, *Physics of laser-driven tin plasma sources of EUV radiation for nanolithography*, Plasma Sources Sci. Technol. **28**, 83001 (2019).

[65] T. W. Morgan, P. Rindt, G. G. van Eden, V. Kvon, M. A. Jaworksi and N. J. Lopes Cardozo, *Liquid metals as a divertor plasma-facing material explored using the pilot-PSI and magnum-PSI linear devices*, Plasma Phys. Controlled Fusion **60**, 14025 (2017).

[66] S. Roccella, G. Dose, R. de Luca, M. Iafrati, A. Mancini and G. Mazzitelli, *CPS based liquid metal divertor target for EU-DEMO*, J. Fusion Energy 2020 39:6 **39**, 462–468 (2020).

[67] P. Rindt, J. L. van den Eijnden, T. W. Morgan and N. J. Lopes Cardozo, *Conceptual design of a liquid-metal divertor for the European DEMO*, Fusion Eng. Des. **173**, 112812 (2021).

[68] J. R. Freeman, S. S. Harilal and A. Hassanein, *Enhancements of extreme ultraviolet emission using prepulsed Sn laser-produced plasmas for advanced lithography applications*, J. Appl. Phys. **110**, 83303 (2011).

[69] T. Cummins, C. O'Gorman, P. Dunne, E. Sokell, G. O'Sullivan and P. Hayden, *Colliding laser-produced plasmas as targets for laser-generated extreme ultraviolet sources*, Appl. Phys. Lett. **105**, 44101 (2014).

[70] D. Kurilovich, A. L. Klein, F. Torretti, A. Lassise, R. Hoekstra, W. Ubachs, H. Gelderblom and O. O. Versolato, *Plasma propulsion of a metallic microdroplet and its deformation upon laser impact*, Phys. Rev. Appl. **6**, 14018 (2016).

[71] B. Liu, D. Kurilovich, H. Gelderblom and O. O. Versolato, *Mass loss from a stretching semitransparent sheet of liquid tin*, Phys. Rev. Appl. **13**, 24035 (2020).

[72]H. Gelderblom, H. Lhuissier, A. L. Klein, W. Bouwhuis, D. Lohse, E. Villermaux and J. H. Snoeijer, *Drop deformation by laser-pulse impact*, J. Fluid Mech. **794**, 676–699 (2016).

[73]C. F. Bohren and D. R. Huffman, *Absorption and scattering of light by small particles* (Wiley, Weinheim, 1983).

[74]R. M. Drake and J. E. Gordon, *Mie scattering*, Am. J. Phys. **53**, 955–962 (1985).

[75]A. Lehr, F. Rivic, M. Jäger, M. Gleditzsch and R. Schäfer, *Optical absorption and shape transition in neutral Sn N clusters with $N \leq 40$: a photodissociation spectroscopy and electric beam deflection study*, Phys. Chem. Chem. Phys. **24**, 11616–11635 (2022).

[76]D. J. Engels, R. A. Meijer, H. K. Schubert, W. J. van der Zande, W. Ubachs and O. O. Versolato, *High-resolution spectroscopic imaging of atoms and nanoparticles in thin film vaporization*, Appl. Phys. Lett. **123**, 254102 (2023).

[77]A. Kramida, Yu. Ralchenko, J. Reader and NIST ASD Team, *NIST Atomic Spectra Database*, National Institute of Standards and Technology, Gaithersburg, MD., (2020) https://www.nist.gov/pml/atomic-spectra-database (visited on 06/10/2021).

[78]R. C. Hilborn, *Einstein coefficients, cross sections, f-values, dipole moments, and all that*, Am. J. Phys. **50**, 982–986 (1982).

[79]C. J. Foot, *Atomic physics*, Oxford Master Series in Physics 7. Atomic, Optical, and laser physics (Oxford University Press, Oxford ; New York, 2005), 331 pp.

[80]J. A. Aguilera and C. Aragón, *Characterization of a laser-induced plasma by spatially resolved spectroscopy of neutral atom and ion emissions: comparison of local and spatially integrated measurements*, Spectrochim. Acta, Part B **59**, 1861–1876 (2004).

[81]J. Lambert, *Photometria sive de mensura et gradibus luminis, colorum et umbrae* (Eberhardt Klett, 1760).

[82]A. Beer, *Bestimmung der Absorption des rothen Lichts in farbigen Flüssigkeiten*, Ann. Phys. **162**, 78–88 (1852).

[83]R. Schupp, F. Torretti, R. A. Meijer, M. Bayraktar, J. Sheil, J. Scheers, D. Kurilovich, A. Bayerle, A. A. Schafgans and M. Purvis, *Radiation transport and scaling of optical depth in Nd:YAG laser-produced microdroplet-tin plasma*, Appl. Phys. Lett. **115**, 124101 (2019).

[84]M. V. Romalis, E. Miron and G. D. Cates, *Pressure broadening of Rb D_1 and D_2 lines by ^{3}He, ^{4}He, N_2, and Xe: Line cores and near wings*, Physical Review A **56**, 4569 (1997).

[85]S. Prahl, *Miepython: pure Python calculation of Mie scattering*, Zenodo, 10.5281/zenodo.15514362 (2023).

[86]B. J. Sumlin, W. R. Heinson and R. K. Chakrabarty, *Retrieving the aerosol complex refractive index using PyMieScatt: a mie computational package with visualization capabilities*, J. Quant. Spectrosc. Radiat. Transfer **205**, 127–134 (2018).
[87]R. Kofman, P. Cheyssac and R. Garrigos, *From the bulk to clusters: solid-liquid phase transitions and precursor effects*, Phase Transitions **24–26**, 283–342 (1990).
[88]A. Lehr, M. Jäger and R. Schäfer, *Optical properties of Si n+(n = 6-100) clusters: the approach to bulk behavior*, J. Phys. Chem. C **124**, 1070–1076 (2020).
[89]G. Cisneros, J. S. Helman and C. N. J. Wagner, *Dielectric function of liquid tin between 250 and 1100°C*, Phys. Rev. B **25**, 4248 (1982).
[90]P. Drude, *Zur elektronentheorie der metalle*, Ann. Phys. **306**, 566–613 (1900).
[91]H. R. Griem, *Principles of plasma spectroscopy*, Cambridge Monographs on Plasma Physics (Cambridge University Press, Cambridge, 1997).
[92]M. M. Martynyuk, *Critical constant of metals*, Russ, J. Phys, Chem, **57**, 494 (1983).
[93]A. Miotello and R. Kelly, *Critical assessment of thermal models for laser sputtering at high fluences*, Appl. Phys. Lett. **67**, 3535–3537 (1995).
[94]R. Kelly and A. Miotello, *Comments on explosive mechanisms of laser sputtering*, Appl. Surf. Sci. **96–98**, 205–215 (1996).
[95]A. Miotello and R. Kelly, *Laser-induced phase explosion: new physical problems when a condensed phase approaches the thermodynamic critical temperature*, Appl. Phys. A **69**, S67–S73 (1999).
[96]N. M. Bulgakova and A. V. Bulgakov, *Pulsed laser ablation of solids: transition from normal vaporization to phase explosion*, Appl. Phys. A **73**, 199–208 (2001).
[97]A. H. A. Lutey, *An improved model for nanosecond pulsed laser ablation of metals*, J. Appl. Phys. **114**, 83108 (2013).
[98]J. Safarian and T. A. Engh, *Vacuum evaporation of pure metals*, Metall. Mater. Trans. **44**, 747–753 (2013).
[99]D. R. Stull, *Vapor pressure of pure substances. Organic and inorganic compounds*, Ind, Eng, Chem **39**, 517–540 (1947).
[100]J. A. Cahill, G. M. Krieg and A. V. Grosse, *Electrical conductivity of tin, lead, and bismuth near their boiling points with estimates to their critical temperatures*, J. Chem. Eng. Data **13**, 504–507 (1968).
[101]D. A. Young and B. J. Alder, *Critical point of metals from the van der Waals model*, Phys. Rev. A **3**, 364–371 (1971).
[102]C. Liang, Y. Shimizu, T. Sasaki and N. Koshizaki, *Synthesis of ultrafine SnO_2-x nanocrystals by pulsed laser-induced reactive quenching in liquid medium*, J. Phys. Chem. B **107**, 9220–9225 (2003).
[103]S. Amoruso, G. Ausanio, R. Bruzzese, M. Vitiello and X. Wang, *Femtosecond laser pulse irradiation of solid targets as a general route to nanoparticle formation in a vacuum*, Phys. Rev. B **71**, 33406 (2005).

[104] P. T. Murray and E. Shin, *Formation of silver nanoparticles by through thin film ablation*, Mater. Lett. **62**, 4336–4338 (2008).
[105] J. C. Alonso, R. Diamant, P. Castillo, M. C. Acosta–García, N. Batina and E. Haro-Poniatowski, *Thin films of silver nanoparticles deposited in vacuum by pulsed laser ablation using a YAG:Nd laser*, Appl. Surf. Sci. **255**, 4933–4937 (2009).
[106] A. Mazzi, F. Gorrini and A. Miotello, *Liquid nanodroplet formation through phase explosion mechanism in laser-irradiated metal targets*, Phys. Rev. E **92**, 31301 (2015).
[107] A. Mazzi and A. Miotello, *Simulation of phase explosion in the nanosecond laser ablation of aluminum*, J. Colloid Interface Sci., Laser Synthesis **489**, 126–130 (2017).
[108] A. Mazzi, F. Gorrini and A. Miotello, *Dynamics of liquid nanodroplet formation in nanosecond laser ablation of metals*, Appl. Surf. Sci. **418**, 601–606 (2017).
[109] D. Hudgins, N. Gambino, B. Rollinger and R. Abhari, *Neutral cluster debris dynamics in droplet-based laser-produced plasma sources*, J. Phys. D: Appl. Phys. **49**, 185205 (2016).
[110] A. L. Klein, W. Bouwhuis, C. W. Visser, H. Lhuissier, C. Sun, J. H. Snoeijer, E. Villermaux, D. Lohse and H. Gelderblom, *Drop shaping by laser-pulse impact*, Phys. Rev. Appl. **3**, 44018 (2015).
[111] K. Tomita, Y. Pan, A. Sunahara, K. Kouge, H. Mizoguchi and K. Nishihara, *Observation of plasma inflows in laser-produced Sn plasma and their contribution to extreme-ultraviolet light output enhancement*, Sci. Rep. **13**, 1825 (2023).
[112] E. Villermaux and B. Bossa, *Drop fragmentation on impact*, J. Fluid Mech. **668**, 412–435 (2011).
[113] A. L. Klein, D. Kurilovich, H. Lhuissier, O. O. Versolato, D. Lohse, E. Villermaux and H. Gelderblom, *Drop fragmentation by laser-pulse impact*, J. Fluid Mech. **893**, 7 (2020).
[114] Y. Wang and L. Bourouiba, *Non-galilean taylor–culick law governs sheet dynamics in unsteady fragmentation*, J. Fluid Mech. **969**, A19 (2023).
[115] C. Vernay, L. Ramos and C. Ligoure, *Free radially expanding liquid sheet in air: time- and space-resolved measurement of the thickness field*, J. Fluid Mech. **764**, 428–444 (2015).
[116] S. J. Byrnes, *Multilayer optical calculations*, ArXiv, 10.48550/arXiv.1603.02720 (2020).
[117] J. A. Stratton, *Electromagnetic theory*, 2nd ed. (McGraw-Hill, 1941).
[118] J. S. Chickos and W. E. Acree, *NIST chemistry WebBook, NIST standard reference database number 69*, (2022) https://webbook.nist.gov/cgi/inchi?ID=C7440315 (visited on 08/11/2023).

[119]I. V. Savchenko, S. V. Stankus and A. Sh. Agadjanov, *Measurement of liquid tin heat transfer coefficients within the temperature range of 506–1170 K*, High Temp. **49**, 506–511 (2011).

[120]D. J. Hemminga, L. Poirier, M. M. Basko, R. Hoekstra, W. Ubachs, O. O. Versolato and J. Sheil, *High-energy ions from Nd:YAG laser ablation of tin microdroplets: comparison between experiment and a single-fluid hydrodynamic model*, Plasma Sources Sci. Technol. **30**, 105006 (2021).

[121]L. Poirier, D. J. Hemminga, A. Lassise, L. Assink, R. Hoekstra, J. Sheil and O. O. Versolato, *Strongly anisotropic ion emission in the expansion of Nd:YAG-laser-produced plasma*, Phys. Plasmas **29**, 123102 (2022).

[122]M. Haddadi. M, B. Das, J. Jeong, S. Kim and D.-S. Kim, *Near-maximum microwave absorption in a thin metal film at the pseudo-free-standing limit*, Sci. Rep. **12**, 18386 (2022).

[123]Y. Wang and L. Bourouiba, *Drop impact on small surfaces: thickness and velocity profiles of the expanding sheet in the air*, J. Fluid Mech. **814**, 510–534 (2017).

[124]M. M. Stevanović, *Thermodynamic characterization of vaporization of the fourth group elements*, Int. J. Thermophys. **4**, 353–362 (1983).

[125]M. J. Assael, A. Chatzimichailidis, K. D. Antoniadis, W. A. Wakeham, M. L. Huber and H. Fukuyama, *Reference correlations for the thermal conductivity of liquid copper, gallium, indium, iron, lead, nickel and tin*, High Temp.-High Pressures **46**, 391–416 (2017).

[126]M. Assael, A. Kalyva, K. Antoniadis, R. Banish, I. Egry, J. Wu, E. Kaschnitz and W. Wakeham, *Reference data for the density and viscosity of liquid copper and liquid tin*, J. Phys. Chem. Ref. Data **39**, 331051–331058 (2010).

[127]H. Heffan, *Heat capacity of liquid tin* (University of California, Berkeley, 1958).

[128]A. V. Khvan, T. Babkina, A. T. Dinsdale, I. A. Uspenskaya, I. V. Fartushna, A. I. Druzhinina, A. B. Syzdykova, M. P. Belov and I. A. Abrikosov, *Thermodynamic properties of tin: part I experimental investigation, ab-initio modelling of α-, β-phase and a thermodynamic description for pure metal in solid and liquid state from 0 K*, Calphad **65**, 50–72 (2019).

[129]H.-U. Krebs, M. Weisheit, J. Faupel, E. Süske, T. Scharf, C. Fuhse, M. Störmer, K. Sturm, M. Seibt, H. Kijewski, D. Nelke, E. Panchenko and M. Buback, *Pulsed laser deposition (PLD) – a versatile thin film technique*, in *Advances in Solid State Physics*, Vol. 43, edited by B. Kramer and B. Kramer (Springer Berlin Heidelberg, Berlin, Heidelberg, July 2003), pp. 505–518.

[130]S. M. Rossnagel, *Thin film deposition with physical vapor deposition and related technologies*, J. Vac. Sci. Technol., A **21**, S74–S87 (2003).

[131]H. B. Profijt, S. E. Potts, M. C. M. Van De Sanden and W. M. M. Kessels, *Plasma-assisted atomic layer deposition: basics, opportunities, and challenges*, J. Vac. Sci. Technol., A **29**, 50801 (2011).

[132]G. G. Van Eden, T. W. Morgan, D. U. B. Aussems, M. A. Van Den Berg, K. Bystrov and M. C. M. Van De Sanden, *Self-regulated plasma heat flux mitigation due to liquid Sn vapor shielding*, Phys. Rev. Lett. **116**, 135002 (2016).

[133]G. G. Van Eden, V. Kvon, M. C. M. Van De Sanden and T. W. Morgan, *Oscillatory vapour shielding of liquid metal walls in nuclear fusion devices*, Nat. Commun. **8**, 192 (2017).

[134]H. Mizoguchi, H. Nakarai, T. Abe, K. M. Nowak, Y. Kawasuji, H. Tanaka, Y. Watanabe, T. Hori, T. Kodama, Y. Shiraishi, T. Yanagida, G. Soumagne, T. Yamada, T. Yamazaki and T. Saitou, *High power LPP-EUV source with long collector mirror lifetime for high volume semiconductor manufacturing*, in 2018 China Semicond. Technol. Int. Conf. CSTIC (Mar. 2018), pp. 1–7.

[135]D. Hudgins and R. S. Abhari, *Rupture time of droplets impacted by a burst of picosecond laser pulses*, Phys. Rev. E **99**, 31102 (2019).

[136]A. Hassanein, T. Sizyuk, V. Sizyuk and S. S. Harilal, *Combined effects of pre-pulsing and target geometry on efficient extreme ultraviolet production from laser produced plasma experiments and modeling*, J. Micro/ Nanolithogr. MEMS MOEMS **10**, 33002–33002 (2011).

[137]S. Yu. Grigoryev, B. V. Lakatosh, M. S. Krivokorytov, V. V. Zhakhovsky, S. A. Dyachkov, D. K. Ilnitsky, K. P. Migdal, N. A. Inogamov, A. Yu. Vinokhodov, V. O. Kompanets, Yu. V. Sidelnikov, V. M. Krivtsun, K. N. Koshelev and V. V. Medvedev, *Expansion and fragmentation of a liquid-metal droplet by a short laser pulse*, Phys. Rev. Appl. **10**, 64009 (2018).

[138]P. Koukouvinis, N. Kyriazis and M. Gavaises, *Smoothed particle hydrodynamics simulation of a laser pulse impact onto a liquid metal droplet*, PLOS One **13**, edited by E. Gutheil, e0204125 (2018).

[139]V. Sizyuk, T. Sizyuk and A. Hassanein, *Temporal pre-pulse shaping in dual pulse laser produced plasma for the optimization of the EUV source in tin microdroplet system*, J. Appl. Phys. **135**, 93101 (2024).

[140]H.-J. Kunze, *Introduction to plasma spectroscopy*, Vol. 56 (Springer Science & Business Media, 2009).

[141]H. K. Schubert, D. J. Engels, R. A. Meijer, B. Liu and O. O. Versolato, *Scaling relations in laser-induced vaporization of thin free-flying liquid metal sheets*, Phys. Rev. Res. **6**, 023182 (2024).

[142]K. Kouge, S. Nagai, T. Hori, Y. Ueno, T. Yanagida, K. Miyao, H. Hayashi, Y. Watanabe, T. Abe, H. Nakarai, T. Saito and H. Mizoguchi, *Update of development progress of the high power LPP-EUV light source using a magnetic field*, J. Photopolym. Sci. Technol. **33**, 37–44 (2020).

[143]Y. Nishimura, Y. Ueno, S. Nagai, F. Iwamoto, K. Miyao, H. Hayashi, Y. Watanabe, T. Abe, H. Nakarai and H. Mizoguchi, *Key technology development progress of*

the high power LPP-EUV light source, in Opt. EUV Nanolithography XXXV, Vol. 12051 (26 May 2022), pp. 241–255.

[144]M. M. Waldrop, *The chips are down for Moore's law*, Nature News, News Feature, 144 (2016).

[145]M. A. van de Kerkhof, F. Liu, M. Meeuwissen, X. Zhang, M. Bayraktar, R. C. de Kruif and N. V. Davydova, *High-power EUV lithography: spectral purity and imaging performance*, J. Micro/Nanolithogr. MEMS MOEMS **19**, 33801 (2020).

[146]J. van Schoot, K. Troost, F. Bornebroek, R. van Ballegoij, S. Lok, P. Krabbendam, J. Stoeldraijer, J. Benschop, J. Finders and H. Meiling, *The future of EUV lithography: continuing Moore's law into the next decade*, in Extreme Ultrav. EUV Lithogr. IX, Vol. 10583 (2018), 105830R.

[147]O. O. Versolato, J. Sheil, S. Witte, W. Ubachs and R. Hoekstra, *Microdroplet-tin plasma sources of EUV radiation driven by solid-state-lasers (topical review)*, J. Opt. **24**, 54014 (2022).

[148]A. Sasaki, A. Sunahara, H. Furukawa, K. Nishihara, S. Fujioka, T. Nishikawa, F. Koike, H. Ohashi and H. Tanuma, *Modeling of radiative properties of Sn plasmas for extreme-ultraviolet source*, J. Appl. Phys. **107**, 113303 (2010).

[149]Q. Huang, V. Medvedev, R. van de Kruijs, A. Yakshin, E. Louis and F. Bijkerk, *Spectral tailoring of nanoscale EUV and soft x-ray multilayer optics*, Appl. Phys. Rev. **4**, 11104 (2017).

[150]L. Behnke, R. Schupp, Z. Bouza, M. Bayraktar, Z. Mazzotta, R. Meijer, J. Sheil, S. Witte, W. Ubachs, R. Hoekstra and O. O. Versolato, *Extreme ultraviolet light from a tin plasma driven by a 2-µm-wavelength laser*, Opt. Express **29**, 4475–4487 (2021).

[151]R. Schupp, L. Behnke, Z. Bouza, Z. Mazzotta, Y. Mostafa, A. Lassise, L. Poirier, J. Sheil, M. Bayraktar, W. Ubachs, R. Hoekstra and O. O. Versolato, *Characterization of angularly resolved EUV emission from 2-µm-wavelength laser-driven Sn plasmas using preformed liquid disk targets*, J. Phys. D: Appl. Phys. **54**, 365103 (2021).

[152]Z. Y. Shi, Y. Yuan, W. P. Wang, Y. Y. Ma, X. Y. Sun, N. Lin and Y. X. Leng, *Enhanced extreme ultraviolet conversion efficiency of a 2 µm laser-driven preformed tin-droplet target using short picosecond pre-pulses*, Phys. Plasmas **30**, 43107 (2023).

[153]I. Tamer, B. A. Reagan, T. Galvin, J. Galbraith, E. Sistrunk, A. Church, G. Huete, H. Neurath and T. Spinka, *Demonstration of a compact, multi-Joule, diode-pumped Tm:YLF laser*, Opt. Lett. **46**, 5096 (2021).

[154]I. Tamer, B. A. Reagan, T. Galvin, F. Batysta, E. Sistrunk, D. Willard, A. Church, H. Neurath, J. Galbraith, G. Huete and T. Spinka, *1 GW peak power and 100 J pulsed operation of a diode-pumped Tm:YLF laser*, Opt. Express **30**, 46336–46343 (2022).

[155]I. Tamer, Z. Hubka, L. Kiani, J. Owens, A. Church, F. Batysta, T. Galvin, D. Willard, A. Yandow, J. Galbraith, D. Alessi, C. Harthcock, B. Hickman, C. Jackson, J. Nissen, S. Tardiff, H. Nguyen, E. Sistrunk, T. Spinka and B. A. Reagan, *Demonstration of a 1 TW peak power, joule-level ultrashort Tm:YLF laser*, Opt. Lett. **49**, 1583–1586 (2024).

[156]Y. Mostafa, L. Behnke, D. J. Engels, Z. Bouza, J. Sheil, W. Ubachs and O. O. Versolato, *Erratum: "Production of 13.5 nm light with 5% conversion efficiency from 2 μm laser-driven tin microdroplet plasma" [Appl. Phys. Lett. 23, 234101 (2023)]*, Appl. Phys. Lett. **126**, 49901 (2025).

[157]Y. Yuan, Y. Y. Ma, W. P. Wang, S. J. Chen, Y. Cui, M. Zi, X. H. Yang, G. B. Zhang and Y. X. Leng, *Enhancing the conversion efficiency of extreme ultraviolet light sources using a 2 μm wavelength laser*, Plasma Phys. Controlled Fusion **64**, 25001 (2021).

[158]S. Fujioka, H. Nishimura, K. Nishihara, A. Sasaki, A. Sunahara, T. Okuno, N. Ueda, T. Ando, Y. Tao, Y. Shimada, K. Hashimoto, M. Yamaura, K. Shigemori, M. Nakai, K. Nagai, T. Norimatsu, T. Nishikawa, N. Miyanaga, Y. Izawa and K. Mima, *Opacity effect on extreme ultraviolet radiation from laser-produced tin plasmas*, Phys. Rev. Lett. **95**, 235004 (2005).

[159]Y. Shimada, H. Nishimura, M. Nakai, K. Hashimoto, M. Yamaura, Y. Tao, K. Shigemori, T. Okuno, K. Nishihara, T. Kawamura, A. Sunahara, T. Nishikawa, A. Sasaki, K. Nagai, T. Norimatsu, S. Fujioka, S. Uchida, N. Miyanaga, Y. Izawa and C. Yamanaka, *Characterization of extreme ultraviolet emission from laser-produced spherical tin plasma generated with multiple laser beams*, Appl. Phys. Lett. **86**, 51501 (2005).

[160]T. Ando, S. Fujioka, H. Nishimura, N. Ueda, Y. Yasuda, K. Nagai, T. Norimatsu, M. Murakami, K. Nishihara, N. Miyanaga, Y. Izawa, K. Mima and A. Sunahara, *Optimum laser pulse duration for efficient extreme ultraviolet light generation from laser-produced tin plasmas*, Appl. Phys. Lett. **89**, 151501 (2006).

[161]T. Higashiguchi, N. Dojyo, M. Hamada, W. Sasaki and S. Kubodera, *Low-debris, efficient laser-produced plasma extreme ultraviolet source by use of a regenerative liquid microjet target containing tin dioxide (SnO_2) nanoparticles*, Appl. Phys. Lett. **88**, 201503 (2006).

[162]S. Fujioka, M. Shimomura, Y. Shimada, S. Maeda, H. Sakaguchi, Y. Nakai, T. Aota, H. Nishimura, N. Ozaki, A. Sunahara, K. Nishihara, N. Miyanaga, Y. Izawa and K. Mima, *Pure-tin microdroplets irradiated with double laser pulses for efficient and minimum-mass extreme-ultraviolet light source production*, Appl. Phys. Lett. **92**, 241502 (2008).

[163]O. Morris, F. O'Reilly, P. Dunne and P. Hayden, *Angular emission and self-absorption studies of a tin laser produced plasma extreme ultraviolet source between 10 and 18nm*, Appl. Phys. Lett. **92**, 231503 (2008).

[164]D. Nakamura, T. Akiyama, K. Okazaki, K. Tamaru, A. Takahashi and T. Okada, *Ablation dynamics of tin micro-droplet irradiated by double pulse laser used for extreme ultraviolet lithography source*, J. Phys. D: Appl. Phys. **41**, 245210 (2008).

[165]K. L. Sequoia, Y. Tao, S. Yuspeh, R. Burdt and M. S. Tillack, *Two dimensional expansion effects on angular distribution of 13.5nm in-band extreme ultraviolet emission from laser-produced Sn plasma*, Appl. Phys. Lett. **92**, 221505 (2008).

[166]J. R. Freeman, S. S. Harilal, B. Verhoff, A. Hassanein and B. Rice, *Laser wavelength dependence on angular emission dynamics of Nd:YAG laser-produced Sn plasmas*, Plasma Sources Sci. Technol. **21**, 55003 (2012).

[167]A. Z. Giovannini and R. S. Abhari, *Three-dimensional extreme ultraviolet emission from a droplet-based laser-produced plasma*, J. Appl. Phys. **114**, 33303 (2013).

[168]A. Z. Giovannini and R. S. Abhari, *Effects of the dynamics of droplet-based laser-produced plasma on angular extreme ultraviolet emission profile*, Appl. Phys. Lett. **104**, 194104 (2014).

[169]H. Chen, X. Wang, L. Duan, H. Lan, Z. Chen, D. Zuo and P. Lu, *Angular distribution of ions and extreme ultraviolet emission in laser-produced tin droplet plasma*, J. Appl. Phys. **117**, 193302 (2015).

[170]H. Matsukuma, A. Sunahara, T. Yanagida, H. Tomuro, K. Kouge, T. Kodama, T. Hosoda, S. Fujioka and H. Nishimura, *Correlation between laser absorption and radiation conversion efficiency in laser produced tin plasma*, Appl. Phys. Lett. **107**, 121103 (2015).

[171]R. Schupp, F. Torretti, R. A. Meijer, M. Bayraktar, J. Scheers, D. Kurilovich, A. Bayerle, K. S. E. Eikema, S. Witte, W. Ubachs, R. Hoekstra and O. O. Versolato, *Efficient generation of extreme ultraviolet light from Nd:YAG-driven microdroplet-tin plasma*, Physical Review Applied **12**, 014010 (2019).

[172]M. Brandstätter, M. M. Weber and R. S. Abhari, *Non-axisymmetric droplet irradiation effects on ion and extreme ultraviolet light emission of laser-produced plasma light sources*, J. Appl. Phys. **129**, 233306 (2021).

[173]A. Sunahara, A. Hassanein, K. Tomita, S. Namba and T. Higashiguchi, *Optimization of extreme ultra-violet light emitted from the CO_2 laser-irradiated tin plasmas using 2D radiation hydrodynamic simulations*, Opt. Express **31**, 31780–31795 (2023).

[174]T. Sugiura, H. Yazawa, H. Morita, K. Sakaue, D. Nakamura, E. J. Takahashi, A. Sunahara, G. O'Sullivan, S. Namba and T. Higashiguchi, *Efficient extreme ultraviolet emission by multiple laser pulses*, Appl. Phys. Lett. **125**, 34103 (2024).

[175]Y. Wu, X. Wang, T. Ray, Y. C. F. Thio and A. Hassanein, *Experimental study of the dynamics and extreme ultraviolet radiation of laser produced colliding Sn plasmas*, Phys. Plasmas **31**, 43508 (2024).

[176]T. Wang, Z. Hu, L. He, N. Lin, Y. Leng and W. Chen, *Characterization of optical depth for laser produced plasma extreme ultraviolet source*, Vacuum **231**, 113805 (2025).

[177]V. I. Azarov and Y. N. Joshi, *Analysis of the $4d^7$-$4d^6$ 5p transition array of the eighth spectrum of tin: Sn VIII*, J. Phys. B: At. Mol. Opt. Phys. **26**, 3495 (1993).

[178]W. Svendsen and G. O'Sullivan, *Statistics and characteristics of XUV transition arrays from laser-produced plasmas of the elements tin through iodine*, Phys. Rev. A **50**, 3710–3718 (1994).

[179]S. S. Churilov and A. N. Ryabtsev, *Analyses of the Sn IX–Sn XII spectra in the EUV region*, Phys. Scr. **73**, 614 (2006).

[180]S. S. Churilov and A. N. Ryabtsev, *Analysis of the spectra of In XII–XIV and Sn XIII–XV in the far-VUV region*, Opt. Spectrosc. **101**, 169–178 (2006).

[181]S. S. Churilov and A. N. Ryabtsev, *Analysis of the $4p^64d^7$-$(4p^64d^64f + 4p^54d^8)$ transitions in the Sn VIII spectrum*, Opt. Spectrosc. **100**, 660–666 (2006).

[182]A. N. Ryabtsev, É. Ya. Kononov and S. S. Churilov, *Spectra of rubidium-like Pd X-Sn XIV ions*, Opt. Spectrosc. **105**, 844–850 (2008).

[183]R. D'Arcy, H. Ohashi, S. Suda, H. Tanuma, S. Fujioka, H. Nishimura, K. Nishihara, C. Suzuki, T. Kato, F. Koike, J. White and G. O'Sullivan, *Transitions and the effects of configuration interaction in the spectra of Sn XV–Sn XVIII*, Phys. Rev. A **79**, 42509 (2009).

[184]H. Ohashi, S. Suda, H. Tanuma, S. Fujioka, H. Nishimura, A. Sasaki and K. Nishihara, *EUV emission spectra in collisions of multiply charged Sn ions with He and Xe*, J. Phys. B: At. Mol. Opt. Phys. **43**, 65204 (2010).

[185]A. Windberger, F. Torretti, A. Borschevsky, A. Ryabtsev, S. Dobrodey, H. Bekker, E. Eliav, U. Kaldor, W. Ubachs, R. Hoekstra, J. R. Crespo López-Urrutia and O. O. Versolato, *Analysis of the fine structure of Sn^{11+} – Sn^{14+} ions by optical spectroscopy in an electron-beam ion trap*, Phys. Rev. A **94**, 12506 (2016).

[186]J. Colgan, D. P. Kilcrease, J. Abdallah, M. E. Sherrill, C. J. Fontes, P. Hakel and G. S. J. Armstrong, *Atomic structure considerations for the low-temperature opacity of Sn*, High Energy Density Phys. **23**, 133–137 (2017).

[187]F. Torretti, A. Windberger, A. Ryabtsev, S. Dobrodey, H. Bekker, W. Ubachs, R. Hoekstra, E. V. Kahl, J. C. Berengut, J. R. C. López-Urrutia and O. O. Versolato, *Optical spectroscopy of complex open-4d-shell ions Sn^{7+} – Sn^{10+}*, Phys. Rev. A **95**, 42503 (2017).

[188]F. Torretti, R. Schupp, D. Kurilovich, A. Bayerle, J. Scheers, W. Ubachs, R. Hoekstra and O. O. Versolato, *Short-wavelength out-of-band EUV emission from Sn laser-produced plasma*, J. Phys. B: At. Mol. Opt. Phys. **51**, 045005 (2018).

[189]F. Torretti, F. Liu, M. Bayraktar, J. Scheers, Z. Bouza, W. Ubachs, R. Hoekstra and O. Versolato, *Spectral characterization of an industrial EUV light source for nanolithography*, J. Phys. D: Appl. Phys. **53**, 55204 (2019).

[190]J. Scheers, C. Shah, A. Ryabtsev, H. Bekker, F. Torretti, J. Sheil, D. A. Czapski, J. C. Berengut, W. Ubachs, J. R. Crespo López-Urrutia, R. Hoekstra and O. O. Versolato, *EUV spectroscopy of highly charged Sn^{13+} - Sn^{15+} ions in an electron-beam ion trap*, Phys. Rev. A **101**, 062511 (2020).

[191]Z. Bouza, J. Scheers, A. Ryabtsev, R. Schupp, L. Behnke, C. Shah, J. Sheil, M. Bayraktar, J. R. Crespo López-Urrutia, W. Ubachs, R. Hoekstra and O. O. Versolato, *EUV spectroscopy of Sn^{5+}–Sn^{10+} ions in an electron beam ion trap and laser-produced plasmas*, J. Phys. B: At. Mol. Opt. Phys. **53**, 195001 (2020).

[192]S. Namba, S. Fujioka, H. Sakaguchi, H. Nishimura, Y. Yasuda, K. Nagai, N. Miyanaga, Y. Izawa, K. Mima, K. Sato and K. Takiyama, *Characterization of out-of-band radiation and plasma parameters in laser-produced Sn plasmas for extreme ultraviolet lithography light sources*, J. Appl. Phys. **104**, 13305 (2008).

[193]H. Sakaguchi, S. Fujioka, S. Namba, H. Tanuma, H. Ohashi, S. Suda, M. Shimomura, Y. Nakai, Y. Kimura, Y. Yasuda, H. Nishimura, T. Norimatsu, A. Sunahara, K. Nishihara, N. Miyanaga, Y. Izawa and K. Mima, *Absolute evaluation of out-of-band radiation from laser-produced tin plasmas for extreme ultraviolet lithography*, Appl. Phys. Lett. **92**, 111503 (2008).

[194]D. Campos, S. S. Harilal and A. Hassanein, *The effect of laser wavelength on emission and particle dynamics of Sn plasma*, J. Appl. Phys. **108**, 113305 (2010).

[195]N. Gambino, B. Rollinger, D. Hudgins and R. S. Abhari, *Spectral emission properties of a laser-produced plasma light source in the sub-200 nm range for wafer inspection applications*, J. Micro/Nanolithogr. MEMS MOEMS **14**, 34002 (2015).

[196]N. Gambino, B. Rollinger, M. Brandstätter and R. S. Abhari, *Vacuum ultraviolet spectral emission properties of Ga, In and Sn droplet-based laser produced plasmas*, Spectrochim. Acta, Part B **122**, 149–156 (2016).

[197]H. Parchamy, J. Szilagyi, M. Masnavi and M. Richardson, *Ultraviolet out-of-band radiation studies in laser tin plasma sources*, J. Appl. Phys. **122**, 173303 (2017).

[198]Z. Bouza, J. Byers, J. Scheers, R. Schupp, Y. Mostafa, L. Behnke, Z. Mazzotta, J. Sheil, W. Ubachs, R. Hoekstra, M. Bayraktar and O. O. Versolato, *The spectrum of a 1-µm-wavelength-driven tin microdroplet laser-produced plasma source in the 5.5–265.5 nm wavelength range*, AIP Adv. **11**, 125003 (2021).

[199]Y. Pan, K. Tomita, A. Sunahara, A. Sasaki and K. Nishihara, *Joint measurement of electron density, temperature, and emission spectrum of Nd:YAG laser-produced tin plasma*, Appl. Phys. Lett. **123**, 204103 (2023).

[200]M. Murakami, Y.-G. Kang, K. Nishihara, S. Fujioka and H. Nishimura, *Ion energy spectrum of expanding laser-plasma with limited mass*, Phys. Plasmas **12**, 62706 (2005).

[201]O. Morris, P. Hayden, P. Dunne, F. O'Reilly, G. O'Sullivan, E. Sokell, E. L. Antonsen, S. N. Srivastava, K. C. Thompson and D. N. Ruzic, *Determination*

of charge state, energy and angular distributions of tin ions emitted from laser produced plasma based EUV sources, J. Phys. Conf. Ser. **58**, 391 (2007).

[202] A. O'Connor, O. Morris and E. Sokell, *Angular and energy distribution of Sn ion debris ejected from a laser-produced plasma source, for laser power densities in the range suitable for extreme ultraviolet lithography*, J. Appl. Phys. **109**, 73301 (2011).

[203] A. Z. Giovannini, N. Gambino, B. Rollinger and R. S. Abhari, *Angular ion species distribution in droplet-based laser-produced plasmas*, J. Appl. Phys. **117**, 33302 (2015).

[204] Z. Chen, X. Wang, D. Zuo and J. Wang, *Investigation of ion characteristics in CO_2 laser irradiating preformed tin-droplet plasma*, Laser Part. Beams **34**, 552–561 (2016).

[205] M. J. Deuzeman, A. S. Stodolna, E. E. B. Leerssen, A. Antoncecchi, N. Spook, T. Kleijntjens, J. Versluis, S. Witte, K. S. E. Eikema, W. Ubachs, R. Hoekstra and O. O. Versolato, *Ion distribution and ablation depth measurements of a fs-ps laser-irradiated solid tin target*, J. Appl. Phys. **121**, 103301 (2017).

[206] A. Bayerle, M. J. Deuzeman, S. van der Heijden, D. Kurilovich, T. d. F. Pinto, A. Stodolna, S. Witte, K. S. E. Eikema, W. Ubachs, R. Hoekstra and O. O. Versolato, *Sn ion energy distributions of ns- and ps-laser produced plasmas*, Plasma Sources Sci. Technol. **27**, 045001 (2018).

[207] M. Brandstätter, N. Gambino and R. S. Abhari, *Temporally and spatially resolved ion dynamics of droplet-based laser-produced tin plasmas in lateral expansion direction*, J. Appl. Phys. **123**, 43308 (2018).

[208] L. Poirier, A. Bayerle, A. Lassise, F. Torretti, R. Schupp, L. Behnke, Y. Mostafa, W. Ubachs, O. O. Versolato and R. Hoekstra, *Cross-calibration of a combined electrostatic and time-of-flight analyzer for energy- and charge-state-resolved spectrometry of tin laser-produced plasma*, Appl. Phys. B **128**, 39 (2022).

[209] L. Poirier, A. Lassise, Y. Mostafa, L. Behnke, N. Braaksma, L. Assink, R. Hoekstra and O. O. Versolato, *Energy- and charge-state-resolved spectrometry of tin laser-produced plasma using a retarding field energy analyzer*, Appl. Phys. B **128**, 135 (2022).

[210] L. Poirier, A. Lassise, R. Hoekstra, J. Sheil and O. O. Versolato, *Dependence of ion charge-energy emission from Nd:YAG-laser-produced plasma on laser intensity in the 0.4–40×10^{10} W/cm^2 range*, Phys. Plasmas **30**, 83505 (2023).

[211] S. R. Totorica, K. Lezhnin, D. J. Hemminga, J. Gonzalez, J. Sheil, A. Diallo, A. Hyder and W. Fox, *Acceleration mechanisms of energetic ion debris in laser-driven tin plasma EUV sources*, Appl. Phys. Lett. **124**, 174101 (2024).

[212] S. Fujioka, H. Nishimura, K. Nishihara, M. Murakami, Y.-G. Kang, Q. Gu, K. Nagai, T. Norimatsu, N. Miyanaga, Y. Izawa, K. Mima, Y. Shimada, A. Sunahara

and H. Furukawa, *Properties of ion debris emitted from laser-produced mass-limited tin plasmas for extreme ultraviolet light source applications*, Appl. Phys. Lett. **87**, 241503 (2005).

[213] D. Nakamura, K. Tamaru, Y. Hashimoto, T. Okada, H. Tanaka and A. Takahashi, *Mitigation of fast ions generated from laser-produced Sn plasma for extreme ultraviolet light source by H_2 gas*, J. Appl. Phys. **102**, 123310 (2007).

[214] R. A. Burdt, Y. Ueno, Y. Tao, S. Yuspeh, M. S. Tillack and F. Najmabadi, *Recombination effects during expansion into vacuum in laser produced Sn plasma*, Appl. Phys. Lett. **97**, 41502 (2010).

[215] D. B. Abramenko, M. V. Spiridonov, P. V. Krainov, V. M. Krivtsun, D. I. Astakhov, V. V. Medvedev, M. van Kampen, D. Smeets and K. N. Koshelev, *Measurements of hydrogen gas stopping efficiency for tin ions from laser-produced plasma*, Appl. Phys. Lett. **112**, 164102 (2018).

[216] S. Rai, K. I. Bijlsma, I. Rabadán, L. Méndez, P. A. J. Wolff, M. Salverda, O. O. Versolato and R. Hoekstra, *Charge exchange in collisions of 1–100-keV Sn^{3+} ions with H_2 and D_2*, Phys. Rev. A **106**, 12804 (2022).

[217] S. Rai, K. I. Bijlsma, L. Poirier, E. De Wit, L. Assink, A. Lassise, I. Rabadán, L. Méndez, J. Sheil and O. O. Versolato, *Evidence of production of keV Sn^+ ions in the H_2 buffer gas surrounding an Sn-plasma EUV source*, Plasma Sources Sci. Technol. **32**, 35006 (2023).

[218] K. Bijlsma, L. Oltra, E. de Wit, L. Assink, I. Rabadán, L. Méndez and R. Hoekstra, *Electron Capture from Molecular Hydrogen by Metastable Sn^{2+*} Ions*, Atoms **12**, 9 (2024).

[219] J. Sheil, L. Poirier, A. C. Lassise, D. J. Hemminga, S. Schouwenaars, N. Braaksma, A. Frenzel, R. Hoekstra and O. O. Versolato, *Power-law scaling relating the average charge state and kinetic energy in expanding laser-driven plasmas*, Phys. Rev. Lett. **133**, 125101 (2024).

[220] L. Oltra, L. Méndez, I. Rabadán, K. Bijlsma, E. de Wit and R. Hoekstra, *Sequential Synchronous Mechanism for Double-Electron Capture: Insights into Unforeseen Large Cross Sections in Low-Energy Sn^{3+} + H_2 Collisions*, Phys. Rev. Lett. **134**, 93002 (2025).

[221] K. Liu, Y. Li, F. Zhang and M. Fan, *Transient thermal and structural deformation and its impact on optical performance of projection optics for extreme ultraviolet lithography*, Jpn. J. Appl. Phys. **46**, 6568 (2007).

[222] G. Yang and Y. Li, *Analysis and control of thermal and structural deformation of projection optics for 22-nm EUV lithography*, in Extreme Ultrav. EUV Lithogr. III, Vol. 8322 (23 Mar. 2012), pp. 830–839.

[223] A. N. Heays, A. D. Bosman and E. F. van Dishoeck, *Photodissociation and photoionisation of atoms and molecules of astrophysical interest*, Astron. Astrophys. **602**, A105 (2017).

[224]R. M. van der Horst, J. Beckers, E. A. Osorio, D. I. Astakhov, W. J. Goedheer, C. J. Lee, V. V. Ivanov, V. M. Krivtsum, K. N. Koshelev, D. V. Lopaev, F. Bijkerk and V. Y. Banine, *Exploring the electron density in plasma induced by EUV radiation: I. Experimental study in hydrogen*, J. Phys. D: Appl. Phys. **49**, 145203 (2016).

[225]J. Sheil, O. Versolato, V. Bakshi and H. Scott, *Review of the 1st EUV light sources code comparison workshop*, Atoms **11**, 130 (2023).

[226]D. Colombant and G. F. Tonon, *X-ray emission in laser-produced plasmas*, J. Appl. Phys. **44**, 3524–3537 (1973).

[227]H. Kawasaki, A. Sunahara, Y. Shimada, T. Ejima, W. Jiang, G. O'Sullivan, M. Nishikino, S. Namba and T. Higashiguchi, *Electron temperature and soft x-ray intensity scaling in laser heavy element plasma interaction*, AIP Adv. **10**, 65306 (2020).

[228]R. A. Wilhelm, M. J. Deuzeman, S. Rai, W. Husinsky, P. S. Szabo, H. Biber, R. Stadlmayr, C. Cupak, J. Hundsbichler, C. Lemell, W. Möller, A. Mutzke, G. Hobler, O. O. Versolato, F. Aumayr and R. Hoekstra, *On the missing single collision peak in low energy heavy ion scattering*, Nucl. Instrum. Methods Phys. Res. B: Beam Interact. Mater. At. **544**, 165123 (2023).

[229]M. Murakami and M. M. Basko, *Self-similar expansion of finite-size non-quasi-neutral plasmas into vacuum: relation to the problem of ion acceleration*, Phys. Plasmas **13**, 12105 (2006).

[230]F. Dahmani and T. Kerdja, *Measurements and laser-wavelength dependence of mass-ablation rate and ablation pressure in planar layered targets*, Laser Part. Beams **9**, 769–778 (1991).

[231]R. A. Burdt, S. Yuspeh, K. L. Sequoia, Y. Tao, M. S. Tillack and F. Najmabadi, *Experimental scaling law for mass ablation rate from a Sn plasma generated by a 1064 nm laser*, J. Appl. Phys. **106**, 33310 (2009).

[232]I. V. Roudskoy, *General features of highly charged ion generation in laser-produced plasmas*, Laser Part. Beams **14**, 369–384 (1996).

[233]B. O'Shay, F. Najmabadi, S. S. Harilal and M. S. Tillack, *Nanosecond spectroscopy of expanding laser-produced tin plasma*, J. Phys. Conf. Ser. **59**, 773 (2007).

[234]M. S. Tillack, K. L. Sequoia and Y. Tao, *Geometric effects on EUV emissions in spherical and planar targets*, J. Phys. Conf. Ser. **112**, 42060 (2008).

[235]T. Sizyuk and A. Hassanein, *Tuning laser wavelength and pulse duration to improve the conversion efficiency and performance of EUV sources for nanolithography*, Phys. Plasmas **27**, 103507 (2020).

[236]M. M. Basko, *On the maximum conversion efficiency into the 13.5-nm extreme ultraviolet emission under a steady-state laser ablation of tin microspheres*, Phys. Plasmas **23**, 83114 (2016).

[237]H.-K. Chung, M. H. Chen, W. L. Morgan, Y. Ralchenko and R. W. Lee, *FLYCHK: generalized population kinetics and spectral model for rapid spectroscopic analysis for all elements*, High Energy Density Phys. **1**, 3–12 (2005).

[238]N. R. Badnell, A. Foster, D. C. Griffin, D. Kilbane, M. O'Mullane and H. P. Summers, *Dielectronic recombination of heavy species: the tin $4p^6 4d^q$ - $4p^6 4d^{(q-1)} 4f$ + $4p^5 4d^{(q+1)}$ transition arrays for q = 1–10*, J. Phys. B: At. Mol. Opt. Phys. **44**, 135201 (2011).

[239]L. Assink, In preparation (2025).

[240]D. J. Engels, H. K. Schubert, R. A. Meijer, F. J. Hernandez-Rueda, W. J. van der Zande and O. O. Versolato, *Multi-wavelength shadowgraphy for an EUV radiation source*, WO2023237313A1 (Dec. 2023).

[241]L. I. de Reus, *Investigating tin vapor broadening and shifting mechanisms for gas parameter extraction using UV shadowgraphy*, MSc thesis (Eindhoven TU, The Netherlands, 9 Apr. 2025).

[242]W. Demtröder, *Laser Spectroscopy 1: Basic principles*, Vol. 9783642538599 (Springer-Verlag Berlin Heidelberg, 1 Nov. 2014), 1-496.

[243]L. Weller, R. J. Bettles, P. Siddons, C. S. Adams and I. G. Hughes, *Absolute absorption on the rubidium D_1 line including resonant dipole–dipole interactions*, J. Phys. B: At. Mol. Opt. Phys. **44**, 195006 (2011).

[244]J. Huennekens and A. Gallagher, *Self-broadening of the sodium resonance lines and excitation transfer between the $3P_{3/2}$ and $3P_{1/2}$ levels*, Phys. Rev. A **27**, 1851–1864 (1983).

[245]Z. J. Jabbour, J. Sagle, R. K. Namiotka and J. Huennekens, *Measurement of the self-broadening rate coefficients of the cesium resonance lines*, J. Quant. Spectrosc. Radiat. Transfer **54**, 767–778 (1995).

[246]D. R. Lide, *CRC handbook of chemistry and physics: a ready-reference book of chemical and physical data* (CRC press, 1995).

[247]S. J. J. de Lange, J. Gonzalez, D. J. Engels, F. M. Kohlmeier and J. Sheil, *Ion emission properties from tin plasmas generated by 2 μm-wavelength laser pulses*, (2025) pre-published.

Samenvatting

Onze afhankelijkheid van druppels tin

In EUV nanolithografie machines worden 50.000 druppels tin per seconde opgeblazen, elk uur van elke dag. Waarom is dat zo? Wat is een EUV nanolithografie machine eigenlijk? Hoezo zouden we allemaal afhankelijk zijn van deze machines? In dit hoofdstuk leg ik uit wat deze EUV nanolithografie machines precies doen en waarom ze zo belangrijk zijn. Ook zal ik uitleggen hoe mijn proefschrift daarbij aansluit, inclusief een korte beschrijving van de belangrijkste resultaten in mijn jaren bij ARCNL.

In totaal komen er in een EUV nanolithografie machine 1,6 biljoen druppels per jaar tot hun eind*. Bij elke explosie van een tin druppel komt er een klein beetje licht vrij, en niet zomaar licht, maar extreem ultraviolet (EUV) licht. Dit EUV licht wordt in de machine gebruikt om computerchips te 'printen'.

Computerchips zitten tegenwoordig niet alleen maar in computers, maar ze zijn overal te vinden. Zo zitten ze in je vaatwassen, stofzuiger, auto, maar ook in je telefoon, tablet, TV en natuurlijk in alle servers die je niet ziet maar nodig zijn voor YouTube, Instagram, Google, ChatGPT of de 'cloud'. Om deze producten te verbeteren is er een continue vraag naar snellere en betere chips. Het is dus niet gek dat sommige van de meest waardevolle bedrijven werken aan computerchips.[1–3]

Laten we in wat meer detail kijken naar de chipindustrie voordat we in detail gaan over hoe één chip gemaakt wordt. In de chipindustrie zijn extreem bekende bedrijven actief, zoals Microsoft en Apple, die producten maken voor consumenten met gebruik van computerchips. Andere voorbeelden in dit veld zijn 'tech' bedrijven zoals Google, Meta (Facebook), of OpenAI (van ChatGPT). Maar ook bedrijven zoals BMW, NXP, Bosch of Texas Instruments (van de rekenmachines) zijn significante gebruikers van computerchips. Al deze bedrijven staan onderaan de piramide van de chipindustrie, zoals te zien in Figuur 1: zij maken producten *met* computerchips.

*1,6 biljoen druppels zijn er heel veel, maar de druppels zijn zo klein dat het maar net boven 100 kg aan tin is.

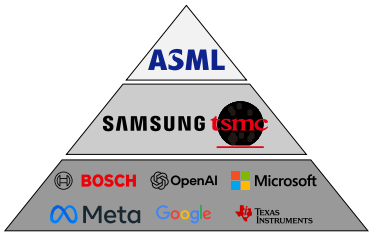

FIGUUR 1: De piramide van (een sector van) de chipindustrie. Hoewel er veel bedrijven zijn die computerchips gebruiken of ontwerpen, zijn er maar een paar die de capaciteiten hebben om ze te maken (de middelste laag, de 'foundries'), en nog minder die de benodigde machines ('tools') kunnen maken. Als we focussen op één zo'n tool, de nanolithografie machine, dan staat ASML alleen aan de top van de piramide.

Het daadwerkelijk maken van computerchips wordt gedaan door een selecte groep bedrijven genaamd 'foundries' wegens de complexiteit en kosten hiervan. De grootste foundry is TSMC.[4] TSMC maakt bijvoorbeeld de chips van Apple en controleert ongeveer 60 % van de gehele markt.[8] TSMC is niet heel bekend, maar toch extreem belangrijk. Zo belangrijk dat het regelmatig genoemd wordt als het gaat over de autonomie van Taiwan.[5,6] Om de schaal van dit bedrijf te schetsen: TSMC gebruikt 8 % van *alle* elektriciteit in Taiwan, een getal wat verwacht wordt te stijgen naar 20 % in 2030.[7]

Hoewel er maar een paar bedrijven zijn die moderne chips kunnen maken op een grote schaal, zijn er nog minder bedrijven die de machines, 'tools,' kunnen maken die hiervoor nodig zijn. Eén van de machines die je nodig hebt om chips te maken is een nanolithografie machine*. De nanolithografie machine is belangrijk omdat deze niet alleen de duurste machine is die je nodig hebt, maar ook de machine is die bepaalt hoe klein je kunt 'printen' op de chip, wat bepalend is voor hoe efficiënt en snel die chips zullen zijn. Tijdens zijn productieproces gaat één chip talloze keren door lithografie machines, maar ook door veel andere machines. Maar aangezien dit proefschrift te maken heeft met nanolithografie, laten we deze andere complexiteiten even buiten beschouwing†. Kort samengevat: nanolithografie machines zijn onmisbaar voor computerchips, die weer onmisbaar zijn voor vele aspecten van onze levens. En hoewel de oudere nanolithografie machines op verschillende plekken te krijgen zijn, is de nieuwste generatie, die met tin druppels werkt, alleen te krijgen bij één bedrijf: ASML.

S

Een korte geschiedenis van 's werelds meest complexe machine

Moderne lithografie machines zijn complexe machines, zo groot als een klein huis, en kosten meer dan 200 miljoen euro per stuk.[10] Ze zijn, volgens ASML zelf,[9] de meest complexe machines in de wereld. Het gehele proces om een chip te 'printen' is uitermate complex en bevat veel scheikunde, natuurkunde en complexe technologie,

*Ook wel eens 'gewoon' lithografie machine. De 'nano' wordt toegevoegd om de schaal, in de nanometers, een miljardste van een meter, aan te geven.

†Zo zijn er nog allerlei andere onderdelen van de chipindustrie waar je een 'piramide' voor zou kunnen tekenen, zoals bedrijven gerelateerd aan het extreem pure silicium dat je nodig hebt als grondstof, de machines die je nodig hebt om je chip te meten en testen, of andere stappen in dit proces zoals etsen.

maar voor dit proefschrift focussen we op een deel van de machine: de lichtbron. De naam zegt het al: in dit deel van de machine wordt het licht gegenereerd dat in de rest van de machine gebruikt wordt voor het printen.

Je kunt je wel voorstellen dat dit geen simpel lampje is. Voor lithografie moet je uitermate veel controle hebben over je licht, omdat je natuurlijk precies het patroon wilt kunnen printen dat gevraagd wordt door de klant. Als je dat niet doet, werkt de chip misschien niet, en dat kost geld. Daarom wil je bijvoorbeeld nauwbandig licht hebben, licht van één kleur, zoals een laser pointer. Als je meerdere kleuren hebt, dan zul je een vervagend effect krijgen, en zullen minder van je chips het goed doen.

De vorige generatie machines gebruikte een laser die licht genereerde met een kleur diep in het UV (λ=193 nm). Maar dat was niet meer goed genoeg voor de meest complexe moderne chips; er moesten kleinere kenmerken op de chips zodat ze nog sneller konden worden. Deze eis wordt beschreven door een van de fundamentele limieten van de optica, het Abbe limiet:

$$\mathrm{CD} = k_1 \frac{\lambda}{\mathrm{NA}}. \tag{8}$$

Het Abbe limiet zegt dat de kritische dimensie (CD, van het Engelse 'critical dimension'), oftewel het kleinste kenmerk dat je kan maken, afhangt van drie dingen: λ, de golflengte (kleur) van het licht waarmee je werkt, de parameter k_1, die afhankelijk is van allerlei procesoptimalisaties, en de numerieke apertuur (NA) van het systeem. De numerieke apertuur kan voorgesteld worden als een bol rondom een punt: hoe meer je lens van de bol vult, hoe beter. Dus je wilt graag een kleine bol (de lens zit dichtbij) of een grote lens die meer van de bol vult. Aangezien de NA en k_1 limieten hebben, moet je op den duur naar een kortere golflengte, naar een 'blauwere' kleur. Op die manier kan je kleiner printen en dus een snellere chip maken.

Om deze reden werd er al meer dan 30 jaar geleden onderzoek gestart naar een nieuwe generatie machines die met kortere golflengtes zou gaan werken.[11–14] Dit werd uiteindelijk de moderne extreme ultraviolet (EUV) nanolithografie machine. Maar hoe zijn we uitgekomen bij een machine die tin druppels opblaast?

Het eerste deel van de puzzel is te vinden bij de spiegels die in de machine zitten. Deze spiegels worden gebruikt om het licht te verzamelen, te verplaatsen, en om uiteindelijk de chip mee te belichten. Je kunt geen lenzen gebruiken, want deze extreem korte golflengtes worden geabsorbeerd door bijna alle materialen*. De oplossing is om speciale (gebogen) meerlaagse spiegels te gebruiken.

*Ook lucht absorbeert EUV licht, er is dus een vacuüm in de machines.

Deze meerlaagse spiegels bestaan uit tientallen lagen van twee afwisselende materialen. Het kernprincipe is dat een kleine deel van het licht gereflecteerd wordt op elke even laag (de reflector) terwijl al het licht doorgelaten wordt door de oneven lagen (de spacer). Als je dan de afstand tussen de opvolgende reflecterende lagen exact afstemt aan de golflengte van het licht, krijg je constructieve interferentie* en dus reflectie van het licht. Dit is het 'Bragg effect' en is geïllustreerd in Figuur 2. Aangezien de reflecterende lagen afgestemd moeten worden op de golflengte van het licht, werkt dit alleen voor een heel nauw bereik aan golflengtes. Stel je voor dat je een spiegel gemaakt hebt voor 532 nm licht (groen), en er valt 580 nm licht op (geel). In deze situatie zal de constructieve interferentie niet voorkomen en krijg je dus niet de reflectie die je wilt. Als je dit toepast op de extreem korte golflengtes van EUV lithografie (tientallen nanometers), loop je tegen allerlei uitdagingen aan zoals de benodigdheden van lagen die slechts 5 nm dik zijn,[15] wat natuurlijk uitermate lastig te produceren is. Er moet dus een keuze gemaakt worden voor één enkele golflengte om mee te werken.
De beste keuze is dan een spiegel gemaakt van molybdeen en silicium. Deze spiegels kunnen een reflectie halen van ongeveer 70 % van al het licht binnen 1 % van 13.5 nm (dus 13.3–13.7 nm).[16] Het record staat zelfs op 71.2 % voor spiegels gemaakt door de Universiteit van Twente![17] Aangezien je ongeveer tien spiegels nodig hebt per machine, is elke procent aan extra reflectie belangrijk. Bijvoorbeeld, een verbetering van 65 % naar 70 % reflectie per spiegel zorgt ervoor dat je twee keer zo veel licht overhoudt na tien spiegels! Dat is waarom EUV lithografie dus met 13.5 nm werkt: het is de golflengte waar de beste spiegels voor bestaan bij deze extreme golflengtes.

Nu moeten we nog zo veel mogelijk licht in de 1 % rondom 13.5 nm krijgen, hoe doen we dat? (Dit is de zogenaamde 'in-band' EUV, omdat het binnen het reflectie bereik van de spiegel valt.) Je kunt niet simpelweg weer een laser gebruiken, aangezien er geen lasers zijn die licht van deze extreem korte golflengtes produceren. Daar komt bovenop dat we ook meer dan 100 W aan in-band EUV licht willen hebben, typische waardes voor industriële nanolithografie.[15,18] Er blijft dan eigenlijk maar één manier over om dit licht te krijgen: een plasma.
Een plasma is een warm gas waarbij elektronen vrijkomen van hun atomen, waardoor je een gas krijgt van vrije elektronen en ionen (atomen met te weinig elektronen waardoor ze een positieve lading hebben). In de natuur komen plasma's voor onder hoge temperaturen (zoals de zon en elke andere ster) of bij hoge voltages (denk aan lassen of bliksem).[24] Er komt licht vrij uit een plasma, bijvoorbeeld als een elektron terugkomt bij een ion, of als een elektron springt van de ene energiestaat naar de andere. In het lab maken we simpelweg plasma's door iets op te blazen met een

*Denk aan twee golven die één grotere golf vormen.

laser*.

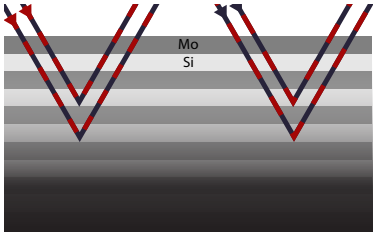

FIGUUR 2: Een schematische weergeving van het Bragg effect. Een lichtgolf komt in en reflecteert op een grens tussen de materialen. Bij het geval links is de golflengte precies afgestemd op de materiaaldikte en zijn de golfen gesynchroniseerd, geïllustreerd door de afwisselende kleur van de lijn. Rechts is de golflengte niet goed afgestemd, is de afwisselende kleur niet gesynchroniseerd, en zal de reflectie laag zijn.

Je kunt niet zomaar elke laser gebruiken om een plasma te maken, je hebt immers een bepaalde intensiteit nodig. De meest bekende lasers uit het dagelijks leven zijn continue lasers zoals laser pointers, afstandsbedieningen, of sierverlichting bij grote feesten. Deze kunnen gevaarlijk zijn als je ze bijvoorbeeld recht in je oog schijnt, maar zullen niet snel een plasma maken. De lasers in ons lab maken daarentegen extreem intense korte pulsen (van maximaal ∼100 ns, 100 miljardste van een seconde) om vervolgens een tijd weer uit te staan. Ter illustratie, de intensiteiten van de gepulste laser in dit proefschrift zijn tussen 10^7 W/cm^2 en 10^{11} W/cm^2. Dat is tussen 10 miljoen W/cm^2 en 100 miljard W/cm^2. Dit kunnen we vergelijken met een intense hittebron in het huis: het sterkste pitje op een kookplaat, waar ongeveer 2000 W aan warmte geproduceerd wordt in een typische diameter van 20 cm. Dat betekent dus een oppervlakte van 314 cm^2 en een vermogensdichtheid van $2000/314 = 6$ W/cm^2 †. De laser pulsen in dit proefschrift zijn minimaal een miljoen keer intenser dan objecten die je in huis zou kunnen vinden.
Bovendien zijn gepulste lasers industrieel beschikbaar met vermogens van meer dan 20 kW[25] en hoef je dan dus maar 0.5 % van dat vermogen om te zetten naar in-band EUV licht en dan heb je 100 W in-band EUV. Dat klinkt haalbaar, maar dat roept wel de vraag op: welk materiaal moet je gebruiken voor je plasma om zo veel mogelijk EUV te krijgen?

Tin is de perfecte keuze. Door een schitterend toeval in de natuurkunde zendt tin heel graag 13.5 nm licht uit. De eerste stap is om 10–14 elektronen vrij te maken van een tin atoom, om dus Sn^{10+} tot Sn^{14+} te maken. Als je dat voor elkaar krijgt, dan zal een groot deel van het licht dat vrijkomt van het tin plasma rond 13.5 nm zitten.[27,28] Zo kan je het voor elkaar krijgen dat bijna 20 % van al het licht dat uit een tin plasma komt binnen de 1 % rondom 13.5 nm, de 'in-band' EUV, te krijgen.[29] Op die manier is het dus ook gelukt om conversie efficiëntie (CE) van laser licht naar EUV licht te

*In het Engels een 'laser-produced plasma,' oftewel LPP.

†De laser pointer van eerder met een vermogen van ∼100 mW komt ook niet in de buurt aangezien de lichtbron vaak ∼5 mm in diameter is en dus nog niet eens boven een W/cm^2 uitkomt.

krijgen van bijna 5 %,[30] waardoor >100 W EUV lichtbronnen niet alleen meer een droom zijn.

Een moderne EUV lichtbron

En zo geschiedde het. Met meer dan 20 jaar aan continue ontwikkeling achter de rug heeft ASML inmiddels een commerciële EUV lichtbron die meer dan 500 W kan produceren.[32,33] En *alleen* ASML kan die lichtbron maken*, en dus ook alleen zij kunnen een EUV lithografie machine maken.

*Via hun afdeling in San Diego, VS. Vandaar het extra geopolitieke spel tussen de VS en Nederland hierover.

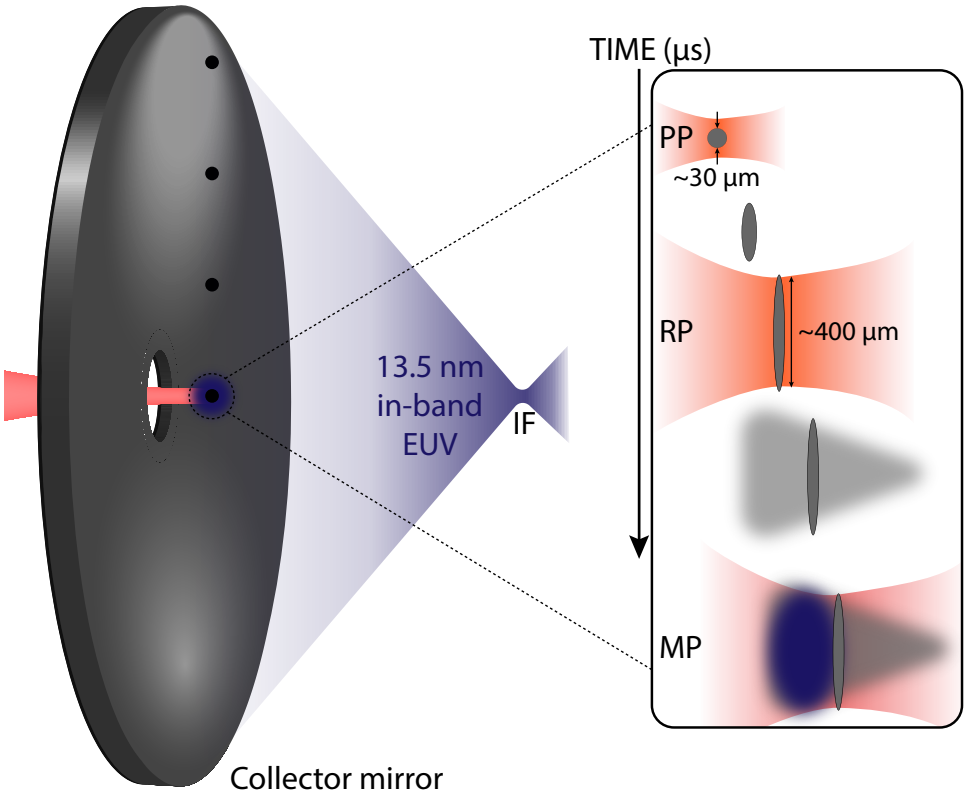

FIGUUR 3: Een schematische weergave van een moderne EUV lichtbron met zijn meerdere laser pulsen. De tin druppels worden vervormd door de pre-puls (PP), om vervolgens verdampt te worden (RP). De laatste stap is om de druppels op te blazen met de hoofdpuls (MP) om het EUV licht te produceren. Links is de spiegel die het EUV licht verzameld en via de 'intermediate focus' (IF) naar de rest van de machine stuurt.

Maar hoe werkt een moderne EUV lichtbron dan? Figuur 3 laat een schematisch overzicht zien van de belangrijke onderdelen van een moderne EUV lichtbron. Als eerste: de 'verzamel' spiegel. Deze heeft als taak om zo veel mogelijk van het EUV licht dat uit het plasma komt de rest van de machine in te sturen via de 'tussen focus' ('intermediate focus' (IF) in het Engels) zodat het daar gebruikt kan worden. Als tweede zit er waterstofgas rondom het plasma. Dit gas moet ervoor zorgen dat er geen tin om de spiegel komt en zo de spiegel onbruikbaar maakt. Aangezien het tin met kilometers per seconde wegvliegt*, is dit gas onmisbaar. De druppelgenerator zorgt ervoor dat er daadwerkelijk tin is om het EUV licht mee te maken. Deze druppelgenerator schiet 50.000 tin druppels per seconde af; elke druppel zal in de machine opgeblazen worden om een flits van EUV licht mee te maken.

Bovendien komt één tin druppel niet één maar drie lasers tegen in een moderne EUV lichtbron. Alle drie zijn ze geoptimaliseerd om zoveel mogelijk licht uit een druppel te krijgen. De eerste laser, de 'pre-puls' (PP), vervormt het tin van een druppel naar een 'pannenkoek' vorm.[36,37] In deze stap rekt de druppel meer dan 10x uit, van een diameter van tientallen micrometer naar bijna een halve millimeter met een dikte tussen 0.05–2 µm. Deze pannenkoek is dus >200x breder dan dik; een hele dunne pannenkoek. Het voordeel hiervan is dat het gemakkelijker is om efficiënt EUV licht te maken van een dunne en brede pannenkoek dan een heel dikke druppel.[35] Een nadeel is dat er wat tin verloren gaat via kleine fragmenten[39] in dit hele proces van de druppel omzetten naar een pannenkoek; deze tin doet niet meer mee later in het proces. De tweede laser is de verdampingspuls (in het Engels: 'rarefication pulse', vandaar RP). Deze puls komt een paar microseconden later[33] en verdampt de pannenkoek om er zo een grote tin damp van te maken. Het voordeel van deze puls is dat een damp efficiëntere absorptie geeft voor de laatste laser puls.[35,40] De laatste puls, de hoofdpuls (Engels: 'main pulse,' MP), is de puls die het plasma maakt dat EUV uitzendt. In moderne systemen is dit een CO_2 gas laser met een golflengte diep in het infrarood (10.6 µm). Deze CO_2 laser produceert 50.000 pulsen per seconde[26,41] met een totaal vermogen van >20 kW,[33,35] ideaal om een hoog vermogen EUV te krijgen.

De rol van ARCNL in onderzoek naar EUV lichtbronnen

Natuurlijk staat de ontwikkeling van de EUV lichtbron niet stil, ook al bestaan er nu bronnen met een vermogen van 500 W. Deze ontwikkeling gebeurt niet alleen bij ASML, waar al meer dan 40.000 mensen werken, maar ook bij verschillende andere locaties, zoals ARCNL†. Dus wat is het verschil tussen ARCNL en ASML?

*Het is gewoon een explosie waar een beetje nuttig licht bij vrijkomt.

†Naar mijn mening uitgesproken als *arc-NL*.

S

Het bedrijf ASML zit in Veldhoven en ontwikkelt, bouwt en verkoopt de nanolithografie machines die gebruikt worden voor de productie van computerchips. Het werk bij ASML is gerelateerd aan deze machines, zowel de huidige modellen, om deze te onderhouden of verbeteren, of de volgende modellen. Er is echter maar een klein deel van het bedrijf dat onderzoek doet naar nieuwe ontwikkelingen die in de verdere toekomst gebruikt kunnen worden in de machines, zonder directe toepassing op een van deze modellen.
Dat is geheel anders bij ARCNL, waar academisch onderzoek gedaan wordt. ARCNL een samenwerking tussen ASML, NWO (onderzoek vanuit de Nederlandse staat), de Vrije Universiteit Amsterdam (VU), de Universiteit van Amsterdam (UvA), en de Rijksuniversiteit Groningen. Een zogenaamde 'public-private partnership' (samenwerking tussen privé en publiek).
Daarom is al het onderzoek bij ARCNL in de richting van ASML-gerelateerde onderwerpen, zoals de lichtbron, maar ook andere onderwerpen zoals materiaalkunde. Het doel is dus om kennis op te doen over de complexe natuurkunde of scheikunde die achter de machines van ASML schuilt, maar je werkt bij ARCNL niet direct aan de verschillende modellen van de machine. De onderzoekers bij ARCNL werken vaak ook aan hun proefschrift, zoals deze, en dit is waar de universiteiten komen kijken: alleen bij een universiteit kun je promoveren. In het werk dat je doet onderzoek je dus natuurkunde of scheikunde gerelateerd aan een deel van de ASML-machine, onderzoek dat je uiteindelijk samenvat in een proefschrift. En op die manier kom je terecht in een complexe situatie als de mijne, waar ik promoveer aan de Vrije Universiteit Amsterdam (dat is niet voor iedereen bij ARCNL zo), ook al heb ik al het onderzoek uitgevoerd op locatie bij ARCNL, onderzoek dat gerelateerd is aan ASML. Ik snap dat het soms verwarrend is.

Onderzoeksvragen en overzicht van dit proefschrift

Zoals hierboven al naar gehint werd, zijn er nog veel open vragen gerelateerd aan de EUV lichtbron. Sommige van deze open vragen zijn redelijk fundamentele natuurkunde, andere vrij direct toepasbaar op de huidige machines, maar het idee is dat ze allen, uiteindelijk, leiden naar meer EUV licht uit de bron.
Zo is ruimte voor optimalisatie rondom de verdampingspuls gigantisch. Je kunt je bijvoorbeeld afvragen: "Wat voor compositie heeft mijn ideale damp?" Aanpassingen aan de verdampingspuls zouden vrij gemakkelijk toegepast kunnen worden in een moderne EUV lichtbron, aangezien deze al zo'n puls heeft. Maar niks houdt ons tegen om te denken over grotere veranderingen. Waarom zou je deze huidige drie pulsen moeten gebruiken? Waarom niet meer pulsen, of een van de pulsen vervangen? Een van de opties in dit gebied is om de hoofdpuls die momenteel opgewekt wordt met behulp van CO_2 gas te vervangen met een vastestoflaser, waar speciale

kristallen gebruikt worden, die 2 µm infrarood licht uitzenden. Vastestoflasers worden al gebruikt voor de pre-puls en de verdampingspuls omdat ze hoge efficiëntie van elektriciteit naar laser vermogen bieden in een compacte vorm. Echter, door een aantal technologische limieten zijn vastestoflasers tot nu toe nog nooit een bedreiging geweest voor de CO_2 gas laser als hoofdpuls. Dit is nu aan het veranderen met recente ontwikkelingen rondom EUV lichtbronnen met 2 µm vastestoflasers als hoofdpuls, die de hoge efficiëntie van vastestoflasers combineren met goede efficiëntie om EUV licht op te wekken.

Dit maakt het voor dit proefschrift dus uitermate interessant om de interactie van vastestoflasers en tin te onderzoeken. We onderzoeken nieuwe toepassingen van vastestoflasers, gerelateerd door EUV lichtbronnen en geïnspireerd door de verdampingspuls en de hoofdpuls. De vraag is simpelweg: "Wat gebeurt er al een lichtpuls, geproduceerd door een vastestoflaser, interacteert met tin?"

Deze vraag kunnen we nog opsplitsen gebaseerd op de intensiteit van de lichtpuls. Het eerste intensiteitsbereik is het lage bereik, waar de lichtpuls van de vastestoflaser verdamping zal veroorzaken. Hier gebruiken we een vastestoflaser die licht genereert met een golflengte van 1 µm, net als de verdampingspuls.[33] In dit bereik hebben we een drietal vragen die we willen beantwoorden: "Wat is de compositie van een tin damp gemaakt door de verdamping van een tin pannenkoek door een vastestoflaser?", "Welk proces beschrijft deze verdamping?" en "Welke laserparameters hebben invloed op de resulterende damp?" Bij compositie verwijzen we naar het feit dat damp ook kleine deeltjes of kleine druppels in zich kan hebben, zoals ook het geval is in waterdamp na het douchen. Dit kan bij tin ook het geval zijn, en wil je dat dan? Dus, als we specifieker zijn: "Wil je kleine druppels of deeltjes in je damp of niet?"
In het hogere intensiteitsbereik gaat het om plasma's die EUV licht uitzenden. In dit gebied gebruiken we nog steeds vastestoflasers, maar dan met een golflengte van 2 µm, aangezien dit de veelbelovende golflengte is voor toekomstige EUV lichtbronnen.[30] Hier stellen we ons de vragen: "Wat is het gedrag van de ionen die weg vliegen uit een plasma gegenereerd door een 2 µm vastestoflaser?", "Hoe kunnen we EUV lichtbronnen gebaseerd op 2 µm vastestoflasers opschalen tot industriële niveaus?" en "Wat is het beste doelwit, zoals de tin pannenkoek of damp, voor een EUV lichtbron met een 2 µm vastestoflaser?"

Deze onderzoeksvragen hebben geleid tot vier hoofdstukken, waar elk hoofdstuk een of meerdere van deze vragen probeert te beantwoorden. Hoofdstukken 1–3 zijn gerelateerd aan de verdamping van tin, terwijl Hoofdstuk 4 ons werk gerelateerd aan EUV lichtbronnen met 2 µm vastestoflasers laat zien. Hieronder volgt een korte beschrijving van elk van deze hoofdstukken. Deze samenvatting zal afsluiten met een terugblik ("Hebben we de vragen beantwoord?") en een vooruitblik ("Wat nu?").

Hoofdstuk 1 gaat over de damp die vrijkomt bij het verdampen van een dunne pannenkoek van tin. De vraag is simpel: "Wat zijn de eigenschappen van deze damp precies?" Om die vraag te kunnen beantwoorden presenteren we in dit werk een nieuwe diagnostiek om de damp te onderzoeken. De kern van de diagnostiek is dat we foto's maken van de tin damp met een veel verschillende kleuren, ongeveer 600, allemaal in het UV (tussen 235 en 400 nm)*. Voor elke kleur maken we een foto van de schaduw van de damp; het licht gaat dus door de damp, en we zien hoeveel van het licht opgenomen wordt door de damp. Door dit te onderzoeken voor verschillende kleuren, *spectroscopisch*, kan je veel zeggen over de damp, zoals de dichtheid en temperatuur van de damp, maar ook of er hele kleine nanodruppels van tin aanwezig zijn (denk aan kleine druppels water na het douchen, maar dan veel kleiner). Het speciale aan onze diagnostiek is dat we foto's maken met verschillende kleuren, dus we kunnen *per locatie* in de damp bepalen wat de dichtheid en temperatuur is, met een resolutie van 10 µm (een honderdste van een mm). Met behulp van de nieuwe diagnostiek laten we zien dat in deze specifieke tin damp inderdaad nanodruppels aanwezig zijn, zwevend in een gas van vrije atomen. Bovendien laten we zien dat elke locatie in de damp hetzelfde is: elke locatie heeft nanodruppels en dezelfde temperatuur (rondom de kooktemperatuur van tin), alleen de hoeveelheid damp verschilt per plek.

Hoofdstuk 2 duikt in de verdamping zelf, *hoe* werkt dat nu als je iets verdampt in een paar nanoseconden (miljardste van een seconde)? Om dat te doen gebruiken we een lange verdampingspuls van 100 ns†, waardoor we foto's kunnen maken tijdens de verdamping. Deze foto's maken we deze keer met groen licht, omdat we juist niet de damp willen zien, maar naar de pannenkoek zelf willen kijken. Je kunt er namelijk een beetje doorheen kijken, omdat hij zo dun is. Door dan op verschillende momenten tijdens de verdamping te kijken, zien we dat de pannenkoek geleidelijk dunner wordt tijdens de verdampingspuls. Dit wijst naar Hertz-Knudsen verdamping. Om dat te bewijzen, ontwikkelen we een computermodel gebaseerd op de formules die Hertz-Knudsen verdamping beschrijven. Dit model reproduceert onze experimentele data heel goed. Op die manier hebben we bewezen hoe de tin pannenkoek verdampt; het is simpelweg dezelfde manier waarop een plas water buiten verdampt na een regenbui, maar dan een miljard keer sneller.

In **Hoofdstuk 3** zetten we de verdampingspuls op steroïden door zijn intensiteit tot ∼100x te verhogen. We doen dit omdat we willen weten hoe je de damp kan veranderen. Leuk dat een damp kan maken met nanodruppels, maar wat als ik

*Al deze foto's worden na elkaar gemaakt, met 50 foto's per kleur, wat kan omdat het proces om de tin damp te maken heel herhaalbaar is. Dit noem je *stroboscopisch*, denk aan een flitsende lamp in de nachtclub. Typisch duurt het maken van al deze foto's dus een paar uur.

†Alles is relatief.

dat niet wil? Welke parameter rondom de verdamping moet ik dan veranderen? Daarom onderzoeken we hoe de damp die vrijkomt afhangt van de intensiteit van de verdampingspuls. Je kunt dit vergelijken met water koken: Als je het fornuis harder zet en het water sneller kookt, verandert de waterdamp dan? We gebruiken een groot bereik aan intensiteiten van de verdampingspuls en we gaan ook zo ook zo hoog dat we ook plasma maken *tijdens* de verdamping. Wat we vinden is dat als je plasma maakt tijdens de verdamping, dat de damp flink verandert. Niet alleen krijg het een andere vorm (omdat het plasma een druk uitoefent op de damp), maar ook wordt de damp veel warmer. (Eerder was het ∼2500 °C, rond de verdampingstemperatuur van tin, nu schiet het omhoog naar ∼8000 °C.) Ook verdwijnen de nanodruppels en blijft alleen het gas van vrije atomen over. Zo hebben we laten zien dat de intensiteit van de verdampingspuls kritisch is voor de damp die vrijkomt.

Ten slot, maken we eindelijk EUV licht en bespreken we de andere toepassing van vastestoflasers in **Hoofdstuk 4**. Specifiek kijken we naar hoe je EUV licht kan maken met een 2 µm-golflengte vastestoflaser, in plaats van de industriële standaard 10.6 µm CO_2-gas laser. Waarom zou je dat doen? Omdat een CO_2-gas laser extreem veel stroom gebruikt voor het vermogen aan licht dat hij uitzendt, terwijl een vastestoflasers veel efficiënter is. Dus als je een vergelijkbare, of zelfs iets mindere, laserlicht naar EUV licht efficiëntie kan krijgen met een 2 µm vastestoflaser, dan zal je totale elektriciteit naar EUV licht efficiëntie beter zijn. Er is daarom dus ook al veel onderzoek gedaan naar EUV productie met 2 µm lasers, ook buiten het werk in dit proefschrift. Maar het complete plaatje miste: er waren onderzoeken gedaan naar welke kleuren licht vrijkomen van het plasma, de ionen, hoeveel EUV licht, etc., maar geen studie die dit allemaal bijeenbrengt in één geheel. Wij brengen al deze dingen in een geheel en laten zien dat we een volledige reconstructie van de energie in het plasma kunnen doen. Dus we balanceren de inkomende energie, de laser, met de uitgaande energie, het licht, de ionen, het restant van de tin pannenkoek, en reflectie of transmissie van de laser. Het merendeel, ∼65 % van de energie komt vrij als licht, maar dat is licht met allerlei golflengtes, niet alleen de gewenste 13.5 nm (dat is maar ∼4 %). We bestuderen ook het gedrag van ionen, het 'afval' van het plasma, en laten zien hoe je de hoeveelheid ionen kunt minimaliseren. Dit unieke inzicht in deze energiebalans is het resultaat van jaren aan ontwikkeling van de opstelling binnen onze groep en kan gebruikt worden door anderen als een maatstaaf. Ook benadrukken we nogmaals de unieke mogelijkheden die EUV productie met 2 µm vastestoflasers biedt.

Dus waar brengt dat ons nu? Als we terugkijken naar de vragen die we gesteld hebben rondom verdamping, zijn ze allemaal beantwoord. Met behulp van onze nieuwe diagnostiek (Hoofdstuk 1) weten we de compositie van een tin damp. Ook hebben we in Hoofdstuk 2 bewezen dat Hertz-Knudsen onze verdamping beschrijft.

En als laatste hebben we ook laten zien welke laserparameter de belangrijkste is voor de resulterende damp: de intensiteit van de verdampingspuls.
Rondom EUV-productie met behulp van 2 µm vastestoflasers hebben we ook grote stappen gezet. Zo hebben we in Hoofdstuk 4 het gedrag van ionen in detail bestudeerd, en ook laten zien hoe je ze kunt minimaliseren. In Hoofdstuk 4 hebben we ook laten zien hoe je de lichtproductie op kan schalen naar industriële niveaus. Echter hebben we nog niet laten zien wat het beste doelwit is voor een EUV-lichtbron met een 2 µm vastestoflaser.

Toch kunnen we stellen dat we veel geleerd hebben over de interactie van tin met lichtpulsen geproduceerd door vastestoflasers. Wat komt hierna dan? In twee korte vooruitblikkende stukken doe ik al het tipje van de sluier omhoog. Zo laten we zien dat de nieuwe diagnostiek met UV kleuren, zoals geïntroduceerd in Hoofdstuk 1, maar dan nu met behulp van een andere laser, ook gebruikt kan worden om atoomfysica te onderzoeken. Het tweede vooruitblikkende stuk zet een eerste stap naar het beantwoorden van de laatste open vraag rondom 2 µm: waar moet je op schieten? Blijven we op tin pannenkoeken schieten of gaan we weer terug naar direct op de tin druppel schieten? Deze vragen zijn echter maar een paar van de vragen waar nu nog aan gewerkt wordt bij ARCNL. Genoeg voor mijn collega's om nog allerlei proefschriften over te vullen...

List of Publications

CHAPTER 1
D. J. Engels, R. A. Meijer, H. K. Schubert, W. J. van der Zande, W. Ubachs, and O. O. Versolato, *High-resolution spectroscopic imaging of atoms and nanoparticles in thin film vaporization*, Applied Physics Letters **123**(25), 254102 (2023).

CHAPTER 2
H. K. Schubert⋆, D. J. Engels⋆, R. A. Meijer, B. Liu, and O. O. Versolato, *Scaling relations in laser-induced vaporization of thin free-flying liquid metal sheets*, Physical Review Research **6**(2), 023182 (2024).

CHAPTER 3
D. J. Engels, H. K. Schubert, M. Karbedia, W. Ubachs, and O. O. Versolato, *Spectroscopic imaging of tin vapor near plasma threshold*, Physical Review Research **7**(2), 023307 (2025).

CHAPTER 4
D. J. Engels⋆, F. M. Kolhmeier⋆, Y. Mostafa, E. J. Salumbides, B. W. Slotema, R. Hoekstra, J. Sheil, W. Ubachs, and O. O. Versolato, *Full energy partitioning in 2-μm-wavelength laser driven EUV sources*, Submitted.

⋆ Equal contributions.

The author has also contributed to the following publications:

L. Behnke, E. J. Salumbides, G. Göritz, Y. Mostafa, D. J. Engels, W. Ubachs, and O. O. Versolato, *High-energy parametric oscillator and amplifier pulsed light source at 2-μm*, Optics Express **31**(15), 24142–24156 (2023).

Y. Mostafa, L. Behnke, D. J. Engels, Z. Bouza, J. Sheil, W. Ubachs, and O. O. Versolato, *Production of 13.5 nm light with 5% conversion efficiency from 2 μm laser-driven tin microdroplet plasma*, Applied Physics Letters **123**(23), 234101 (2023).

Y. Mostafa, L. Behnke, D. J. Engels, Z. Bouza, J. Sheil, W. Ubachs, and O. O. Versolato, *Erratum: "Production of 13.5 nm light with 5% conversion efficiency from 2 μm laser-driven tin microdroplet plasma"*, Applied Physics Letters **126**(4), 49901 (2025).

H. K. Schubert⋆, D. J. Engels⋆, M. Kharbedia, H. Gelderblom, and O. O. Versolato, *Observation of discrete concentric surface modulations on free-flying liquid tin sheets*, Physics of Fluids **37**(9), 094108 (2025).

S. J. J. de Lange, J. Gonzalez, D. J. Engels, F. M. Kohlmeier, and J. Sheil, *Ion emission properties from tin plasmas generated by* 2 µm*-wavelength laser pulses*, Submitted.

M. Kharbedia, B. Liu, R. A. Meijer, D. J. Engels, H. K. Schubert, L. Bourouiba, and O. O. Versolato, *Rim destabilization and re-formation upon severance from its expanding sheet*, Submitted.

J. Gonzalez, D. J. Engels, D. J. Hemminga, O. O. Versolato, and J. Sheil, *Formation of a strongly radiative plasma from a Sn vapour due to the presence of nanoparticles*, Submitted.

Y. Mostafa, L. Behnke, D. J. Engels, and O. O. Versolato, *Mass use in* 2 µm *laser driven tin plasma using sheet targets*, Submitted.

M. Kharbedia, H. Franca, H. K. Schubert, D. J. Engels, M. Jalaal, and O. O. Versolato, *Laser-driven droplet deformation at low Weber numbers*, Submitted.

H. K. Schubert, R. A. Meijer, B. Liu, D. J. Engels, and O. O. Versolato, *Time resolved study of the plasma threshold of free-flying liquid tin sheets*, In preparation.

⋆ Equal contributions.

Acknowledgments

Now, for probably the most read section of any thesis, where everyone plays the traditional game of 'spot my name': the Acknowledgments! This thesis ends a chapter of my life that started at the end of the COVID-19 pandemic. It seems like a blur now, but without the whole pandemic, this thesis would most likely have never happened. It is the reason I wanted to escape my student room in Eindhoven; a problem solved by diving into the lab at ARCNL in Amsterdam. The warm welcome and cool work there motivated me so much that I decided: Why not stay a while longer? It was an excellent decision to do so. Now, nearly four years after arriving at the Amsterdam Science Park for the first time in August 2021, my journey as a PhD candidate at ARCNL has come to an end. I am very grateful to all the people who made my PhD a success or just brightened my days at (or outside) ARCNL. Let us hope that I do not forget to list anyone...

First, I want to start by acknowledging the people who will definitely not read these words. Specifically, the people in my life that have not made it to this moment: my grandpas, Elise, and Sander. I am happy to have had the opportunity to walk alongside you for the time I did. You will never stop inspiring me to live my life to the fullest (or to, for example, cycle up a mountain) and not to take it for granted. Thanks, all of you, for our time together.

Oscar, thanks for all the support and guidance. Ever since I met you, I have always looked up to how you run the group. Honestly, I don't know how you do that and combine it with your busy family life. You have been a mentor to me, teaching me many things related to physics but also about life in general, and I am very proud of what we achieved during our time working together. I feel blessed to have had a supervisor that I could trust this much and who was so understanding, also in the bad times. I will always fondly remember our time together, especially the good times, such as when I got to show your family around during the ARCNL Open Day; I had such a blast. I wish you the best of luck with the group, your wife and daughters, and all your other loved ones.

I am also grateful for my co-promoters, John and Wim Ubachs. John, thanks for all our endless discussions. I happily spent way too much time in the 'John-trap,' having discussions about everything and nothing. I am happy that you finally found your

own place in Amersfoort, best of luck there and with your group.
Wim, thank you for all the atomic physics and laser physics crash courses. I learned a lot from you and I am grateful for all your input (especially on bibtex files, I have never before met a person who goes through bibtex files like you, it is really a talent). I still appreciate talking with you every time you visit ARCNL, even in retirement.

A bit further away, I want to thank my original supervisor, Randy. Randy, it has been a while since you left to go to sunny San Diego, but this thesis would not have happened without you supervising me when I was 'just' a Master student at ARCNL. I really enjoyed working with you. It motivated me so much and I learned a lot in a short time. Thanks so much for giving me a running start at ARCNL and I wish you all the best on the other side of the pond.
Ronnie, Groningen is also far away, as you know. Thanks for helping me out with atomic physics, opening my mind to the world of ion measurements, and brightening my day with your dry humor. Good luck with your Untapped (and the group, of course).

I want to thank all the special people at ARCNL who make the institute such an amazing place to work. Honestly, the people at ARCNL make looking for a next job very difficult. Where will I ever find so many nice people?
I want to start with my paranymphs: Ester & Felix. Ester, we joined ARCNL at the same time, both as Master students. And then we both decided to stick around for a PhD. What are the odds that I would share this journey with such an amazing person? Your support, at work and outside of work, has been invaluable. Thank you for supporting me through the whole process.
Felix, as Surabhi always says, we might be too much alike. But that might also explain why we had so much fun together. Even during long and painful beamtimes, I would always enjoy working with you (and we would also get a lot of stuff done, win-win). Then, after spending the entire week in the lab together, we would just go cycling together on the weekend. What more can you want? (Maybe some music during the beamtime?) Thanks for everything and let us agree to keep the cycling going, even when we are no longer doing beamtimes together!

Talking about cycling, I would like to thank all the ARCNL-related people who are part of my usual cycling club: Felix, Kevin, Lucas, and Reynolds. Thanks for all the fun rides, from laughing about Kevin's backpack, to eating ice cream together on summer days or poking fun at each other for whatever reason. I always enjoyed our trips together (and making you guys suffer). Onward to many more trips!

Back at ARCNL, I would like to thank all the members of the ARCNL PV who play a key role in making the institute such a fun place to be at. I am not going to list names (you know who you are, and I fear forgetting someone), but I really appreciate

all your hard work. No experience comes close to slightly annoying your colleagues by bending the rules in a PV activity. Again, without you, ARCNL would not be as fun. Thanks!
To all my colleagues from the Source department: Thank you for all the support, both in the lab and outside, and also for all the fun we had together. I will remember all our politics-inspired (or just random) discussions fondly. From East-German politics (personified by Karl, of course), etymology (especially Lucas and Stan, to the annoyance of some), Mats' obsession for quinoa, Surabhi's many calls with her parents (still not married yet...), to something completely random (Bas' specialty). I always enjoyed our non-work related time together.
Some kind words for the black swans of the Source department: the team in Groningen. I always enjoyed any moment shared with you. From buffer gas beamtimes, the defense ceremonies (of Klaas or Subam, for example), to extracurricular activities with Luc and Xyoisan or discussions about Emiel's ducks, or helping Fleur to build her new droplet generator in Groningen. It was a pleasure and I wish you all the best! May you finally stop the ions!

Laurens is a member of the EUVPP team that deserves some special attention because I have the feeling that the role of a technician is often underappreciated. But without you, much of the work in this thesis would not have been possible. Thanks for all your hard work!
I also would like to thank all the support staff located at AMOLF, from precision engineering and mechanical design to purchasing or software and electronics engineering. Your amazing work made many of the experiments seen in this thesis possible. Thanks for that! I want to highlight some people with whom I worked the most closely.
Henk-Jan, thank you for all your amazing work. You have surprised me with amazing work countless times, you always managed to pull some amazing design out of thin air. Good luck with all your future projects, from AMOLF to Flevoland.
Bob, thank you for all your support with the electronics around our setup. I always wanted more and even in your role as the reluctant boss, you were always there to help me achieve that vision. Thanks for all that effort!
Jorijn, the 'senior' software engineer (read: god) of SonicScrewdriver. Although it is easy to laugh at bugs, I want to thank you for making SonicScrewdriver an amazing tool that makes our data acquisition so much easier. A lot has happened throughout the last four years, but at every stage I enjoyed working with you, whether it was updating wiki lists with requests or hours long debug sessions in the lab. Good luck in your new house and I hope you get a lamp soon!

Speaking about keeping something running: I want to thank the people who keep ARCNL running. From Marjan and Wim van der Zande, to the entire secretariat

(and a little bit my fellow members of the Works Council). Thanks for your tireless efforts!

Now that my time as a student of physics has come to an end, I would like to thank my amazing friends who accompanied me on this journey that started with an introduction week in 2015 at TU Eindhoven. (Ten years ago... We are getting old.) I was afraid to leave such a good group of friends behind when I moved to Amsterdam, but I am very happy to still have you all in my life. Dennis, Mitchel, Niels, Rick, Rik, Stef, Tom O, Tom A, thanks for all the amazing moments together and onward towards many more adventures!
I also want to thank all my friends from URE. My experience building a barely working racecar with you guys shaped me in many ways, but it also left me with some amazing friends who still brighten my days regularly. Dennis, Josh, Max, Raymond, Stan, and Teun, thank you for all for being great friends and always showing interest in this weird physics thing I was doing.
Aris, thanks for all the fun weekends in Leuven. I always look forward to our regular visits and cycling trips. You don't really need any more luck with the PhD since you are acing it, so I will just wish you luck with the Belgian hills: May you reach the top of one before me soon again. Also, thank you Pascal for pushing me to take this opportunity. Your support during our many post-board year cycling trips helped me a lot in deciding what I wanted to do with my life, for which I will always be grateful.
To Wies & Gergő, thanks for all the incredible (and very *burgelijke*) dinners together. I guess we have to change the name of our chat group now?
Ries, I am thankful that I could go through this PhD journey with you. Playing Factorio together while ranting about stupid experiments, what more do you want? I am looking forward to seeing your thesis soon as well (no pressure). I promise, I will still listen to your rants about broken down experiments even now I don't have my own anymore.
Finally, Marion, I always look forward to our video calls or the visits to Munich. I love that I have you in my life, even now that you have left the Netherlands, and I look forward to many more amazing hours-long discussions via the phone. Good luck with Lukas and baby Roxas!

Ik hoop dat mijn oma's zo ver zijn gekomen (in het proefschrift bedoel ik dan). Ik kom graag *langs* in Panningen en Meijel; het is een van mijn favoriete dingen aan de bezoeken aan Limburg. Ik ben blij dat ik nog zo lang heb kunnen genieten van jullie wijsheden. Tot bij de verdediging en gedraag jullie hè!
Pap en mam, zonder jullie was ik nooit hier gekomen. Al bijna 28 jaar zijn jullie er altijd voor mij. Na al die jaren studeren heb ik een ding geleerd: ik moet wat vaker voorstellen om te videobellen...
Daphne, toch leuk dat we nu (ongeveer) tegelijk afstuderen. Ik ben blij dat je inmiddels

een fijn appartementje gevonden hebt. En nu zelfs katten! Zie je wel, we komen er wel.
Ik wil Enzo en Dino ('de jongens') bedanken voor alle relaxerende aaisessies. (And everyone who took care of them at some point, such as Barsha, Robin, and Ester.) Een aaibaar object is heel erg aan te raden voor als je een PhD gaat doen.
En natuurlijk Tanya. We zijn al zo lang samen dat ik soms vergeet hoeveel geluk ik heb met jou. Ons huisje (of ja eigenlijk die van de jongens, wij zijn er minder) is mijn veilige plek, zeker als jij er bent. Ik ga onze gezamenlijke fietsritjes naar ARCNL wel missen. Het is een beetje eng om weg te gaan uit zo'n vertrouwende plek. Maar ook dat komt wel goed, het is niet de eerste keer in de laatste zeven jaar, en samen kunnen we het aan.

Dion
June 2025